ABSTRACT

MICROENGINEERED SENSOR DEVICES WITH FIELD EMISSION ELECTRON SOURCES

by
Chao Sun

This dissertation describes the design, simulation, fabrication, and characterization of a microengineered pressure sensor device and a microengineered mass spectrometer device, both of which use field emission cathode tip arrays as electron sources. VLSI and MEMS process techniques are used to scale down the dimensions from existing vacuum pressure sensors and mass spectrometers.

The microengineered pressure sensor device is fabricated on a silicon substrate approximately 1cm by 1cm. It consists of an electron source in the form of cathode tip array structure, an electron accelerating space which includes a gas ionization volume, and an ion collection electrode. The electrons emitted from the cathode are accelerated to energies high enough to ionize neutral gas molecules in the ionization volume. The ions are then collected by a negatively biased electrode located at center of the device. This pressure sensor device further utilizes a magnetic field created by a permanent magnet to lengthen the electron trajectory. It is the first report of a magnetic ionizing type pressure (vacuum) sensor with a field emission electron source on a chip. The test results show that the ion current is a linear function of pressure and is consistent with the theoretical modeling and simulation.

The microengineered mass spectrometer device is fabricated using two silicon substrates approximately 1cm by 1cm, where one is a cathode electron source and the

MICROENGINEERED SENSOR DEVICES WITH FIELD EMISSION ELECTRON SOURCES

by
Chao Sun

A Dissertation
Submitted to the Faculty of
New Jersey Institute of Technology
in Partial Fulfillment of the Requirements for the Degree of
Doctor of Philosophy

Department of Electrical and Computer Engineering

January 1998

APPROVAL PAGE

MICROENGINEERED SENSOR DEVICES WITH FIELD EMISSION ELECTRON SOURCES

Chao Sun

Dr. William N. Carr, Dissertation Advisor — Date
Professor of Electrical and Computer Engineering, NJIT

Dr. Kenneth R. Farmer, Dissertation Advisor — Date
Associate Professor of Physics, NJIT

Dr. Robert B. Marcus, Committee Member — Date
Research Professor of Electrical and Computer Engineering, NJIT

Dr. Edip Niver, Committee Member — Date
Associate Professor of Electrical and Computer Engineering, NJIT

Dr. Marek Sosnowski, Committee Member — Date
Associate Professor of Electrical and Computer Engineering, NJIT

BIOGRAPHICAL SKETCH

Author: Chao Sun

Degree: Doctor of Philosophy

Date: January 1998

Undergraduate and Graduate Education:

- Doctor of Philosophy in Electrical Engineering,
  New Jersey Institute of Technology, Newark, NJ, 1998

- Master of Science in Electrical Engineering,
  New Jersey Institute of Technology, Newark, NJ, 1993

- Bachelor of Science in Physics,
  Fudan University, Shanghai, P. R. China, 1982

Major: Electrical Engineering

To my beloved family

ACKNOWLEDGMENT

I would like to express my sincere gratitude to my advisors, Profess William N. Carr and Profess Kenneth R. Farmer, for their valuable guidance, consistent support and encouragement throughout my graduate studies at NJIT.

Special thanks are given to the other members of my dissertation committee: Profess Robert B. Marcus, Profess Edip Niver, and Profess Marek Sosnowski for their careful review, productive comments, and helpful suggestions.

I wish to express my appreciation and acknowledgment to EPA Center on Airborne Organics for funding this project.

I wish to acknowledge all the helps and facilities made available to me at NJIT, which had a major role in completion of this dissertation. I wish to especially thank Dr. Dentcho Ivanov and Mr. Ken O'Brien for their helps in the Microelectronics Cleanroom, Dr. Robert B. Marcus for using his SEM machine, vacuum equipment and other facilities, and Dr. Roland Levy for using his RF laboratory.

Finally I greatly indebted to my family for their continuous support and encouragement.

TABLE OF CONTENTS

TABLE OF CONTENTS
(Continued)

Chapter **Page**

TABLE OF CONTENTS
(Continued)

LIST OF TABLES

Table **Page**

LIST OF FIGURES

LIST OF FIGURES
(Continued)

Table **Page**

LIST OF FIGURES
(Continued)

Table **Page**

LIST OF FIGURES
(Continued)

Table **Page**

CHAPTER 1

INTRODUCTION

This dissertation describes the design, simulation, fabrication, and characterization of a microengineered pressure sensor device and a microengineered mass spectrometer device, both of which use field emission cathode tip arrays as electron sources. VLSI and MEMS process techniques are used to scale down the dimensions from existing vacuum pressure sensors and mass spectrometers. The microengineered pressure sensor device is fabricated on a silicon substrate approximately 1cm by 1cm. It consists of an electron source in the form of cathode tip array structure, an electron accelerating space which includes a gas ionization volume, and an ion collection electrode. The electrons emitted from the cathode are accelerated to energies high enough to ionize neutral gas molecules in the vacuum of the ionization volume. The ions are collected by a negatively biased electrode located at center of the device. The ion current is proportional to the vacuum pressure being measured. This pressure sensor device further utilizes a magnetic field created by a permanent magnet to lengthen the electron trajectory. The microengineered mass spectrometer device is fabricated using two silicon substrates approximately 1cm by 1cm, where one is a cathode electron source and the other is the ion collector. An external electron source is not needed. A field emission cathode tip array is used as an electron source to ionize the input gas molecules. The ions are extracted by an electric field and follow a curved trajectory that is determined by the ion mass, charge state and the crossed combination of static electric and magnetic fields. The separated ions are then collected at different locations on the parallel planar electrodes.

There is a growing interest worldwide in the concept and possible applications of miniature, micro and even nanoscale devices. These microengineered pressure sensor and mass spectrometer devices are the unique outgrowth of this interest. The objectives of this research are to develop a micro sensor for innovating the existing ionization type vacuum sensor, and to develop a portable, economical mass spectrometer system for in-situ gas detection and analyses.

In chapter two, the basic principles of ionization type pressure (vacuum) sensor and mass spectrometer are described. Some important properties and design equations are developed and discussed. The basic concepts and relations of vacuum and gas pressure parameters necessary for this design are also developed in this chapter.

Chapter three includes the fundamental field emission theory and basic features of vacuum microelectronics. The Fowler-Nordheim equation is illustrated and discussed.

Chapter four describes the design of the microengineered pressure sensor and mass spectrometer devices. Several different design structures for these devices with the respective electron and ion trajectories are shown. Advantages and disadvantages of each structure are discussed. The optimized design is determined. Sensitivity and some other important parameters of the devices are modeled and developed.

Chapter five details the process methodology for fabrication and integration of the microengineered pressure sensor and mass spectrometer devices.

Chapter six describes the device characterization. Ion current vs. pressure behaviors are measured and compared with theoretical calculations. The testing results discussed.

Chapter seven gives the summary.

CHAPTER 2

PRINCIPLE OF IONIZATION SENSOR AND MASS SPECTROMETER

This chapter reviews briefly the basic principles of ionization type pressure sensors and mass spectrometers. The basic concepts and relations of vacuum and gas pressure parameters necessary for this design are developed in this chapter.

2.1 Ionizing Type Vacuum Sensor

The first part of this research dealt with the design and fabrication of a microengineered ionization type pressure sensor device. VLSI and MEMS process techniques are used to fabricate this device. The dimensions of the ionization pressure sensor are scaled down to 1cm by 1cm. The operation of this device is similar to that of traditional ion vacuum gauge. It is based on ionization of gas molecules by electron impact and the subsequent collection of these ions at a collector. This positive ion current is proportional to pressure, provided that all other parameters, including temperature, are held constant. In this pressure sensor, a magnetic field is employed to increase the electron path length and number of ionizing collisions. The structure of this pressure sensor device is a combination of hot-cathode and cold-cathode ionization gauges. It possesses all advantages of both hot and cold cathodes gauge but eliminates some drawbacks of them, such as the additional vapor pressure due to the residual gas produced by the hot filament in the hot-cathode gauge, and non-linearity of the ion current as a function of pressure in the cold-cathode gauge.

2.1.1 Hot Cathode Vacuum Gauge

The conventional hot cathode gauge resembles a triode vacuum tube having a central cathode concentrically stretched in a cylindrical loosely wound grid (the electron collector) and a metallic cylinder referred to as the anode (the ion collector) (Figure 2.1). The gauge is operated in the electrical circuit shown in Figure 2.2. The cathode, a tungsten filament typically biased at 30V dc above ground potential, emits electrons which are accelerated to the grid by the potential difference between cathode and grid, typically 150-200V. Most of the accelerated electrons pass through the grid where their direction of motion is reversed because of the oppositely directed field of the ion collector (Figure 2.3). Electrons could distribute throughout the shaded area illustrated in Figure 2.3, cycles back and forth until they strike the grid where they are collected. Some of the electrons collide along their path with residual gas molecules and, if they possess enough energy, produce an ion-electron pair. Owing to the distribution of potential in the ionizing region, electrons are decelerated so that they are inefficient for producing ionization over a large portion of their trajectory. The positively charged ions produced are repelled by both the positively biased cathode and the electron collector, and they are collected at the ion collector, usually maintained at ground. Electrons resulting from the ionization process are collected at the grid together with the electrons emitted from the cathode. If the emission current is maintained constant, the ion current is proportional to gas pressure. The linear relationship between ion current and gas pressure fails below 10^{-8} Torr and above 10^{-3} Torr. In the lower range of pressure this is due to the residual currents (x ray) to the collector. In the upper pressure range electrons of low energy are created owing to the high frequency of electron and residual gas molecule collisions. These

electrons, which cannot yield ionization, are collected at the grid and measured as part of the emission current. This reduces the value of the gauge sensitivity [1-2].

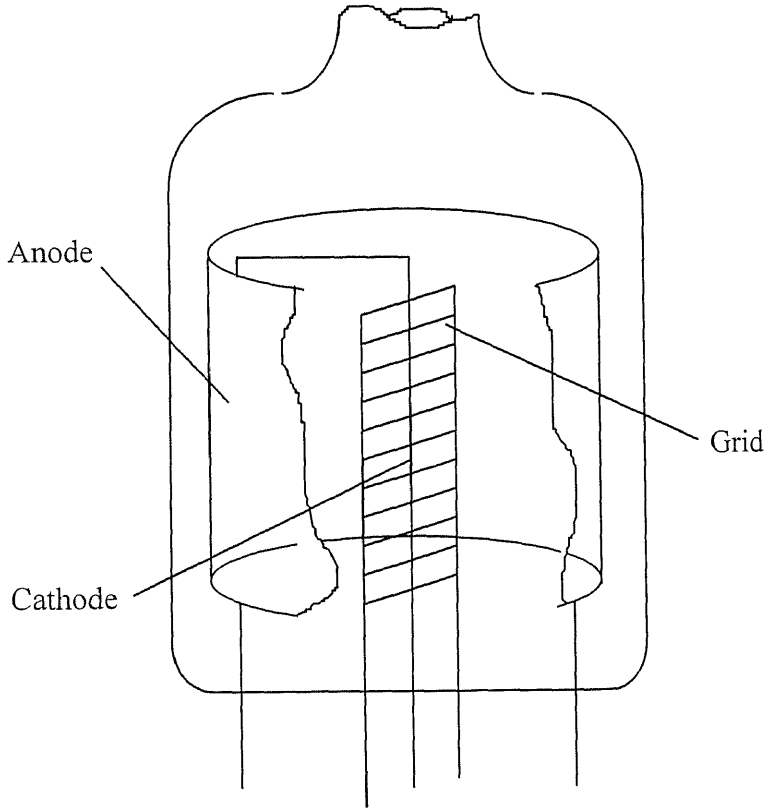

Figure 2.1 Conventional triode vacuum gauge.

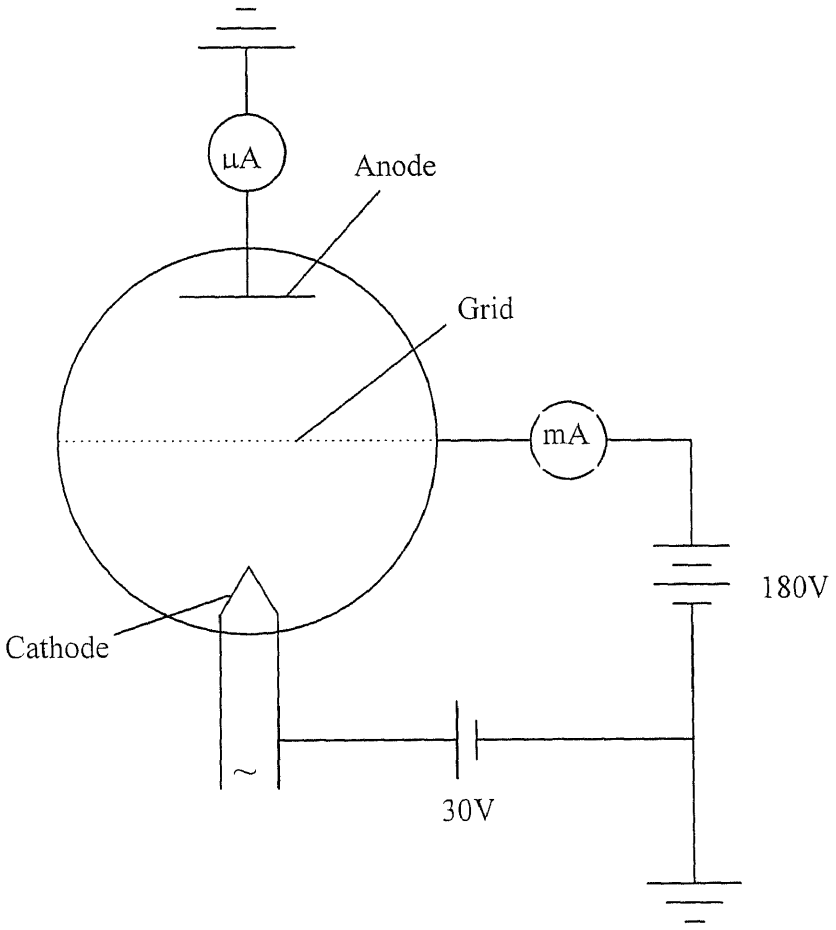

Figure 2.2 Electrical circuit to operate the conventional triode gauge.

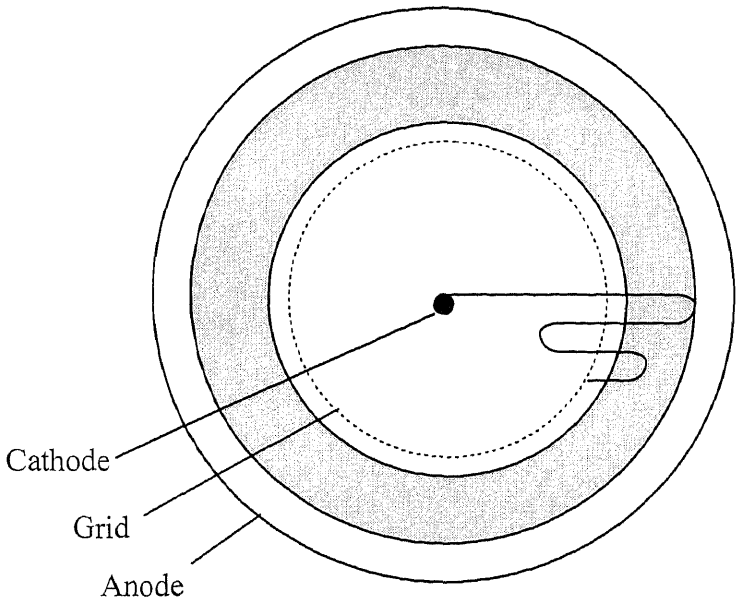

Figure 2.3 Schematic electron trajectory in a conventional triode gauge.

2.1.2 Cold Cathode Vacuum Gauge

The gauge tube illustrated in Figure 2.4 is the cold cathode vacuum gauge developed by Penning. In this gauge a pair of cathode plates is arranged on either side of a ring-shaped anode. A 2kV dc source in series with a resistor and an ammeter is connected to the electrodes, and a magnetic field is arranged parallel to the electrode axis. The arrangement of the electric and magnetic fields causes electrons to travel long distances in spiral paths before finally colliding with the anode. These long trajectories considerably enhance the ionization probability and result in a gauge with a much higher ionization efficiency than that without a magnetic field. The total current, which is the sum of the electron and positive ion currents, is so great that a current amplifier is not needed. Output currents of 1 to 5 mA/mTorr are typical [1-2].

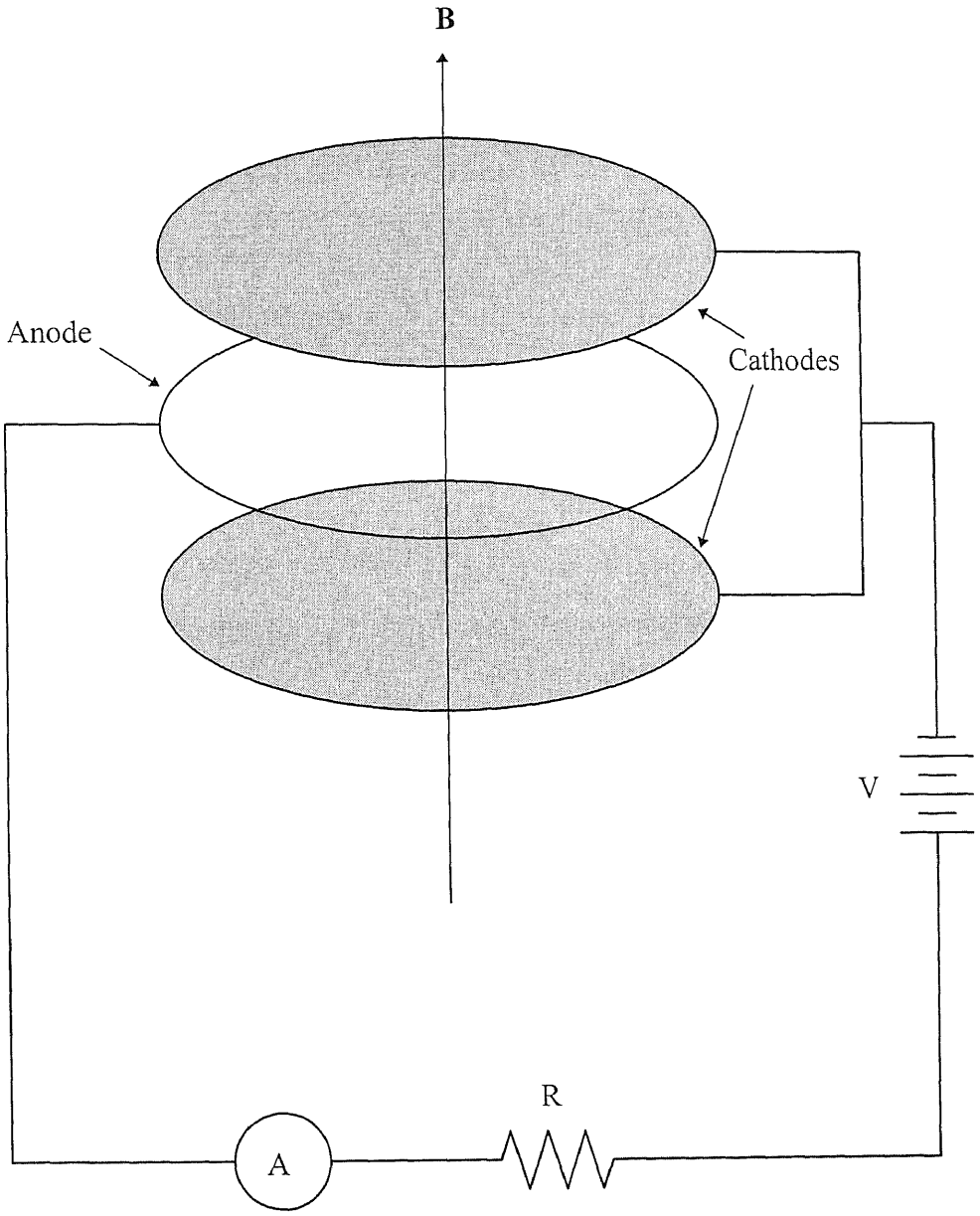

Figure 2.4 Penning type cold cathode gauge.

2.2 Mass Spectrometer

The second focus of this research is the design and fabrication of a microengineered mass spectrometer. Mass spectrometers are used to measure the ratio of mass to electric charge of a molecule or atom. There are several forms of mass spectrometer but the basic principle of operation is common: first the gas molecules are ionized, then accelerated and separated into groups according to their mass-to-charge values, and finally detected (Figure 2.5).

The means of ionization are fairly standard, the gas molecules being bombarded by electrons. The acceleration is done by electric field, while the separation is accomplished using magnetic deflection, resonance or time of flight techniques. A variety of methods have been developed for each of the three stages of particle identification. Other methods have been developed into portable instruments.

Among a variety of the commonly used mass spectrometers, the semicircular, homogeneous field design first reported by Dempster, is still widely employed either as a single magnetic analyzer, or in conjunction with electrostatic lenses. The microengineered mass spectrometer described in this dissertation is based on this mass separation method. Typical ion trajectories for the 180° magnet arrangement are shown in Figure 2.6, assuming a highly collimated ion beam.

Let singly charged ions be produced and accelerated through a potential V_c, thus acquiring a kinetic energy of magnitude eV_c. If this accelerating potential V_c is large compared with the initial energy distribution of the ions, we can assume that all ions enter the magnetic field with a discrete velocity which is given by

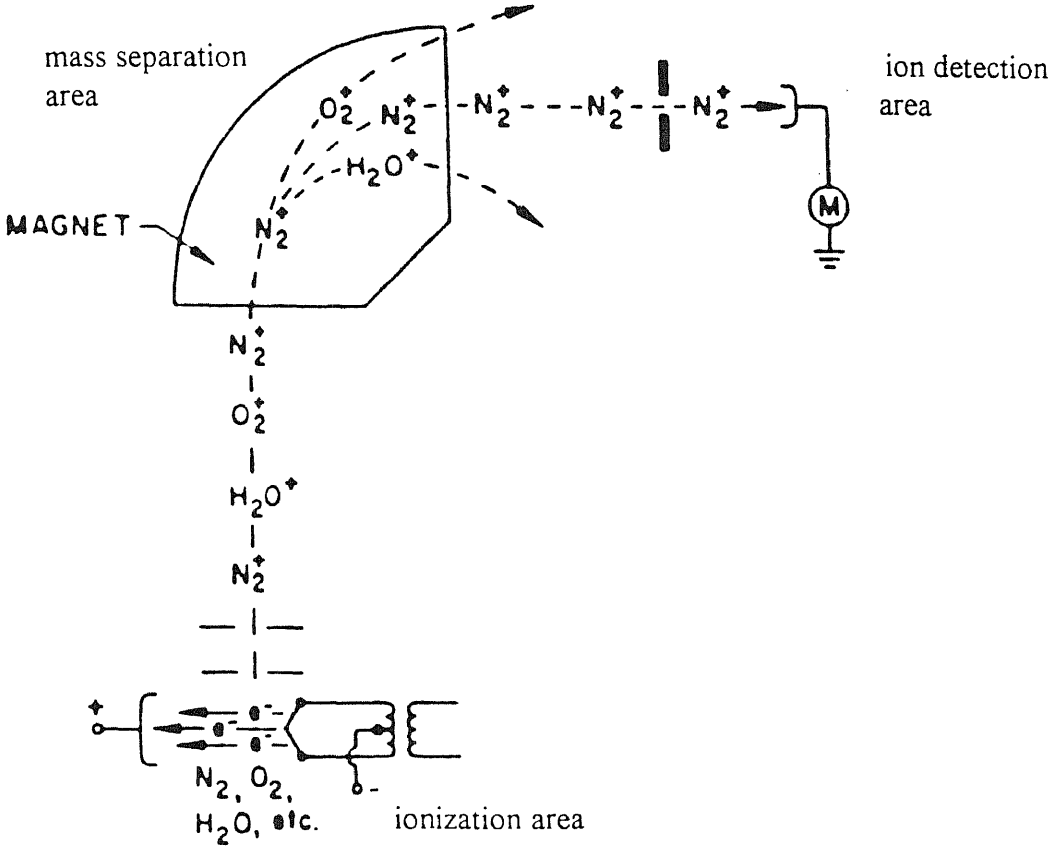

Figure 2.5 Functional drawing of a mass spectrometer shows ionization area, mass separation area, and ion detection area.

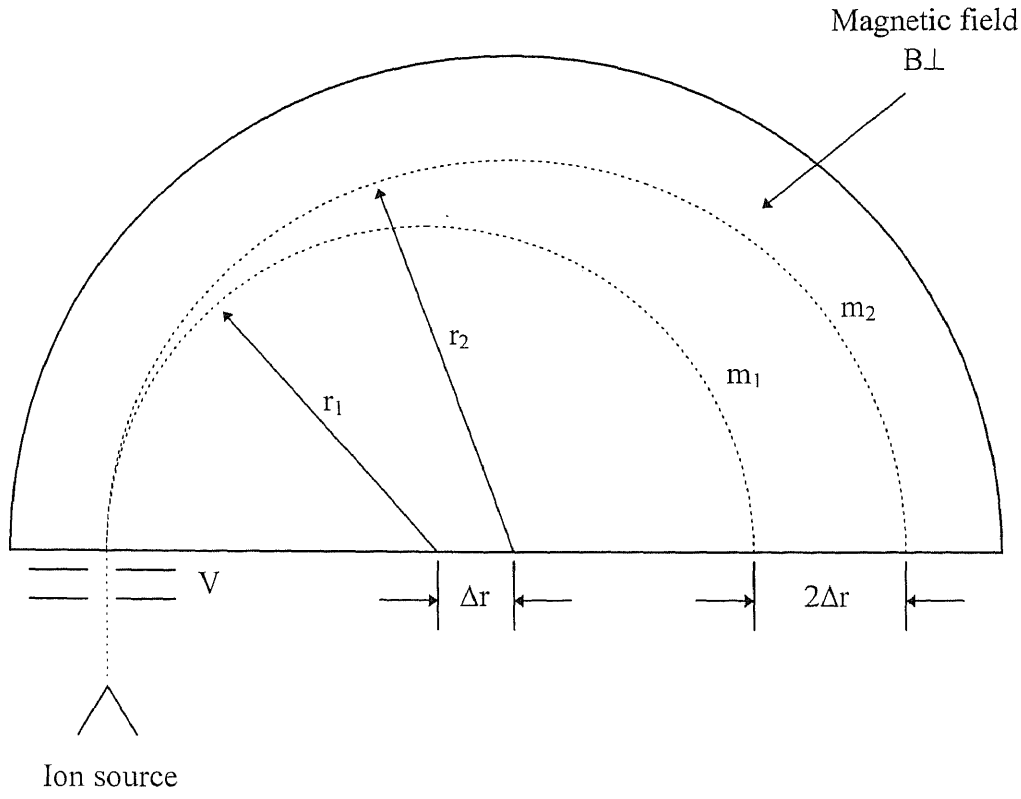

Figure 2.6 Ion paths in a homogeneous 180° magnetic sector.

$$eV_c = \frac{1}{2}mv^2, \text{ or } v = \sqrt{\frac{2eV_c}{m}} \tag{2.1}$$

where m is the mass of the ion, e is the electronic charge, and v is the velocity of the ion after acceleration. For positive ions having a charge state ζ (ζ=1,2,3...), where ζ denotes the number of electrons stripped from a neutral atom, the more general expression results:

$$\zeta eV_c = \frac{1}{2}mv^2. \tag{2.2}$$

If the magnetic field B is perpendicular to the velocity vector of the ions, the ions will be deflected into a circular orbit with radius r, resulting from the balancing of the centrifugal force with the Lorentz force $B\zeta ev$

$$B\zeta ev = \frac{mv^2}{r}. \tag{2.3}$$

Eliminating v from the above two equations yields the general expression relating the radius of curvature of an ion in a homogeneous magnetic field to the several other parameters:

$$r = \frac{1}{B}\left(\frac{2mV_c}{\zeta e}\right)^{1/2}. \tag{2.4}$$

If the magnetic field strength B is expressed in Gauss, m is given in atomic mass units, V_c is the accelerating potential in volts, and ζ is the multiplicity of electronic charge, then the radius of curvature r, in centimeters, is approximated by the relation

$$r = \frac{144}{B}\left(\frac{mV_c}{\zeta}\right)^{1/2}. \tag{2.5}$$

The above suggests that for ions accelerated through the same potential, those of large mass number will have a larger radius of curvature. It will also be noted that an ambiguity remains with respect to the mass number and charge state. A doubly-charged magnesium ion of mass 24 Mg^{24} will have approximately the same radius of curvature as will a carbon C^{12} atom that is only singly ionized. Therefore, unless the magnetic analyzer can resolve the small momentum difference corresponding to these two species, only a single peak will be observed at the mass-equals-12 spectral position. The equation can also be differentiated to yield an expression of the general form

$$\frac{2\Delta r}{r} = \frac{\Delta m}{m} + \frac{\Delta V_c}{V_c} - \frac{2\Delta B}{B}. \tag{2.6}$$

For a homogeneous magnetic field and ions having a negligible energy spread, the last two terms will vanish and the equation (2.6) reduces to

$$2\Delta r = \frac{\Delta m}{m} r. \tag{2.7}$$

The quantity $2\Delta r$ gives a measure of the mass dispersion, or the separation of resolved ions along the focal plane. Thus, in Figure 2.6, if r_1 and r_2 are the radii of curvature of masses m_1 and m_2, respectively, the mass dispersion of these two isotopes will result in a diameter difference

$$2(r_1 - r_2) = (\frac{m_1 - m_2}{m_1}) r_1 \tag{2.8}$$

For isotopes that differ by only one mass number ($\Delta m=1$), the mass dispersion D along the focal plane will have a magnitude

$$D = c\frac{r}{m} \tag{2.9}$$

where the unitless constant c will depend upon the magnetic sector angle. For the 180° sector, c will be 1, and

$$D = 2\Delta r = \frac{r}{m} \tag{2.10}$$

Thus the distance along the 180° focal plane between adjacent isotopes will increase directly with the radius of curvature, and it will be inversely proportional to the mass number. Hence analyzers with small radii of curvature and having a reasonable mass separation for light gases may be inadequate for the analysis of gases of high atomic mass number.

Although the 180° analyzer possesses good directional focusing properties, there are definite limitations on the sharpness of the line image, even if the ions are monoenergetic and the magnetic field is perfectly homogeneous. Consider Figure 2.7, in which ions leaving a source have a half-angle of divergence, α, and rays are drawn with equal radii from centers of circular orbits from points O, O', and O". When α is large, the central ray will not coincide with the peripheral rays, and at the 180° boundary the image width will be of magnitude $\alpha^2 r$. (At the 360° boundary, i.e., initial source position, this aberration will vanish, but so will all mass dispersion).

It is obvious that the greatest resolution of ions is obtained by using a deflection of 180°. However this requires a relatively large system and a magnet of large-pole-piece area since the field must be uniform over the whole ion path. More compact and lighter mass spectrometers with deflections of 120°, 90°, and 60° were built, but the resolution of these instruments is not as high as for those with 180° angular deflection.

Besides the single magnetic deflection type mentioned above there are other types of mass spectrometers: double-focusing spectrometer, multiple magnet system, the cycloidal spectrometer, cyclotron resonance spectrometer, the time-of-flight spectrometer, quadrupole spectrometer and special type spectrometers [3].

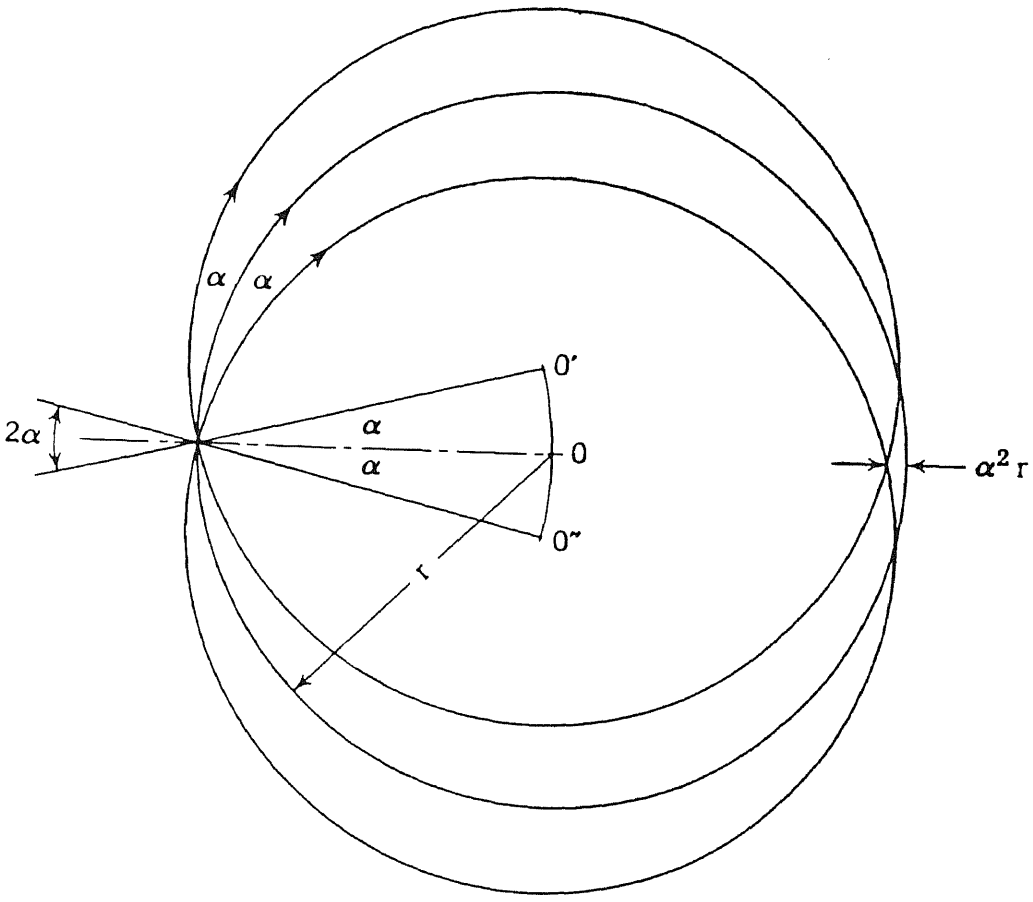

Figure 2.7 Angular aberration in the 180° sector

2.3 Basic Concepts of Vacuum and Gas Pressure

The field emission type sensors are operated in a high vacuum environment. A gaseous environment where pressure or density is below that of standard atmosphere is termed a vacuum. The physical quantity used to characterize such an environment is the gas pressure. Usually vacuum is obtained by removing gas from an airtight vessel by some means of pumping. In the absence of a gas load, the degree of vacuum in the vessel increases as the pressure of the residual gases decreases.

Generally speaking, pressure is a convenient parameter to characterize vacuum. However, below certain limits of gas rarefaction, pressure is not adequate to explain phenomena that take place in the vacuum, and other physical

quantities, such as the density of molecules and the mean free path, can characterize it more exactly. The meaning and magnitude of these quantities is given by the kinetic theory of gases. According to this theory, a gas is a collection of an enormous number of particles (molecules) moving along random directions, colliding with each other, and changing their direction of motion with each collision. For a gas sample of mass M, having a known absolute temperature T, and molecular weight m, the product of the pressure P and volume V is given by

$$PV = \frac{M}{m}RT \tag{2.11}$$

where M/m is the number of moles and R is an universal constant, $R = 62.36 \ \text{Torr} \cdot \text{liter} / \text{K} \cdot \text{mole}$. Equation (2.11) is the general gas law. The number of molecules n per unit volume is

$$n = \frac{M}{m} \cdot \frac{N_A}{V} \tag{2.12}$$

where N_A is the Avogadro's number, $N_A = 6.023 \times 10^{23}$ molec./mole.

From equations (2.11) and (2.12), n can be expressed as

$$n = \frac{N_A P}{RT}. \tag{2.13}$$

If P is expressed in Torr, and R in Torr·cm^3/K, the number of molecules per cm^3 is given by

$$n = \frac{6.023 \times 10^{23}}{6.236 \times 10^4} \cdot \frac{P}{T} = 9.656 \times 10^{18} \cdot \frac{P}{T} \quad (cm^{-3}). \tag{2.14}$$

Equation (2.13) can also be written

$$P = n \cdot \frac{R}{N_A} \cdot T = nkT \tag{2.15}$$

where k is the Boltzmann constant and expressed as $k=R/N_A=1.035\times10^{-22}$ Torr·liter/K·mole.

Gas molecules collide with each other. These collisions produce a distribution of velocities. Maxwell and Boltzmann expressed the distribution of the velocities by the relationship [4]

$$\frac{1}{n}\frac{dn}{dv} = f_v = \frac{4}{\pi^{1/2}}\left(\frac{m}{2kT}\right)^{3/2} v^2 \exp\left(\frac{-mv^2}{2kT}\right) \tag{2.16}$$

where f_v is the fractional number of molecules in the velocity range between v and v+dv, per unit of velocity range, and m is the mass of molecule. The distribution function of the velocities of molecules in the x direction is ginen as

$$\frac{1}{n}\frac{dn_x}{dv_x} = f_{v_x} = \left(\frac{m}{2\pi kT}\right)^{1/2} \exp\left(\frac{-mv_x^2}{2kT}\right). \tag{2.17}$$

The number of molecules striking a unit area of surface (perpendicular to the x direction), per unit time is given by

$$\phi = \int_0^\infty v_x dn_x. \tag{2.18}$$

The symbol ϕ is the incident flux density rate. By introducing dn_x from equation (2.17) into (2.18) and integrating, it results that

$$\phi = \frac{n}{2\pi^{1/2}}\left(\frac{2kT}{m}\right)^{1/2} \tag{2.19}$$

By using equation (2.14), the incident flux density rate ϕ becomes

$$\phi = 3.513 \times 10^{22} \cdot \frac{P}{(mT)^{1/2}} \quad (\text{molec./cm}^2\text{s}) \tag{2.20}$$

where P is in Torr, m is the molecular weight of the gas and T is the absolute temperature.

The average distance traversed by a molecule between successive collisions is its mean free path λ. A molecule having a diameter δ and a velocity v moves at a distance $v \cdot dt$ in the time dt. The molecule suffers a collision with another molecule when its center is within the distance δ of the center of another molecule, therefore sweeps out without collision a cylinder of diameter 2δ. This cylinder has a volume

$$dV = \frac{\pi}{4}(2\delta)^2 \, vdt. \tag{2.21}$$

Since there are n molecules per cm^3, the volume associated with one molecule is on the average $1/n$ cm^3. When the volume dV is equal to 1/n, it must contain on the average one other molecule, thus indicating that a collision has occurred. If τ=dt is the average time between collisions,

$$\frac{1}{n} = \pi\delta^2 v\tau \tag{2.22}$$

then the ballistic mean free path λ is

$$\lambda = v\tau = \frac{1}{\pi n\delta^2}. \tag{2.23}$$

If we consider the more realistic case, in which not only the reference molecule is in motion but also the others, then equation (2.23) must be re-written

$$\lambda = \frac{1}{\pi n\delta^2} \cdot \frac{v}{v_r} \tag{2.24}$$

where v is the absolute velocity, while v_r is relative velocity of the molecules.

When the Maxwell-Boltzmann distribution of velocities is also considered, it results in

$$\frac{v}{v_r} = \frac{1}{\sqrt{2}} \tag{2.25}$$

and

$$\lambda = \frac{1}{\sqrt{2}\pi n\delta^2}. \tag{2.26}$$

By using equation (2.14), λ becomes

$$\lambda = 2.33 \times 10^{-20} \cdot \frac{T}{\delta^2 P} \quad (\text{cm}) \tag{2.27}$$

where T is in K, δ in cm, and P in Torr.

Figure 2.8 illustrates the variation of the quantities expressed by Equations (2.14), (2.20), and (2.27) in different vacuum ranges. The calculated values of n, ϕ, and λ are shown in Table 2.1. These parameters are used to determine the sensitivity of the microengineered mass spectrometer device in chapter four.

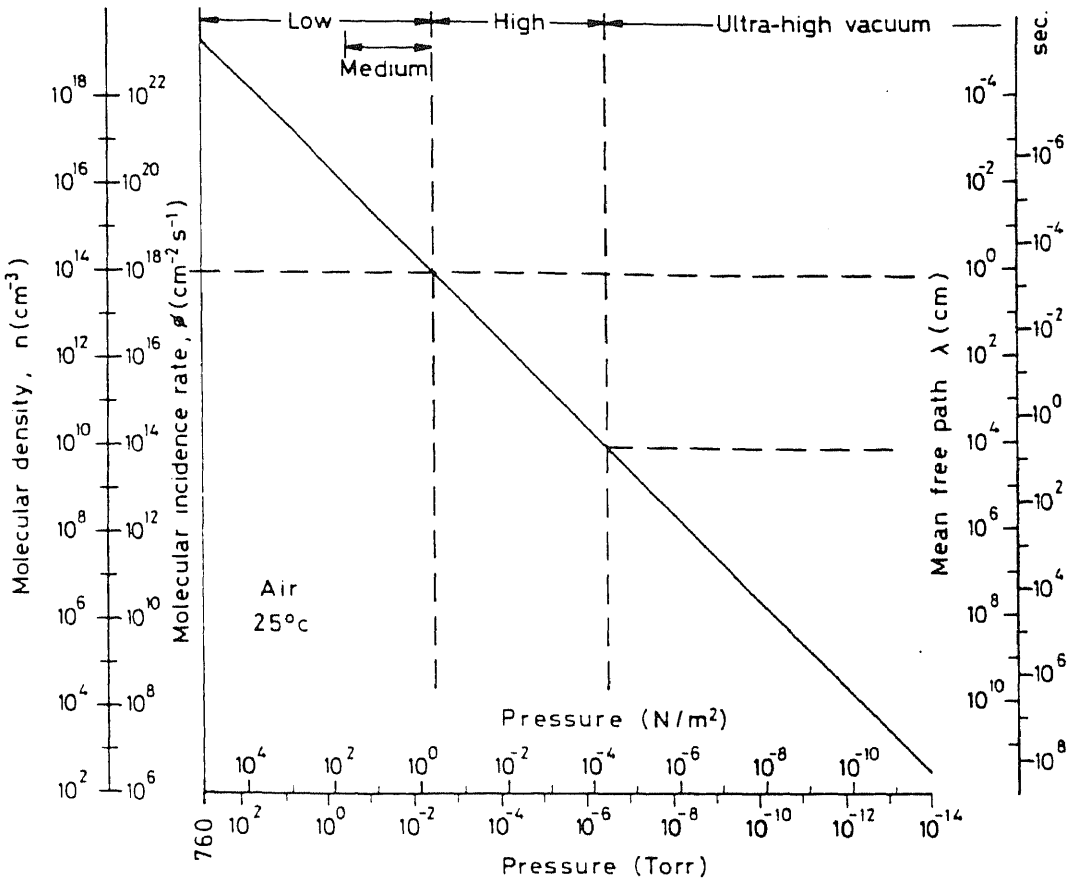

Figure 2.8 Variation of the number density of molecules n, ballistic mean free path λ, and molecular incidence rate ϕ as a function of pressure P [4].

Table 2.1 (a) Values of molecular density n, molecular incidence rate ϕ, and ballistic mean free path λ, as a function of pressure P, for air at 25°C [4].

P Torr	*n* molec/cm^3	ϕ molec/cm^2·sec	λ cm
760	2.46×10^{19}	2.88×10^{23}	6.7×10^{-6}
1	3.25×10^{16}	3.78×10^{20}	5.1×10^{-3}
10^{-3}	3.25×10^{13}	3.78×10^{17}	5.1
10^{-6}	3.25×10^{10}	3.78×10^{14}	5.1×10^{3}
10^{-9}	3.25×10^{7}	3.78×10^{11}	5.1×10^{6}
10^{-12}	3.25×10^{4}	3.78×10^{8}	5.1×10^{9}
10^{-15}	3.25×10	3.78×10^{5}	5.1×10^{12}

Table 2.1 (b) Values of ϕ, and λ for various gases at 25°C and 10^{-3} Torr [4].

Gas	ϕ molec/cm^2·sec	λ cm
H_2	14.4×10^{17}	9.3
He	10.4×10^{17}	14.7
N_2	3.85×10^{17}	5.0
O_2	3.60×10^{17}	5.4
A	3.22×10^{17}	5.3
Air	3.78×10^{17}	5.1
H_2O	4.80×10^{17}	3.4
CO_2	3.07×10^{17}	3.3

2.4 Ionization Source

Ions are created in mass spectrometers by impact ionization. Figure 2.9 is an ionization chamber that might be used in a mass spectrometer. Electrons from the filament or field emitter are drawn across the chamber to the anode. While crossing this space some of the electrons collide with gas molecules, strip off one or more of their electrons, and create positive ions.

The positive ion production is not the same for all gases. Table 2.2 gives the total positive ion cross sections relative to N_2 for several common gases at an ionizing energy of 70 eV. Although the ionization cross section does not peak at the same energy for all gases, it is generally greatest for most gases somewhere in the 50-to-150 eV range. The devices designed in this thesis operate at a potential between 50V and 100V and take advantage of the higher ion yield.

The ion production of each species is proportional to its density or partial pressure. Consider a sample of a gas mixture containing only equal portions of nitrogen, oxygen and hydrogen whose total pressure is 3×10^{-7} Torr. A mass scan of this mixture would show three main peaks of unequal amplitudes. All other factors being equal, the main oxygen peak would be slightly larger and the hydrogen peak about half as large as the nitrogen peak because of differences in relative sensitivity or ionizer yield. If, however, the total pressure of the gas mixture were doubled to 6×10^{-7} Torr, the amplitudes of each of the three main peaks would double. In other words, the instrument is linear with pressure. Linearity of the ionizer extends to a maximum total pressure of the order 10^{-5} Torr. At higher pressure, space charge effects and gas collisions become important. The ions produced in the space between the filament (or field emitter) and

anode are drawn out of that region, focused, and accelerated toward the mass separation space in any mass spectrometer.

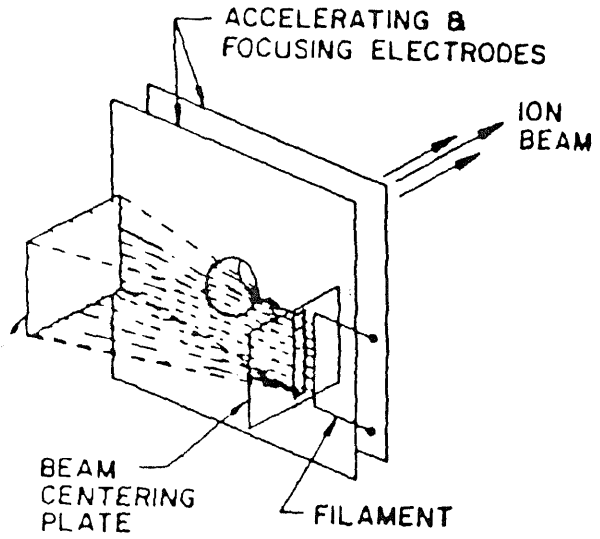

Figure 2.9 One form of an ionizing source used in a mass spectrometer [2].

Table 2.2 Experimental total ionization cross sections (70V) for selected gases normalized to nitrogen [2].

Gas	Relative Cross Section
H_2	0.42
He	0.14
CH_4	1.57
Ne	0.22
N_2	1.00
CO	1.07
C_2H_4	2.44
NO	1.25
O_2	1.02
Ar	1.19
CO_2	1.36
N_2O	1.48
Kr	1.81
Xe	2.20
SF_6	2.42

CHAPTER 3

FIELD EMISSION ELECTRON SOURCE

The electron source used in the microengineered pressure sensor and mass spectrometer devices is field emission from the silicon tip array. It is the most critical part in these micro devices. Field emission vacuum microelectronics technology is used in design and fabrication of the electron source. Vacuum microelectronics is a new field made possible by advances in microstructures and nanofabrication technology. Field emission vacuum microelectronics devices are novel electron tunneling devices for generating electron emission into a vacuum environment. Field emission vacuum microelectronics devices are further characterized by a wide operating temperature range, nuclear radiation immunity, higher electron emission current density, and lower power consumption than the thermionic emitters.

By using the field emission micro tip array, the dimension of the devices is significantly reduced to millimeter scale. Compared with thermionic devices (where electron emission is caused by thermal excitation), field emission vacuum microelectronics devices have four major advantages:

(1) The efficiency of thermionic emission is low and therefore thermionic devices consume more power.

(2) In thermionic devices, preheat time is needed in order to have a hot cathode and generate emission.

(3) Field emission devices permit higher integration than thermionic device since more heat dissipation occurs with thermionic devices and a larger surface and volume per device must be provided in order to maintain a reasonable operating temperature.

(4) Since the field emission devices operate at room temperature, less thermal degradation is expected.

However, the field emission devices have two major drawbacks:

(1) The emitters are vulnerable during the fabrication processing. Many processes often used in the typical semiconductor fabrication process such as blowing nitrogen to speed-up drying, or using oxygen plasma for descumming, will easily destroy the emitter tips.

(2) The emission is sensitive to the surface condition of the emitter. A clean emitter surface is generally required to have reliable field emission.

3.1 Field Emission Theory

Electron emission from a solid surface into a vacuum may be generated by several different ways such as thermionic emission (the electrons are thermally excited over the potential energy barrier), photoemission (the electrons are excited over the potential energy barrier by the incoming photons) and field emission [5-6]. The first field emission of electrons from sharp points was observed by Wood [7] in 1897. However, field emission was never well understood until Fowler and Nordheim applied quantum tunneling to explain and model this effect in 1928 [8]. In 1953, Dyke and Dolan reported the effect of morphology on emission and suggested that a vacuum arc was initiated by

field emission [9] [10]. In 1961, Shoulders proposed the first vacuum microelectronics devices [11].

In field emission, the electrons tunnel through the surface potential energy barrier, which has been sufficiently reduced by the influence of a strong electric field. The surface potential energy E for a typical value of Fermi level E_f and work function ϕ is illustrated in Figure 3.1 [12] where z is the distance from metal surface, z_c is the distance from the metal surface at which the surface barrier is maximum.

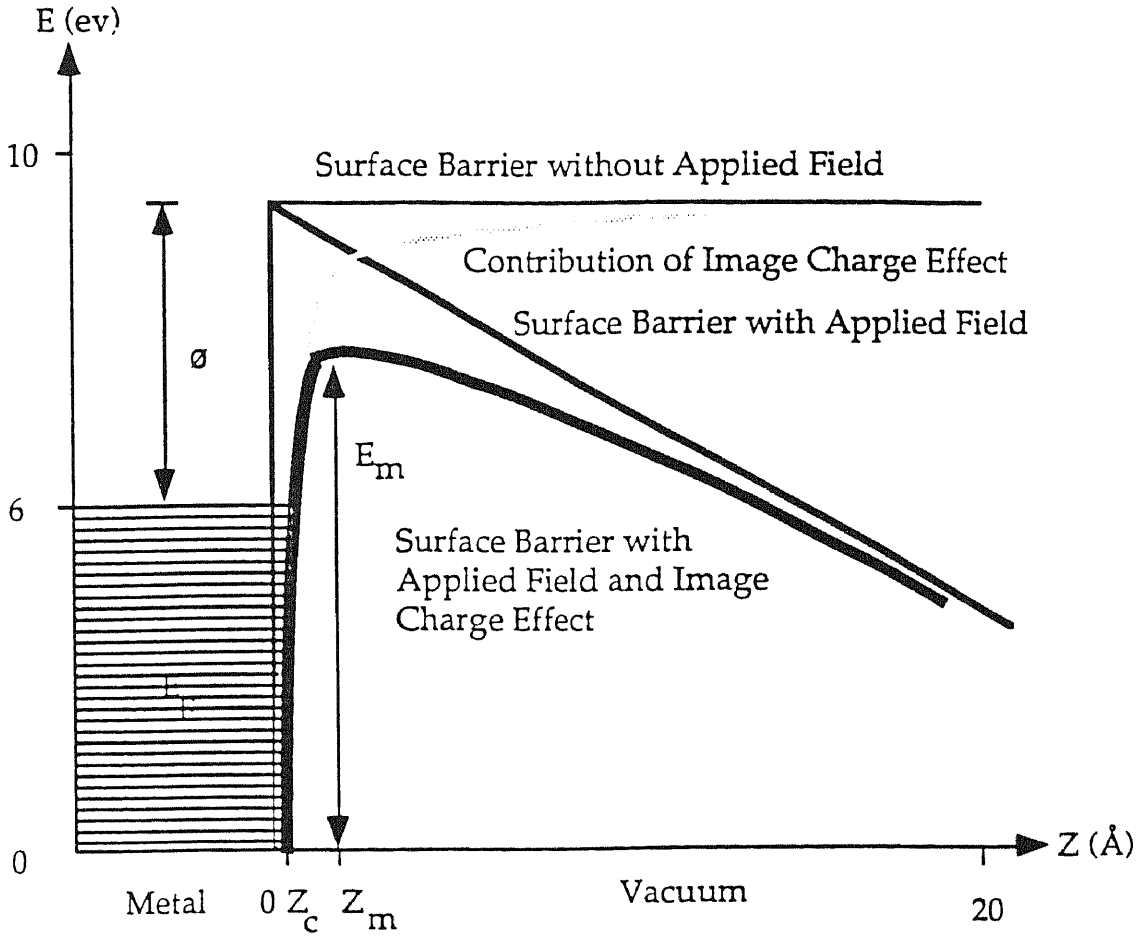

Figure 3.1 The surface potential energy diagram for electrons at a metal surface in the presence of a strong electric field (bold solid line). This shaped potential energy is the results of the image potential energy (light line) and the strong electric field (solid line).

An infinitely-deep metal surface from -∞ to 0 along the z axis is assumed in Figure 3.1. An electron situated at a distance z from a plane surface of perfect conductor is affected by the image force. Therefore, the potential energy of electrons on the vacuum side of the metal-vacuum interface is given by

$$V(z) = E_f + \phi - \frac{e^2}{4z} \tag{3.1}$$

where E_f is Fermi level and ϕ is work function and is valid for $z \geq 3$Å. The units of V(z), E_f and ϕ are eV.

For $z \leq 3$Å, the detailed shape of the potential barrier also depends on the metal surface [12]. When the external electric field is applied, the electron potential energy is given by

$$V(z) = E_f + \phi - \frac{e^2}{4z} - eFz, \qquad (z \geq z_c)$$

$$V(z) = 0, \qquad (z \leq z_c) \tag{3.2}$$

where z_c is determined by $V(z_0)=0$.

There are several equations describing the field. A general emission current density equation which was derived by Fowler and Nordheim in 1928 [8] is given by

$$J(F) = 6.2 \times 10^{-6} \frac{\sqrt{E_f}}{(\phi + E_f)\sqrt{\phi}} F^2 e^{-6.8\times10^7 \phi^{3/2}/F} \tag{3.3}$$

where the current density J is in A/cm^2, the electrical field F is in V/cm, and the Fermi level E_f and work function ϕ are in eV. Another equation is derived with consideration of the barrier lowering by the image effect [13] [14]. This modified Fowler-Nordheim equation is

$$J(F) = \frac{1.54 \times 10^{-6}}{\phi t^2(y)} F^2 e^{-6.83\times10^7 \phi^{3/2} v(y)/F} \tag{3.4}$$

where emission current density J is in A/cm^2, electric field F is in V/cm, work function ϕ is in eV, the Schottky lowing of the work function barrier $y=3.79\times10^{-4}F^{0.5}/\phi$. The function v(y) and t(y) have been computed and shown in Figure 3.2 [15]. The approximation value of 1.1 for $t^2(y)$ and $0.95-y^2$ for v(y) can be used in Equation 3.4. It is clear from Equation 3.3 or 3.4 that the electric field dominates the current density. It should be noted that a smaller radius of an emitter not only means higher emission current density J, but also indicates a smaller emitting area A. If the tip is too sharp, the emission current I may be decreased because of the smaller product of J and A. A simulation shows the maximum emission current is at r=10Å based on an extraction voltage of 30V, an extraction distance of 1μm and a work function of 4.01eV [16]. It should also be noted that the thermionic emission contribution to the emission current density becomes important when the temperature rises. In thermionic emission the metal is heated so that the electrons can be excited over the potential energy barrier. The equation of thermionic emission is given by

$$J(T) = 120T^2 e^{-\frac{\phi}{kT}} \tag{3.5}$$

where the emission density J is in A/cm^2, absolute temperature T is in °K, work function ϕ is in eV and Boltzmann constant k is 8.625×10^{-5} eV/°K [5]. For thermionic emission, temperature dominates the current density whereas electric field dominates the current density for field emission. Figure 3.3 shows the thermionic current emission and field emission regions for a range of temperature and applied field for a 4.5eV work function

emitter [12] [17]. This indicates that at sufficiently high field, the major emission is from field emission. But at sufficiently high temperature and low field, the major emission is from thermionic emission. Some improved Fowler-Nordheim equations for field emission from semiconductors have been reported [18].

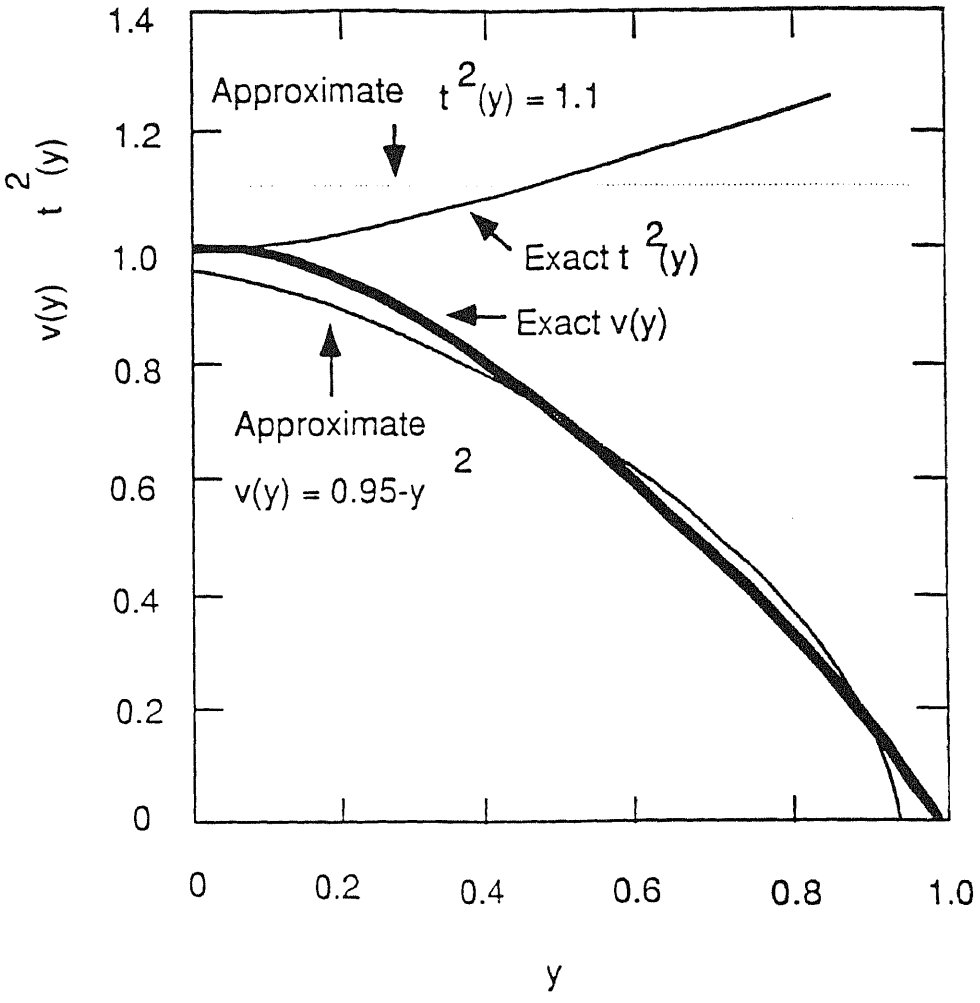

Figure 3.2 Comparison of approximate forms with exact solutions for the Fowler-Nordheim emission function v(y) and $t^2(y)$.

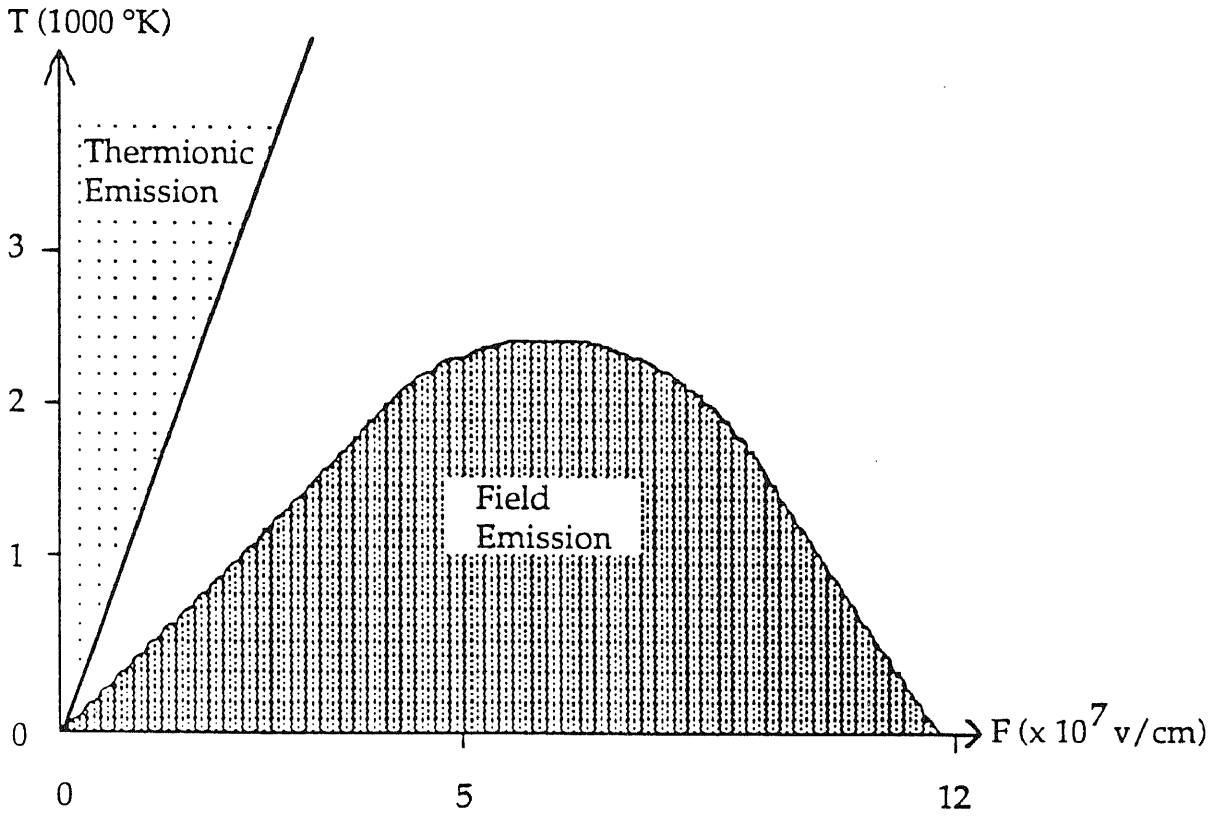

Figure 3.3 Thermionic emission and field emission regions of temperature and applied field for a 4.5 eV work function emitter.

3.2 Tip Emitting Area and Field Adjustment Factor

In order to analyze the Fowler-Nordheim behavior, it is desirable to derive the formulas for emitting area and field adjustment factor $\alpha=Fr/V$, where F is the electric field, r is the emitter radius and V is the applied voltage. The derivation starts from the Fowler-Nordheim equation [13]

$$J = \frac{AF^2}{\phi t1.1} e^{-B(0.95-y^2)\frac{\phi^{3/2}}{F}} \tag{3.6}$$

where J is in A/cm^2, F is in V/cm, emitter work function ϕ is in eV, $A=1.54\times10^{-6}$, $B=6.83\times10^{7}$, and Schottky lowering of the work function barrier $y=3.79\times10^{-4}F^{1/2}/\phi$. We may let $J=I/\beta r^2$ and use $F=V\alpha/r$, where βr^2 is the emitting area, α/r is the field conversion factor and I is the field emission current. Thus Equation (3.6) becomes

$$\frac{I}{\beta r^2} = \frac{AV^2\alpha^2}{1.1\phi r^2} e^{-\frac{0.95Br\phi^{3/2}}{V\alpha}} e^{\frac{1.436\times10^{-7}B}{\phi^{1/2}}} \tag{3.7}$$

The emitting area βr^2 can be obtained by rearranging Equation (3.7)

$$\beta r^2 = \frac{I}{V^2} \frac{1.1\phi r^2}{1.54\times10^{-6}\alpha^2} e^{\frac{6.49\times10^{7} r\phi^{3/2}}{V\alpha}} e^{-\frac{9.81}{\phi^{1/2}}} \tag{3.8}$$

Equation (3.8) can also be written as:

$$\log\frac{I}{V^2} = -5.85 + \log\frac{\alpha^2\beta}{\phi} + \frac{4.26}{\phi^{1/2}} - 2.819\times10^{7}\phi^{3/2}\frac{r}{V\alpha} \tag{3.9}$$

The slope S of the $\log(I/V^2)$ vs. $1/V$ plot is derived as follows:

$$S = \frac{d(\log\frac{I}{V^2})}{d(\frac{1}{V})} = \frac{-2.819\times10^{7} r\phi^{3/2}}{\alpha} \tag{3.10}$$

Thus the field conversion factor α can be obtained from the slope of the F-N plot since r and ϕ are known

$$\alpha = \frac{2.819 \times 10^7 \, r\phi^{3/2}}{S} \tag{3.11}$$

Then the emitting area βr^2 can be calculated from Equation (3.8). For an emitter with constant ϕ, r and α, the slope is constant during a change of voltage.

3.3 Factors Governing Field Emitter Operation

Electrical breakdown strength, the tip thermal stresses, and the maintenance of a clean emission surface are factors limiting maximum emitter current over a period of time. For this purpose, an ultra high vacuum (UHV) system is required. However, the operation of these devices in vacuum at pressure a high as 10^{-3} Torr has been demonstrated [19] [20].

Factors limiting the maximum current density of a field emitter array (FEA) for various tips were described by Utsumi [21]. One fundamental limit for current density in an FEA is thermal instability due to Joule (I^2R loss) heating by electrical current flowing in a nano scale emitter. The field emission current is approximated by $I=Jr^2$ where J and r are the field emission current density at the emitter and the emitter radius, respectively [21]. If I is too high, the Joule heating effect becomes serious and the emitter tip may be metallurgically damaged. Utsumi calculated the maximum emission current density before melting to be

$$J_{max} = 10^6 \frac{\sqrt{2T_M \sigma K}}{h} \tag{3.12}$$

where T_M is the melting point (°C), σ is electrical conductivity $(\Omega cm)^{-1}$, K is thermal conductivity, and h is the emitter height (cm) from the substrate. J is in A/cm^2 [21].

CHAPTER 4

DESIGN OF MICRO PRESSURE SENSORS AND MASS SPECTROMETER

4.1 Background and Applications

There exists a need for the microengineered gas sensors. In the past twenty years, the application of microelectronic technology to the fabrication of mechanical devices greatly stimulated research in semiconductor sensors. Such microfabricated devices are microengineered sensors. Micromachining technology takes advantage of the benefits of semiconductor technology to address the manufacturing and performance requirements of the sensor industry. The versatility of semiconducting materials and the miniaturization of VLSI techniques promise new sensors with better capabilities and improved performance-to-cost ratio over those of conventionally machined devices. The small size of the microengineered sensors not only contributes to their potentially low cost, but also allows them to be integrated with microelectronic circuits, the so-called integrated sensors; thus, further enhancing their performance [22]. The microengineered gas sensor devices described in this dissertation are the unique outgrowths of the semiconductor sensors. They are based on field emission cathodes for ionization. VLSI and MEMS process techniques are used to scale down the dimension of the existing ion vacuum gauge and mass spectrometer.

The objectives of this research are to develop a microengineered pressure sensor for innovating the existing ionization type pressure sensor, and to develop a portable, economical mass spectrometer system for in-situ gas detection and analyses. The uses of

the devices include high vacuum measurement, micromachined built-in pressure monitor, portable chemical gas composition analyzer, and hand-held air pollution detector.

4.2 Design of Microengineered Pressure Sensor

4.2.1 Description of Microengineered Pressure Sensor

This microengineered pressure sensor device consists of a electron source in the form of cathode tip array structure, an electron accelerating space which includes a gas ionization volume, and an ion collection electrode. The electron flux emitted from the cathode is accelerated to energies high enough to ionize neutral gas molecules in the vacuum of the ionization volume. The ionization rate of neutral gas molecules is proportional to the flux of neutral gas molecules entering from the surrounding vacuum. An ion collector maintained at a potential negative with respect to the ions supplies an electric current, I_{ion} to an outside current sensing circuit. The external ion current I_{ion} is proportional to the vacuum pressure being measured,

$$I_{ion}=q\eta\Phi \tag{5.1}$$

where q is the electron charge, η is the fraction-ionized factor, and Φ is flux rate of neutral gas molecules.

This microengineered pressure sensor device further utilizes a magnetic field created by a permanent magnet to lengthen the electron trajectory. By lengthening the electron trajectory path within the ionization volume, the fraction-ionized factor η can be greatly increased. It is desirable in this device for η to be as large as possible with the resulting increase in minimum detectable signal and signal-to-noise ratio.

This microengineered vacuum sensor device is used to measure gas pressure. It is to be fabricated on a silicon substrate approximately 1cm by 1cm. The top and side views of the device are shown in Figure 4.1.

In the central area of the substrate, there are the electron emitter ring and ion collector. The ion collector is surrounded by the cathode ring. The electron anode annular ring is used to create high electric field that accelerates the electrons. The base of the silicon substrate is a permanent magnet. A 500 Gauss magnetic field is suitable for this device.

The basic principle of operation is further summarized as follows: electrons are emitted from the cathode and enter the ionizing region. In this region, there exists the crossed electric and magnetic fields. The electric field is approximately parallel to the substrate, from the annular ring towards the center of the circle. The magnetic field set by a permanent magnet is perpendicular to the substrate. Due to the effect of Lorentz force, the electrons travel in the paths of many consecutive circles between the cathode and annular ring. The circular movement of electron will continue until the electron collides with the gas molecules and cause them to ionize. The endless electron trajectory results in a maximum number of ionization events as desired.

For hydrogen, for example, the ionization process is described by the equation of $H+e^{-}\rightarrow H^{+}+2e^{-}$. In order for this to occur, the electron must have sufficient energy to cause an electron to be released by the hydrogen atom. For this pressure sensor device, the above condition can be satisfied since the electric field is high enough to raise the energy level of each electron emitted from the cathode to ionize gas molecule.

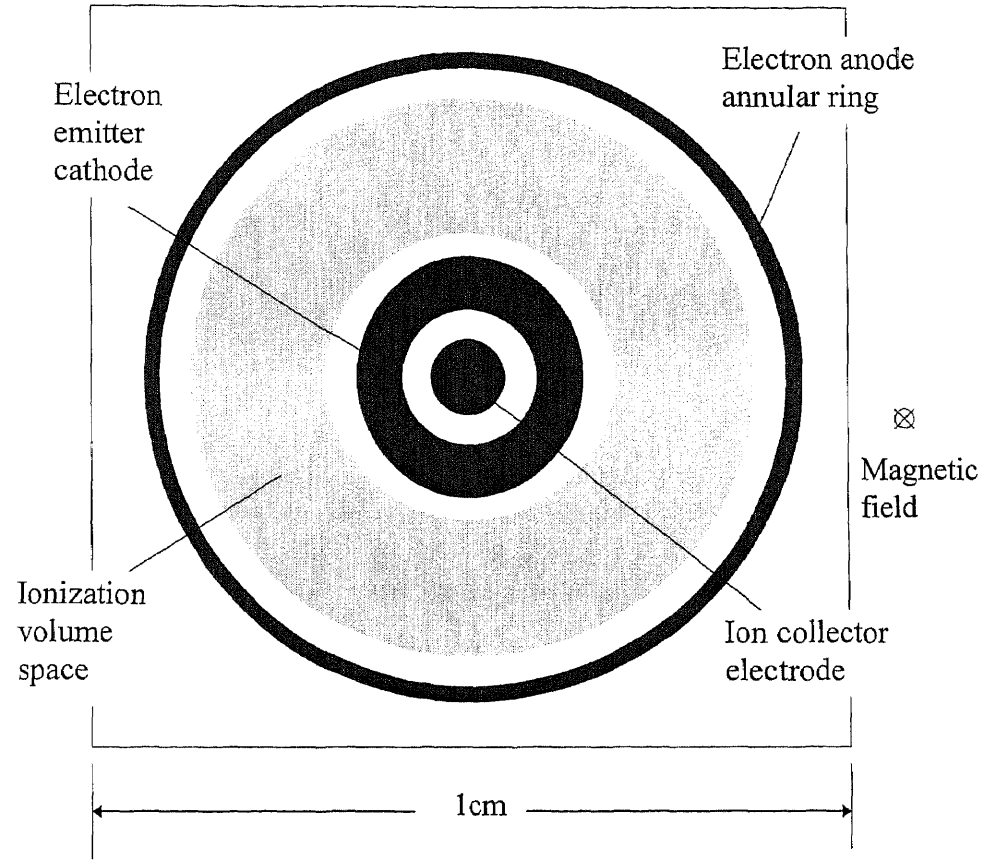

(a) Top view.

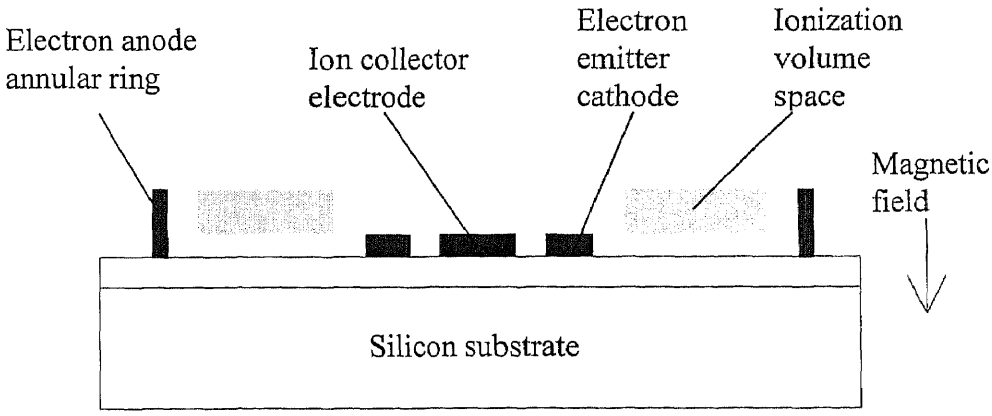

(b) Side view.

Figure 4.1 Microengineered vacuum sensor device.

Once ionization has occurred, the ions are attracted and collected by the ion collector which is biased at a potential negative with respect to the positive ions.

According to the general gas law, the gas pressure P is proportional to the density of gas molecules n. From the ionization theory we know that ion current I_{ion} is also proportional to n. Therefore, pressure P becomes proportional to I_{ion}. By detecting the ion current I_{ion}, the pressure P is measured.

4.2.2 Simulation of Microengineered Pressure Sensor

Figures 4.2-4.5 are operational simulations of this microengineered pressure sensor device. The computer program SIMION is employed to simulate the trajectories.

SIMION is an electrostatic lens and design program [23]. In SIMION, an electrostatic lens is defined as a 2-dimensioned electrostatic potential array containing both electrode and non-electrode points. The potential array is refined using over-relaxation methods allowing voltage contours and ion trajectories to be computed and plotted. Magnetic field can also be specified for computing ion trajectories in many electrostatic and magnetic field environments.

Figure 4.2 shows the trajectory of a typical electron emitted from a cathode tip in the central device area. There will be millions of electrons with similarly shaped trajectories forming an electron "cloud" around the cathode. The voltage applied on the anode (annular ring) is V_a=1000V. The cathode is grounded. The applied magnetic field B is 500 Gauss. The initial electron energy is W_i=0. The electron trajectory is extremely long. It is unlikely that it gets collected at the anode unless it collides with gas molecule.

When the anode voltage V_a is decreased to 500V, the radius of the circular trajectory becomes smaller (Figure 4.3).

On the other hand, the radius of the electron circular trajectory is increased with a reduction of applied magnetic field. Figure 4.4 shows the electron trajectory with the magnetic field reduced to 400 Gauss. If the applied magnetic field is further reduced, the electron will impact the anode where collection occurs immediately.

Figure 4.5 shows the side view of ion trajectories. The ions created in the active ionizing volume are collected by the ion collector in the central area and measured by the electrometer connected to the ion collector. An example of an appropriate measuring circuit is shown in Figure 4.6.

It should be noted that the simulation results of the electron trajectory may not be very accurate. The simulated electric field near the electrodes is distorted because the electrodes consist of squares and their edges are not smooth. In real situations, the electrons emitted from the tips may not travel many consecutive circles. When electrons travel a circle and are close to gate electrode, their kinetic energy become so small that most of them will be collected at the end of the first circle by the positively biased gate. To verify the accuracy of the SIMION, the electron trajectories in Figure 4.2, 4.3 and 4.4 were reversed (the starting and ending points were replaced each other) and the results remained unchanged. This suggests that despite the shortcomings of the simulation, the calculated electron trajectories may be fairly reliable. On the other hand, SIMION is a 2-D program and cannot describe a 3-D continuing trajectory where in fact the electrons are not in the plane of the cathode. Some electrons may be accelerated by the electric field which is perpendicular to the chip (though this field is small compared to the electric field

which is parallel to chip), and exit the ionizing volume. The electron trajectories shown in Figures 4.3, 4.3 and 4.4 just represent the ideal situations. In Chapter 6, the experimental and theoretical data will be compared and the discrepancy will be explained.

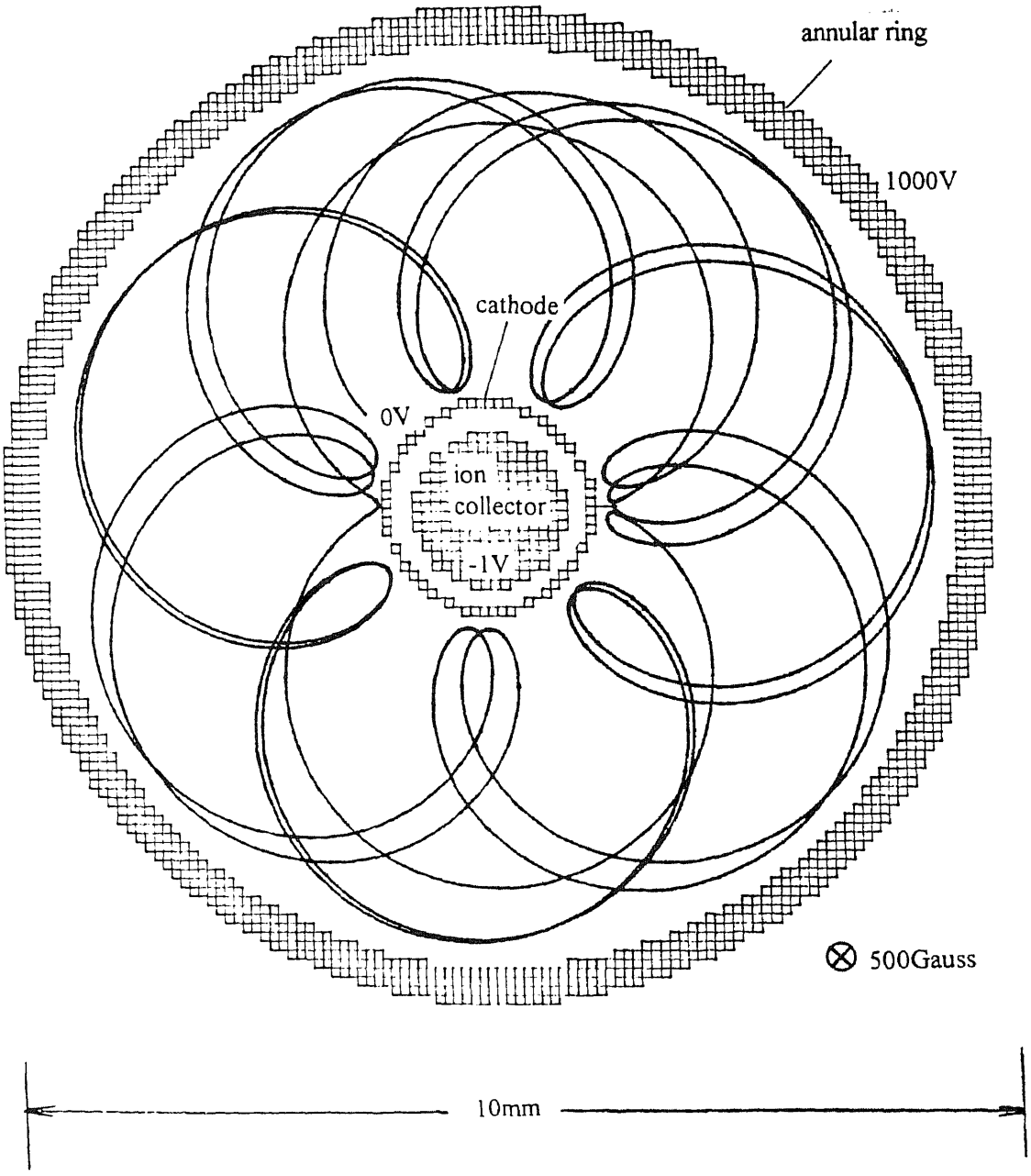

Figure 4.2 Electron trajectory (top view). V_a=1000V, B=500 Gauss.

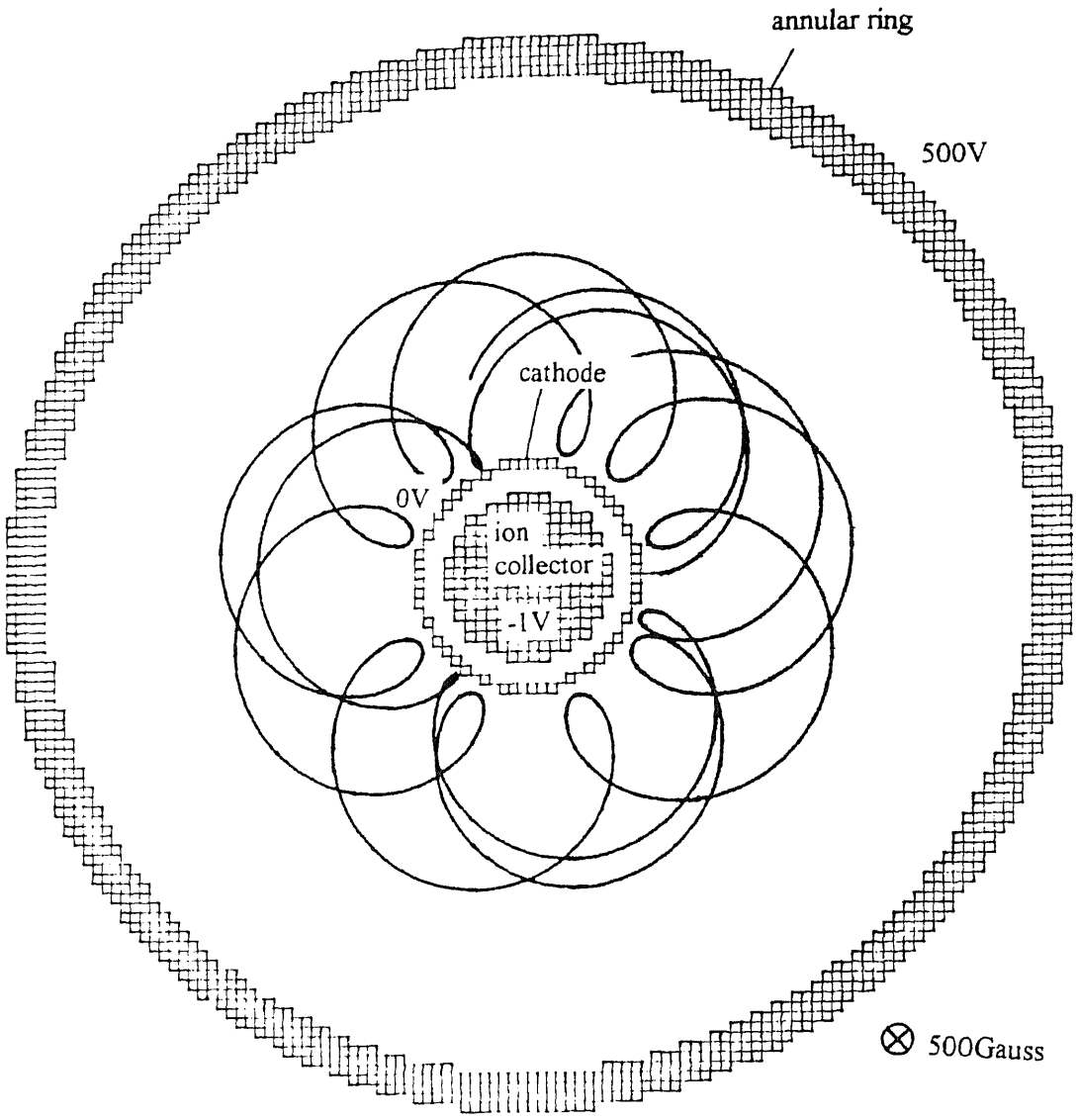

Figure 4.3 Electron trajectory (top view). V_a=500V, B=500 Gauss.

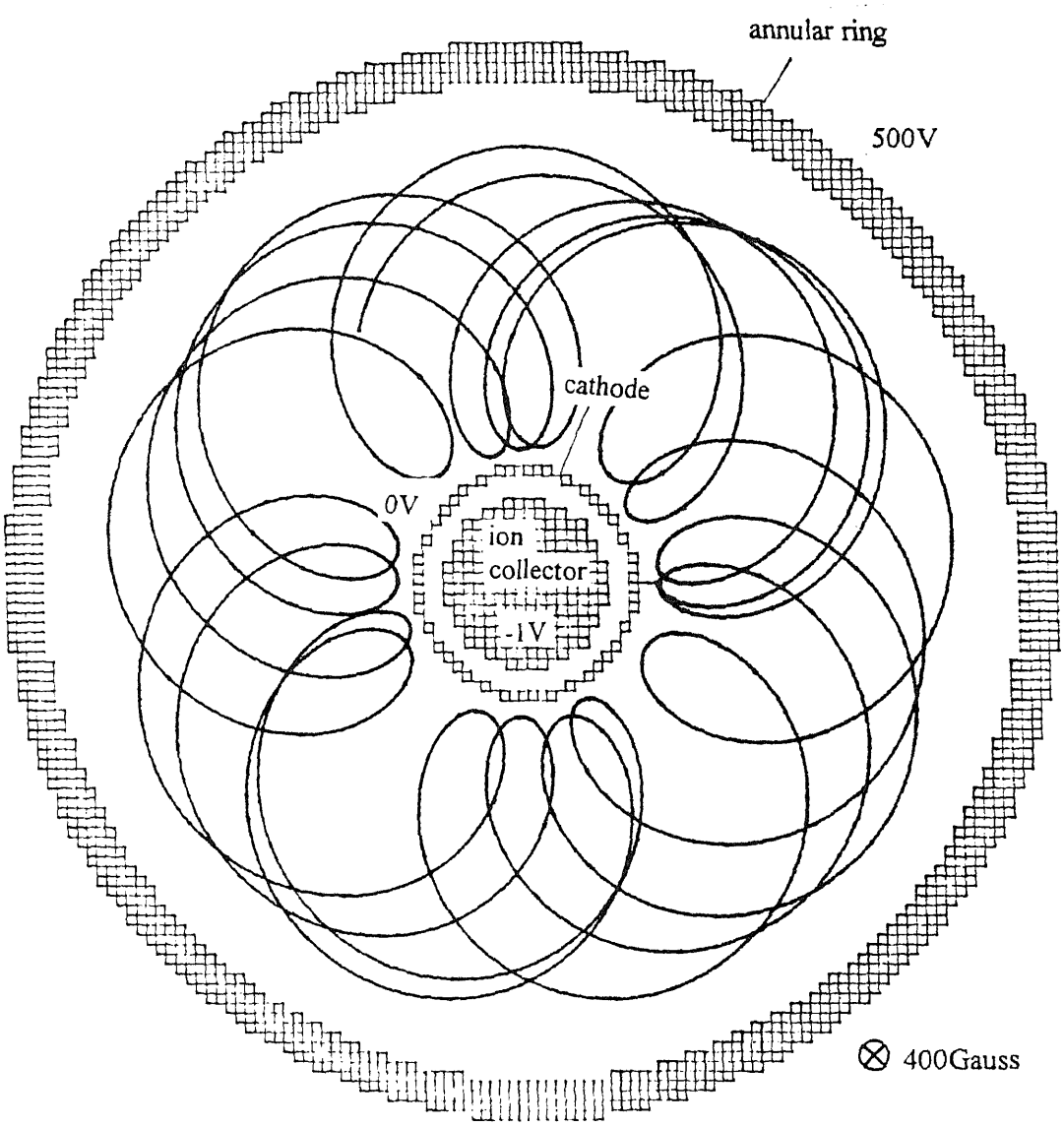

Figure 4.4 Electron trajectory (top view). V_a=500V, B=400 Gauss.

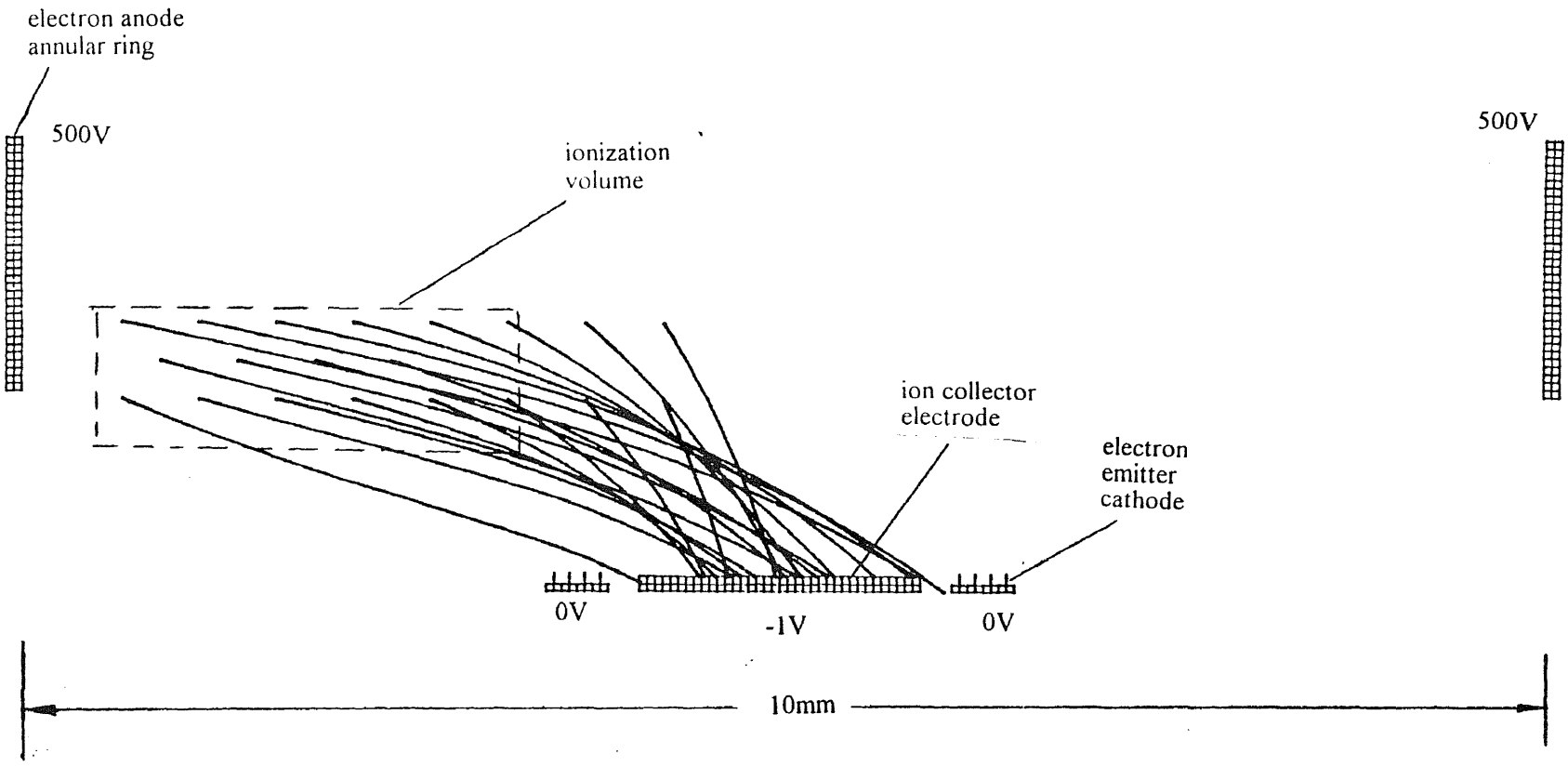

Figure 4.5 Ion trajectories (side view).

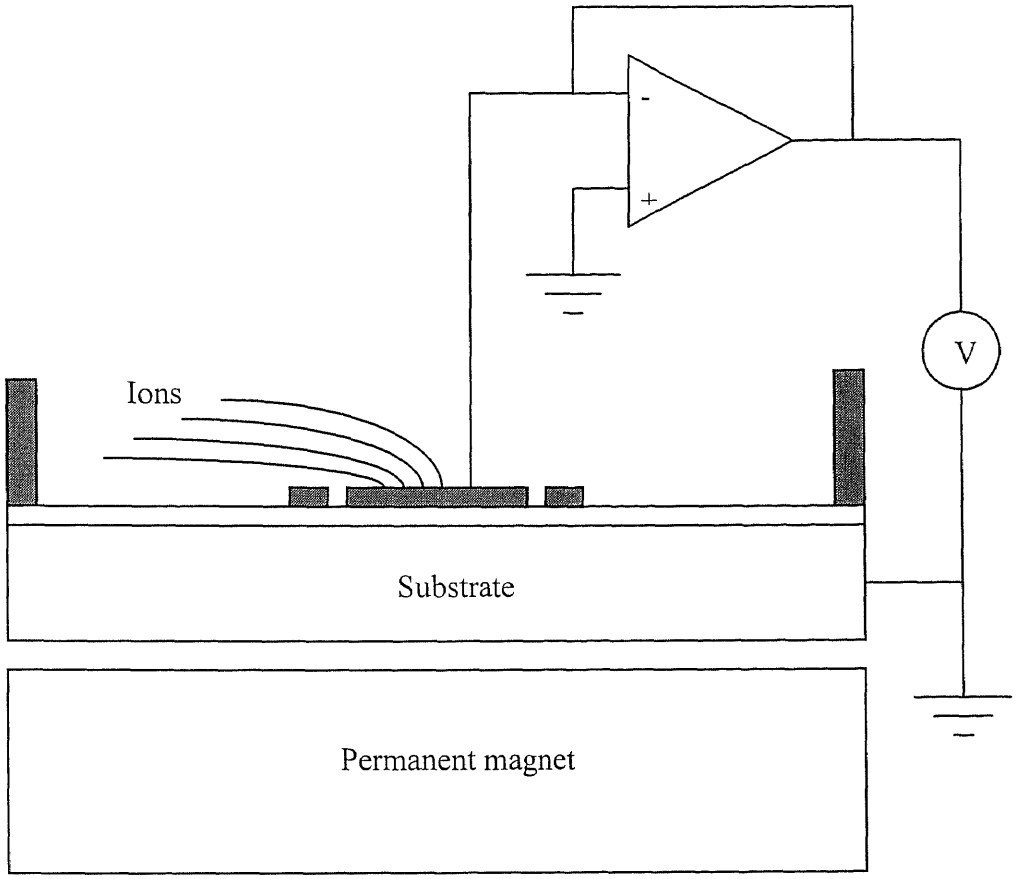

Figure 4.6 An example of ion current measuring circuit.

4.3 Device Parameter Modeling

An important parameter in designing the microengineered pressure sensor device is the sensitivity. The minimum detectable gas pressure is determined by the device sensitivity. The sensitivity is defined as [24] the quotient of the ion current at the collector and the pressure of the gas present in the ion source. The calculation is based upon molecular ionization theory.

When an electron is moving with a velocity v and then collides with an atom, kinetic energy is exchanged. If no excitation or ionization results, such a collision is an elastic collision. The collision becomes inelastic if the gas atom or molecule is excited or ionized by acquiring energy from the incident electron. Since there is a large number of particles in a gas and the characteristics of their paths cannot be determined, the collision frequency cannot be calculated or measured at any given instant. However, because of the very large number of molecules present, it can be assumed that when the system is in equilibrium, they are uniformly distributed in space, and their velocities are distributed according to the Maxwell-Boltzmann law. Under these conditions, the fluctuations in the frequency of collisions about a mean value are very small. When an electron is injected into the gas with a velocity v, the probability of a collision of a given type occurring is

$$dv = n\sigma \cdot dx \tag{4.2}$$

where n is the number of particles per unit volume of gas, σ is the cross section of the collision, and dx is the distance traveled in the gas. The mean free path λ is the reciprocal of the total cross section $n\sigma$,

$$\lambda = \frac{1}{n\sigma}. \tag{4.3}$$

If an electron beam flux rate N (electrons/sec) is introduced into the gas, then the average number of collisions dN in a distance dx will be approximately

$$dN = N \cdot d\varpi = Nn\sigma \cdot dx. \tag{4.4}$$

The concept of collision cross section can be made useful in describing the impact process and its products. If the electrons undergo $n\sigma$ collisions per unit path, some collisions will be elastic, and another portion will be inelastic which will ionize or excite the molecules impacted. The total number of collisions per unit length is [25-26]

$$\frac{dN}{dx} = Nn\sigma = Nn(\sigma_{el} + \sigma_{ion} + \sigma_{ex}) \tag{4.5}$$

where σ_{el}, σ_{ion}, and σ_{ex} are cross sections for elastic, ionizing, and exciting collisions respectively. The number of ionizing collisions per unit length is

$$\frac{dN_{ion}}{dx} = Nn\sigma_{ion}. \tag{4.6}$$

The fraction of collision events that are ionizing f_{ion} is obtained by dividing the number of ionizing collisions $n\sigma_{ion}$ by the total number of collisions $n\sigma$. Thus

$$f_{ion} = \frac{n\sigma_{ion}}{n\sigma} = \frac{\sigma_{ion}}{\sigma} = \frac{\lambda}{\lambda_{ion}} \tag{4.7}$$

where $\sigma=\sigma_{el}+\sigma_{ion}+\sigma_{ex}$.

The values of the ionization cross section σ_{ion} for the rare gases, resulting from collision with electrons of energies between 10eV and 100eV are given in Figure 4.7 where a_0 is about 0.05nm. The ionization cross sections are energy dependent and the maximum values occur between 80eV and 200eV, above which the cross section decreases quite rapidly. The increase in cross section is much more rapid between 10eV and 25eV. These curves show that cross sections increase as the atomic size of the atom

increases. The ionization cross section σ_{ion} for the common gases N_2, O_2, and H_2, is given in Figure 4.8 for comparison. These curves exhibit exactly the same features as those of the rare gases.

The sensitivity of the microengineered pressure sensor device can be calculated by using the discussed ionization cross section. The beam of N electrons per second emitted from the array of cathode tips travels in the paths of many consecutive circles between the cathode and annular ring. The average number of ionizing collisions Ω between electrons and molecules per second is

$$\Omega = Nn\sigma_{ion}l \tag{4.8}$$

where n is the density of gas molecules, N is the electron flux rate (total number of electrons/sec emitted from the cathode), and l is the average distance each electron travels in the ionizing region. Assuming all ions are collected by the ion collector, then the total ion current I_{ion} is

$$I_{ion} = Nqn\sigma_{ion}l \tag{4.9}$$

where q is the charge of the electron. Since N·q is the total cathode current I_e, equation (4.9) becomes

$$I_{ion} = nI_e\sigma_{ion}l. \tag{4.10}$$

The ion current I_{ion} can be related to the partial pressure P of the gas species using equation (2.14) to substitute for n. The ion current I_{ion} becomes

$$I_{ion} = 9.656 \times 10^{18} \frac{P}{T} I_e\sigma_{ion}l \tag{4.11}$$

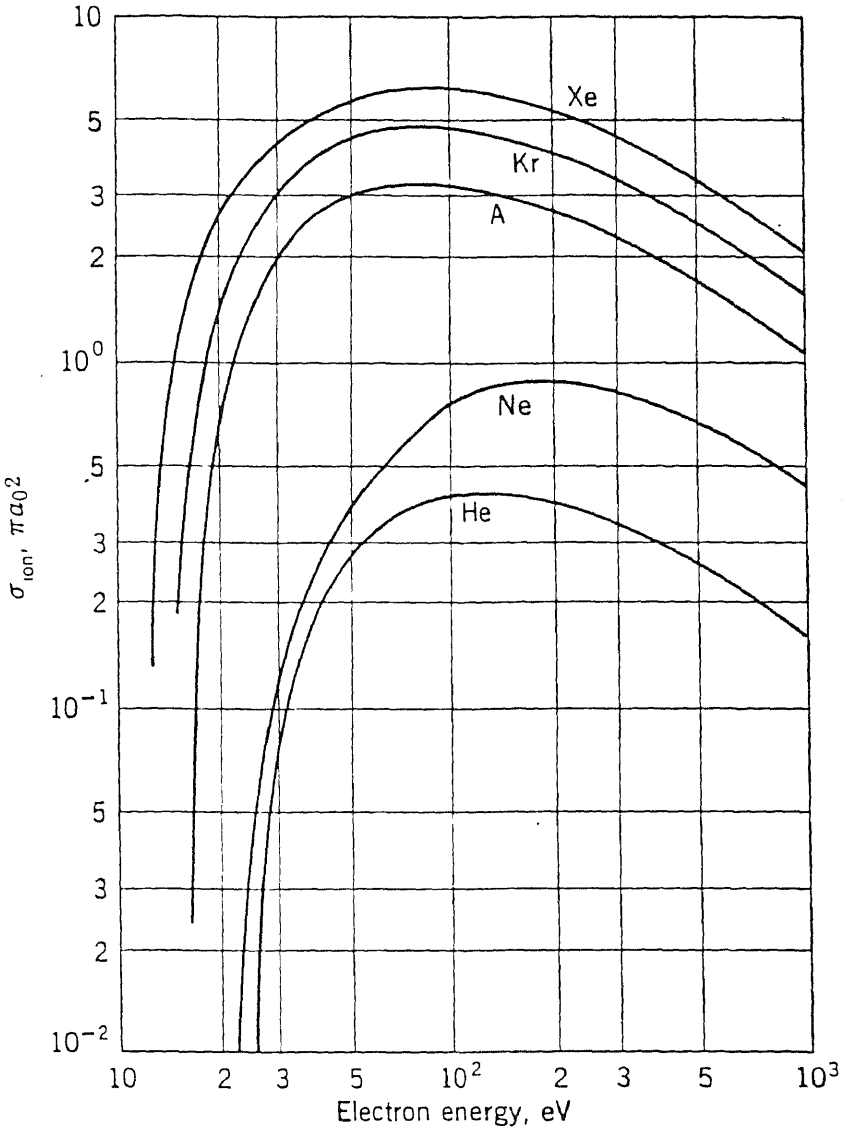

Figure 4.7 Ionization cross section σ_{ion} for the rare gases due to electron impact given in units of πa_0^2, where $\pi a_0^2 = 8.82 \times 10^{-17}$ cm^2, a is the radius of H-atom in ground state a≈0.05nm [25].

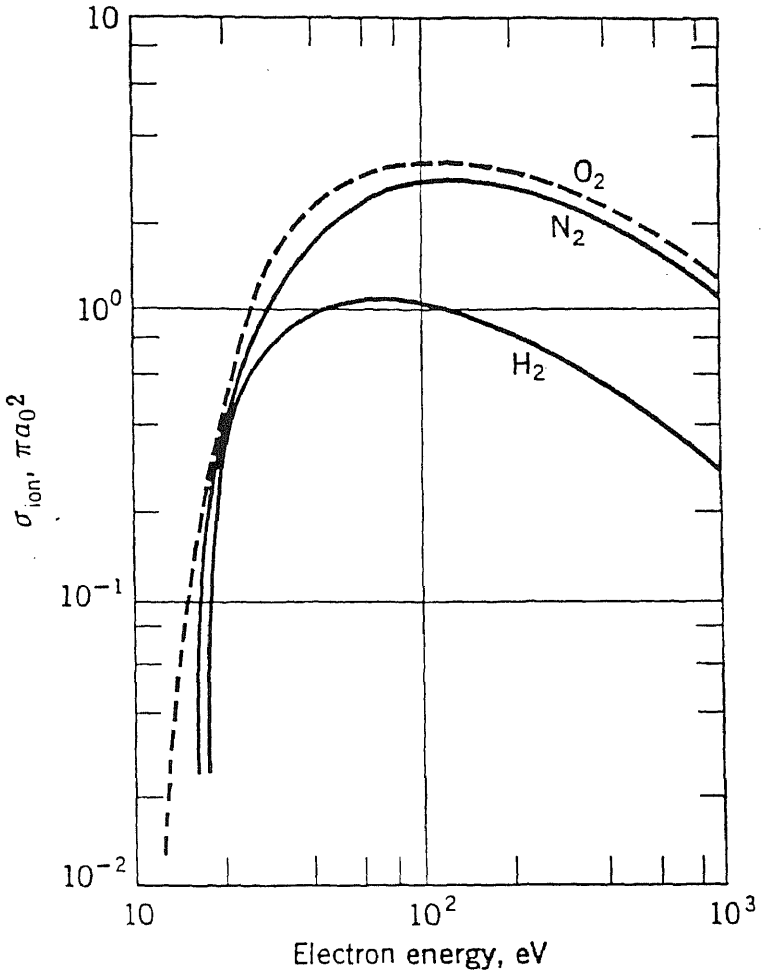

Figure 4.8 Ionization cross section σ_{ion} for O_2, N_2, and H_2 due to electron impact given in units of πa_0^2 [25].

where P is expressed in Torr, T is the absolute temperature in °K, σ_{ion} is in cm^2, and l is in cm.

Conversely, if $I_{ion,min}$ is the minimum detectable current for the ion collector, then the minimum detectable pressure P_{min} becomes

$$P_{min} = 1.0356 \times 10^{-19} \frac{I_{ion,min} T}{I_e \sigma_{ion} l}. \tag{4.12}$$

Another important performance parameter is the ionization efficiency η in the region of the cathode. It is defined as the ratio of the average number of ions created in the active ionizing volume per second I_{ion}/q to the total number of molecules entering this volume per second Φ

$$\eta = \frac{I_{ion}}{q\Phi} \tag{4.13}$$

From equation (2.20), the molecular flux rate Φ becomes

$$\Phi = \phi S = 3.513 \times 10^{22} \cdot \frac{PS}{(mT)^{1/2}} \tag{4.14}$$

where P is in Torr, m is the gas molecular weight, S is in cm^2, and T is the absolute temperature. Substituting equations (4.11) and (4.14) into (4.13), one obtains

$$\eta = \frac{9.656 \times 10^{18} \frac{P}{T} \cdot \frac{I_e}{q} \cdot \sigma_{ion} \cdot l}{3.513 \times 10^{22} \frac{PS}{(mT)^{1/2}}} = 2.75 \times 10^{-4} \left(\frac{m}{T}\right)^{1/2} \frac{I_e \sigma_{ion} l}{qS} \tag{4.15}$$

where I_e is the total cathode current, q is electron charge, and l is the average distance that each electron travels (in cm). This efficiency is a small value and is due to the small cathode current. It can be concluded that cathode electron current determines the

ionization efficiency. The minimum detectable partial pressure P_{min} can be reduced significantly by increasing the cathode electron current I_e. This can be seen by inspection of equation (4.12).

The sensitivity of this microengineered pressure sensor device γ is

$$\gamma = \frac{\text{ion current}}{\text{pressure}} = \frac{I_{ion}}{P} = 9.656 \times 10^{18} \frac{I_e \sigma_{ion} l}{T} \text{ (A/Torr)}. \qquad (4.16)$$

The above equations will be used to analyze the test results in Chapter six.

4.4 Design of Microengineered Mass Spectrometer

4.4.1 Description of Microengineered Mass Spectrometer

This mass spectrometer device uses planar geometry [27]. It is to be fabricated on two silicon substrates approximately 1cm by 1cm, one is used as the electron source and the other as the anode to collect the ions. It utilizes an electrostatic and a magnetic field to have the ions with different masses separated and collected by adjacent and coplanar anodes. A 3000 Gauss magnetic field permits collection of ions of up to approximately 222amu (radon) for the special dimensions used. Power supply voltage levels are 0 and V_a. For static magnetic fields of 3000 Gauss, the required value for V_a is 50V. Schematic diagrams of this device are shown in Figure 4.9. Chip A is approximately 1cm by 1cm. There is a strip of tip arrays about 1cm by 0.2cm on chip A. The total number of tips is about 7,000. Chip B measures 1cm by 1.5cm. There are several ion collectors on this chip. Each collector is used for a specific molecular weight of singly ionized gas ions.

The principle of operation is as follows: The electrons are emitted from the cathode tips and enter what will be referred to as the "active region". In the "active

region", the electrons accelerated by electric field, collide with gas molecules and cause them to be ionized. For hydrogen, for example, the ionization process for single ionization is,

$$H + e^- \rightarrow H^+ + 2e^-.$$

In order for this occur, the incident electrons must have sufficient energy to cause an electron to be released by hydrogen atom. This minimum energy is known as the ionization energy or ionization potential of the atom. For hydrogen, there is only a single electron present, and therefore no more than one can possibly be liberated. However, for atoms with more than one electron, it is possible for multiple ionization to occur. The energy required for the second ionization is in general higher than that required for the first, which means that a second ionization is less likely to occur than the first. Once ionization has occurred, the ions are accelerated by the electric field set up by the electrodes, and are caused to move in a curved trajectory by a combination of the electric field and an applied magnetic field. Finally, the separated ions are collected on the ion collectors (anode). The location of these collectors depends on the computer simulation result of ion trajectories.

As mentioned in chapter two, the mass spectrometers do not actually respond to mass, but rather to the ratio of mass to charge. For this reason, it is possible that if a given mass particle were ionized twice, it would look the same to the mass spectrometer as a singly ionized particle of half its mass. However, since the second ionization energies are higher than the first [28], this situation has a much lower probability. The design of this device is such that the electrons cannot in most cases attain enough energy to cause a second ionization.

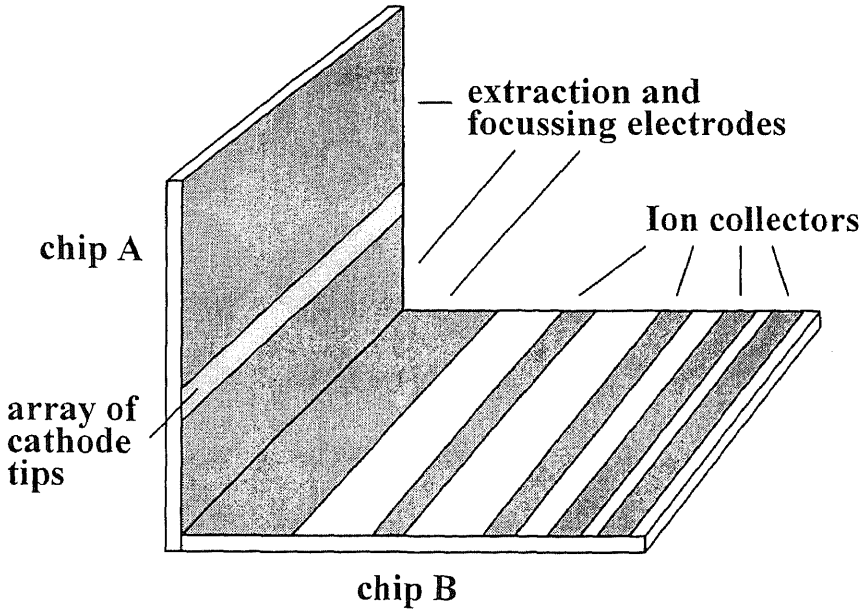

(a) Isometric view.

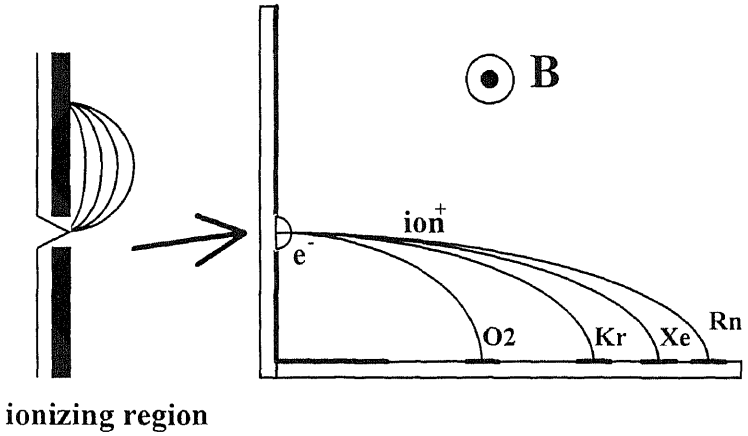

(b) Side view showing the electron and ion trajectories.

Figure 4.9 Schematic diagram of microengineered mass spectrometer.

4.4.2 Simulation of Microengineered Mass Spectrometer

In this section, several structures of this mass spectrometers devices were designed, simulated, and compared. The SIMION program is used to simulate the trajectories.

Figure 4.10 shows the device I which uses only one substrate. This device is a surface engineered planar structure. Its length is 1.5cm, width is 1cm. Due to the relatively small size of the active region compared to the overall size of the substrate, it was necessary to simulate the active region separately from the ion collection region of the device. Figure 4.10(a) shows the entire region while Figure 4.10(b) shows the active region. The ratio of the scale of these two figures is 10:1. Electrode A is an electron collector with 50V. B and C are both focal electrodes with -20V and -50V respectively. D1, D2, D3, and D4 are all 0V. Cathode tips on the substrate are grounded. The magnetic field is 3000 Gauss (directed out of the paper). Electrons are field emitted from cathode tips and collected by electrode A. Ions created in the active region are attracted by electrode B, focused by electrode C, and finally collected by one of the collectors D1, D2, D3, or D4.

Figure 4.11 shows the device II with two substrates. The vertical substrate (chip A) containing the cathode is 1cm by 1cm and the lateral substrate containing the anodes is 1.5cm by 1cm. Figure 4.11(a) shows the entire device II with ion trajectories. Figure 4.11(b) is expanded 10x to show the active region. The surface of the vertical substrate is biased at 50V, but the cathode tips array is grounded. Ion collectors D1, D2, D3, and D4 on the lateral substrate (chip B) are also maintained at near ground potential. The main advantage of device II is that the sensitivity was greatly increased due to its larger active

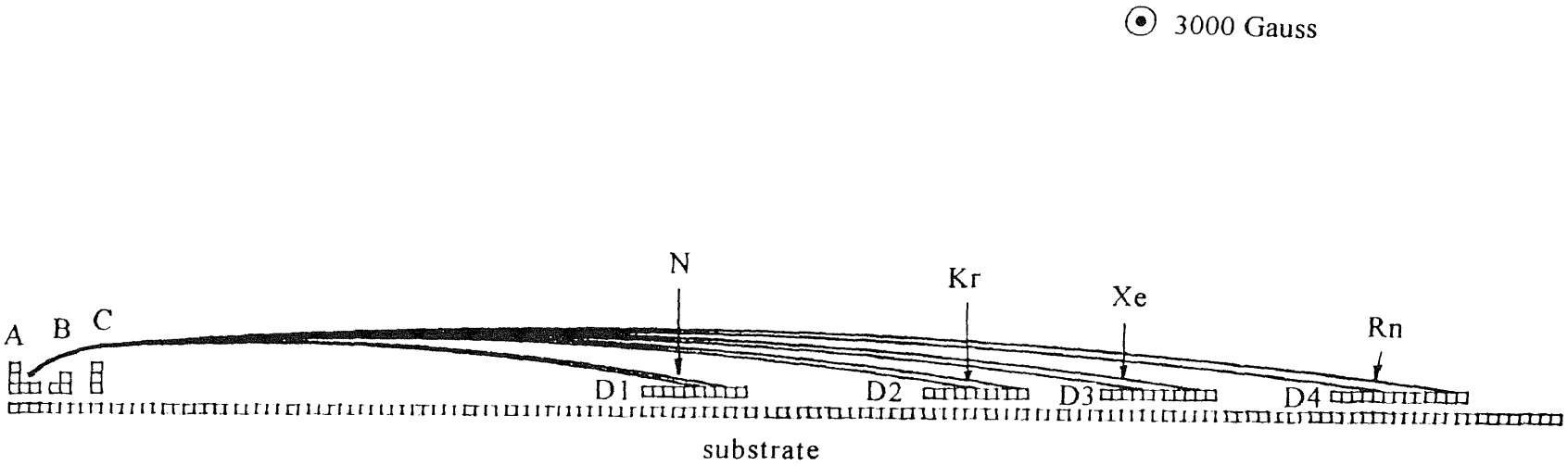

Figure 4.10 (a) Planar device I showing ion trajectories for nitrogen, krypton, xenon, and radon. Magnetic field is 3000 Gauss. A, B, and C electrodes are biased at 50V, -20V, and -50V respectively. D1, D2, D3, and D4 are all biased at0V. The scale unit is 0.1mm per square.

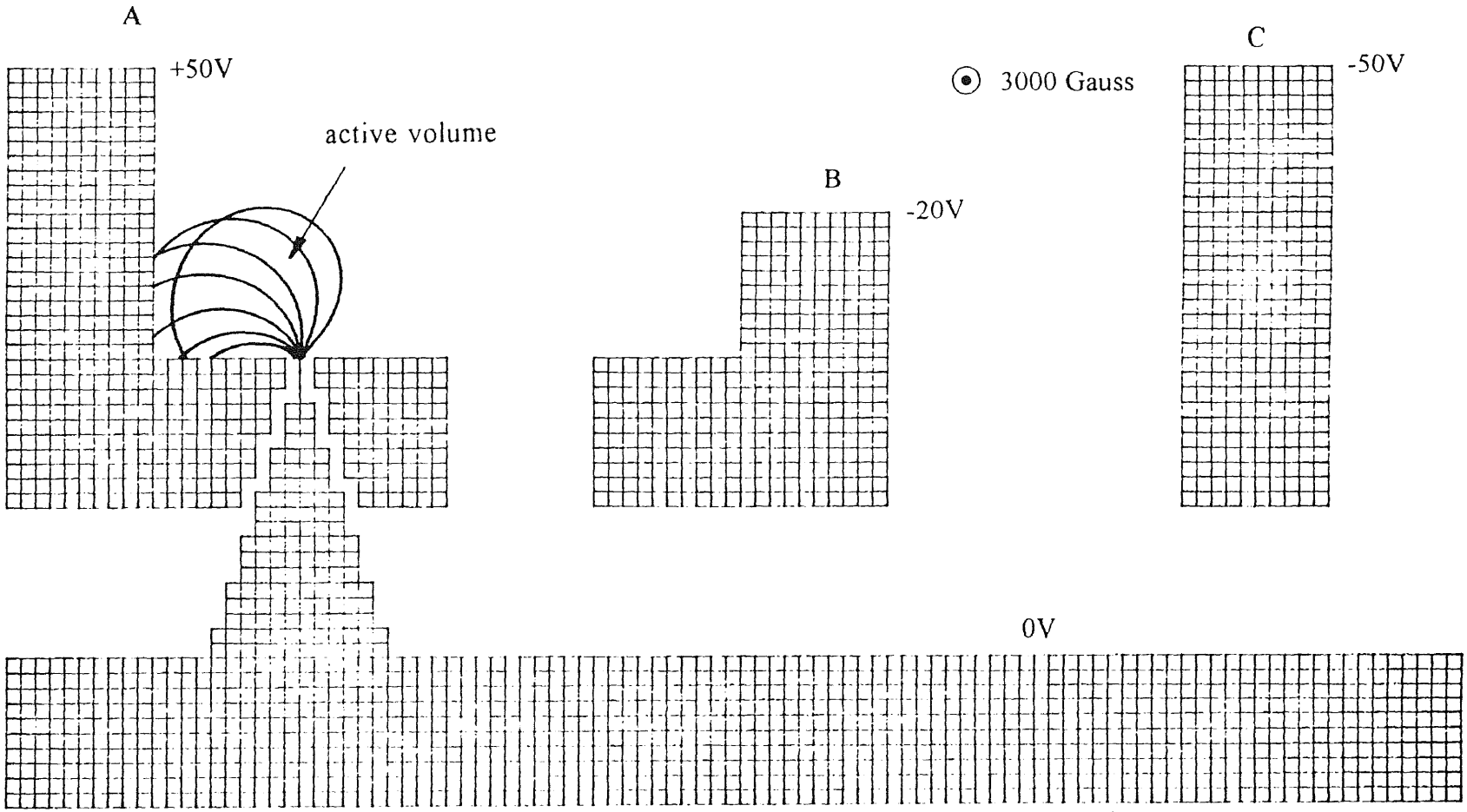

Figure 4.10 (b) Close in electron cathode region of device I with cathode tip showing trajectories of electrons and ions. The scale unit is 0.01mm per square.

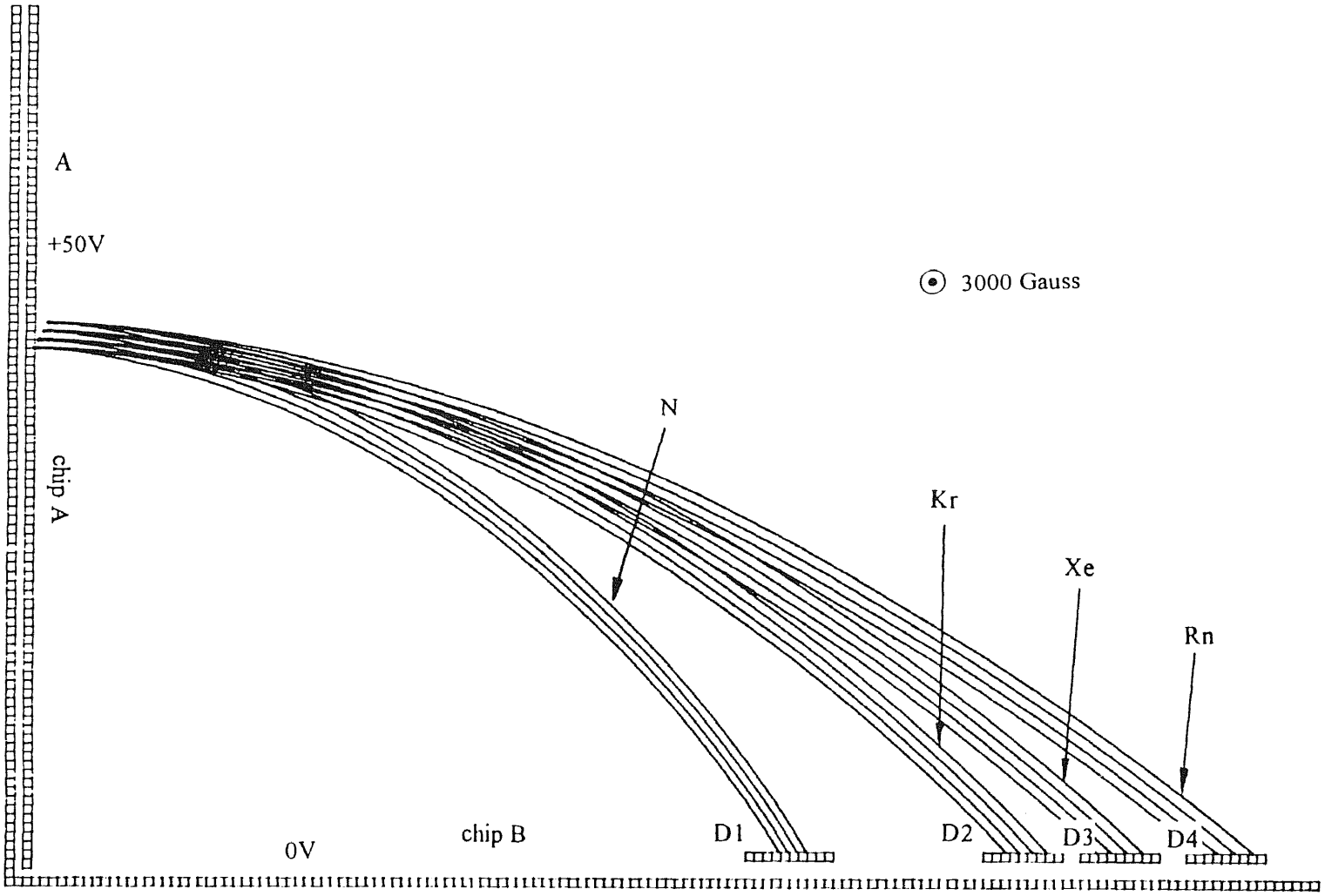

Figure 4.11 (a) Device II showing ion trajectories for nitrogen, krypton, xenon, and radon. Magnetic field is 3000 Gauss. A is biased at 50V. D1, D2, D3, and D4 are maintained at near 0V. Substrates are grounded. The scale unit is 0.1mm per square.

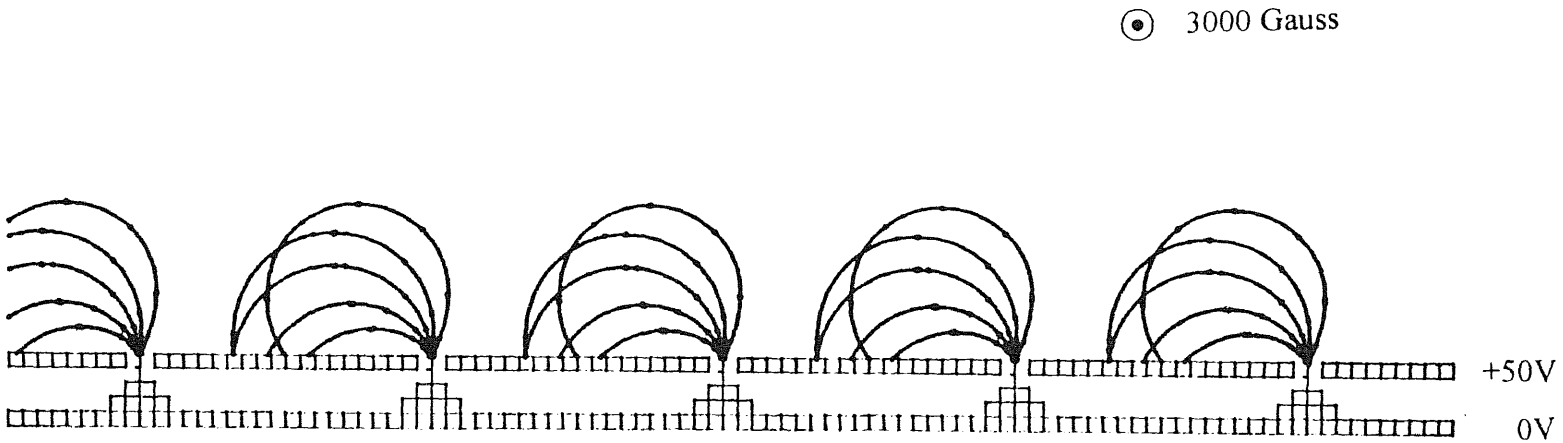

Figure 4.11 (b) Close in electron cathode region of device II with cathode tip array showing electron trajectories. The scale unit is 0.01mm per square.

region (between the initial point of the highest and lowest ion trajectories in figure 4.11(a)).

The sensitivity results from the ions created and detected (collected). An increased volume of the ionizing active region results in additional ionization and a resulting higher sensitivity. The ionizing active region is very close to the cathode tips. The ionizing volume is determined by the total number of tips. However, as the volume of the active region is increased beyond certain special limits, overlap of ion trajectories will occur. This means ions with different mass, for example, Xe^+ and Rn^+ cannot be separated and collected by adjacent collectors D3 and D4 respectively. A portion of Xe^+ will be unacceptably collected on radon collector D4 and a portion of Rn^+ will also be unacceptably collected on xenon collector D3. Figure 4.12 shows the simulation of the trajectory overlap problem. Trajectories of Xe^+ and Rn^+ are selected for illustration in this figure. Overlap will reduce resolution of this device. The trade-off should be made between sensitivity and resolution. Since many factors, for example, the uniformity of applied magnetic field, the sharpness of tips, the distance between neighboring tips, will effect a change in resolution, the calculation of resolution is very complicated. The computer simulation results provide trajectory information in which the magnetic field is assumed to be uniform. Trajectories for different gas species which do not overlap in the SIMION simulation plot are indicative of the desired performance.

After many simulations, it was found that if an electrode was added to the left side of chip B (figure 4.11(a)) with the same voltage as that on the surface of chip A (50V), the active region could be larger but without ion trajectories overlap. Figure 4.13 shows

the device III. The added electrode F acts like a focal electrode. The ion separation is much better than device II.

By comparing device I design, device II design, device III design, and many other structures which are not shown in this thesis, the optimized geometry of the microengineered mass spectrometer was determined to be device III. It can be seen from figure 4.13 that nitrogen, krypton, xenon and radon ions are adequately separated by device III. The active region of device III is the largest. It provides maximum sensitivity. The remainder of this thesis describes device III.

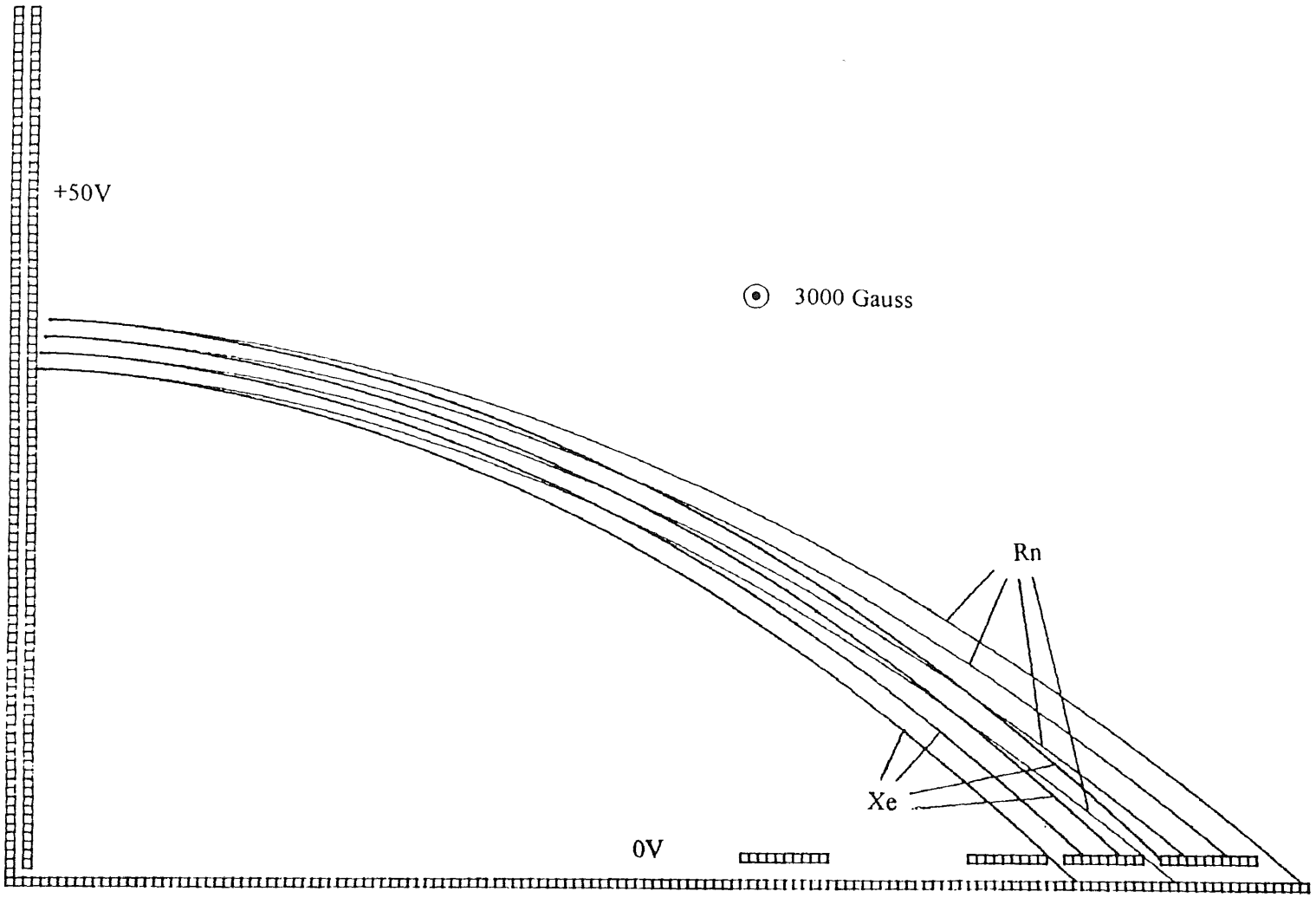

Figure 4.12 Xenon and radon ion trajectories overlap. Ion collectors are maintained at near 0V. The scale unit is 0.1mm per square.

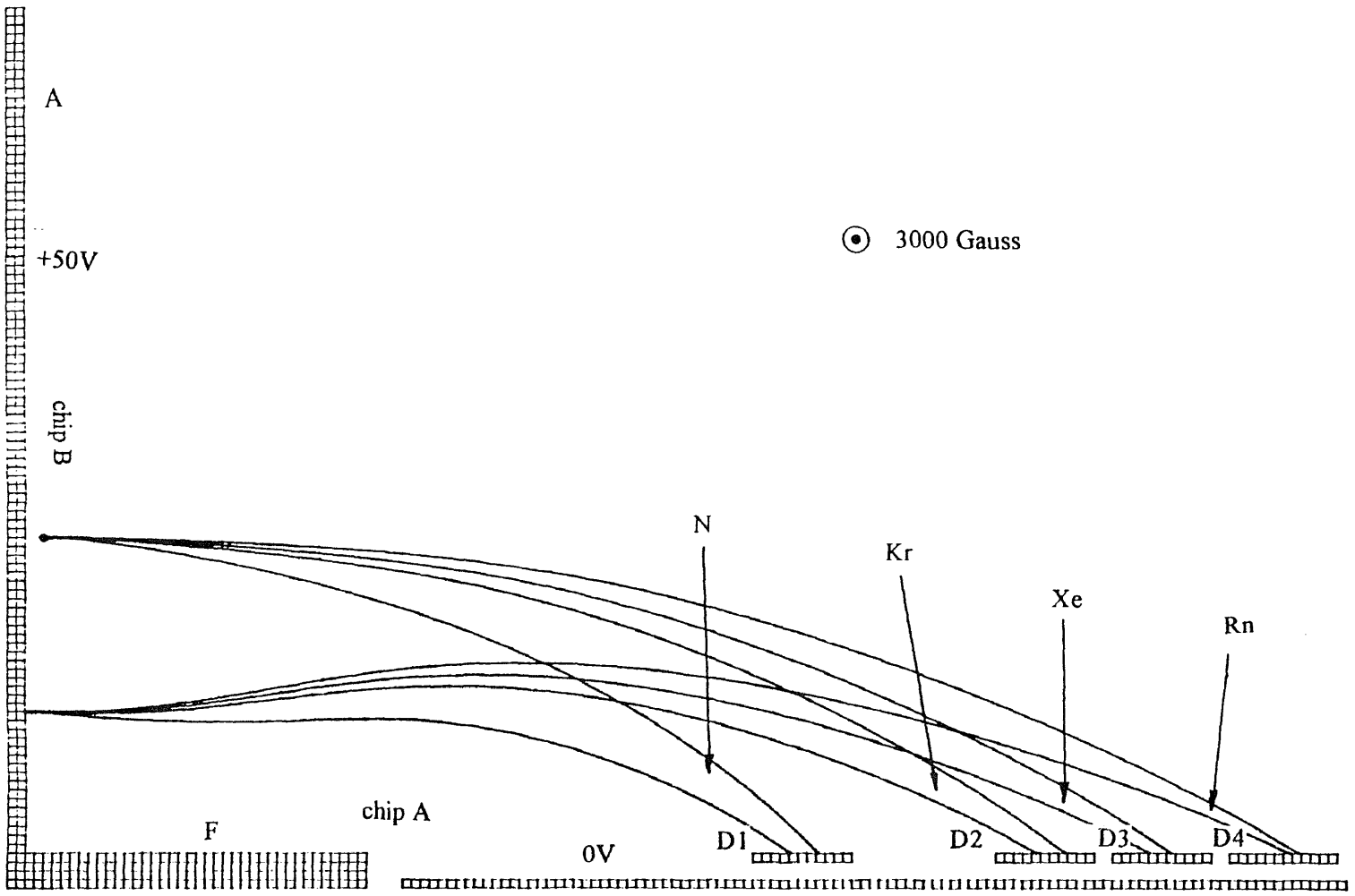

Figure 4.13 Device III showing ion trajectories for nitrogen, krypton, xenon, and radon. Magnetic field is 3000 Gauss. A and F are connected and biased at 50V. D1, D2, D3, and D4 are maintained at near 0V. Substrates are grounded. The scale unit is 0.1mm per square.

4.4.3 Cathode Design

The critical electrodes in the microengineered mass spectrometers are the cathode tips. The location of the cathode determines the active, ionizing region. The electrons emitted from tips must ionize molecules in and only in the active region. Any ionization activity outside the active region will generally cause dispersion. The electron trajectories are determined by applied electric and magnetic fields, field emission tip shape and distance between individual tips and the gate (electron extraction electrode). Figure 4.14 shows the near-field trajectories of electrons emitted from the cathode tip array. In the design, trial values for the voltage of electrodes and the magnetic field were selected. Then ion trajectories were simulated by the aid of the SIMION program. Basically, the design requires that the maximum volume for the active, ionizing region be selected which will permit isotope separation. This is done by varying the starting point coordinates of ions ($x \rightarrow x+\Delta x$, $y \rightarrow y+\Delta y$) until the overlap of some ions with different mass occurs. In the optimized design shown in Figure 4.13, the variations in the ion starting point coordinates, Δx and Δy, are 0.2mm and 2mm, respectively. The product of $w \times \Delta x \times \Delta y$ is defined as the volume of active region, where w is the width of the substrate (w=1cm in this design). The location of the cathode tips array must be within the area $w \times \Delta y$ so that all emitted electrons can only travel in the active region. Figure 4.15 shows a view of the cathode-tip array (chip A) and the active region (enclosed by dotted lines).

Simulation results also show that the electron trajectories of most electrons are approximately a semicircle (Figure 4.14(b)). The maximum height of the trajectories is less than 200μ. Since no electron travels beyond this height, there are no ions created. Therefore the design requirement $\Delta y \leq 0.2$mm is satisfied.

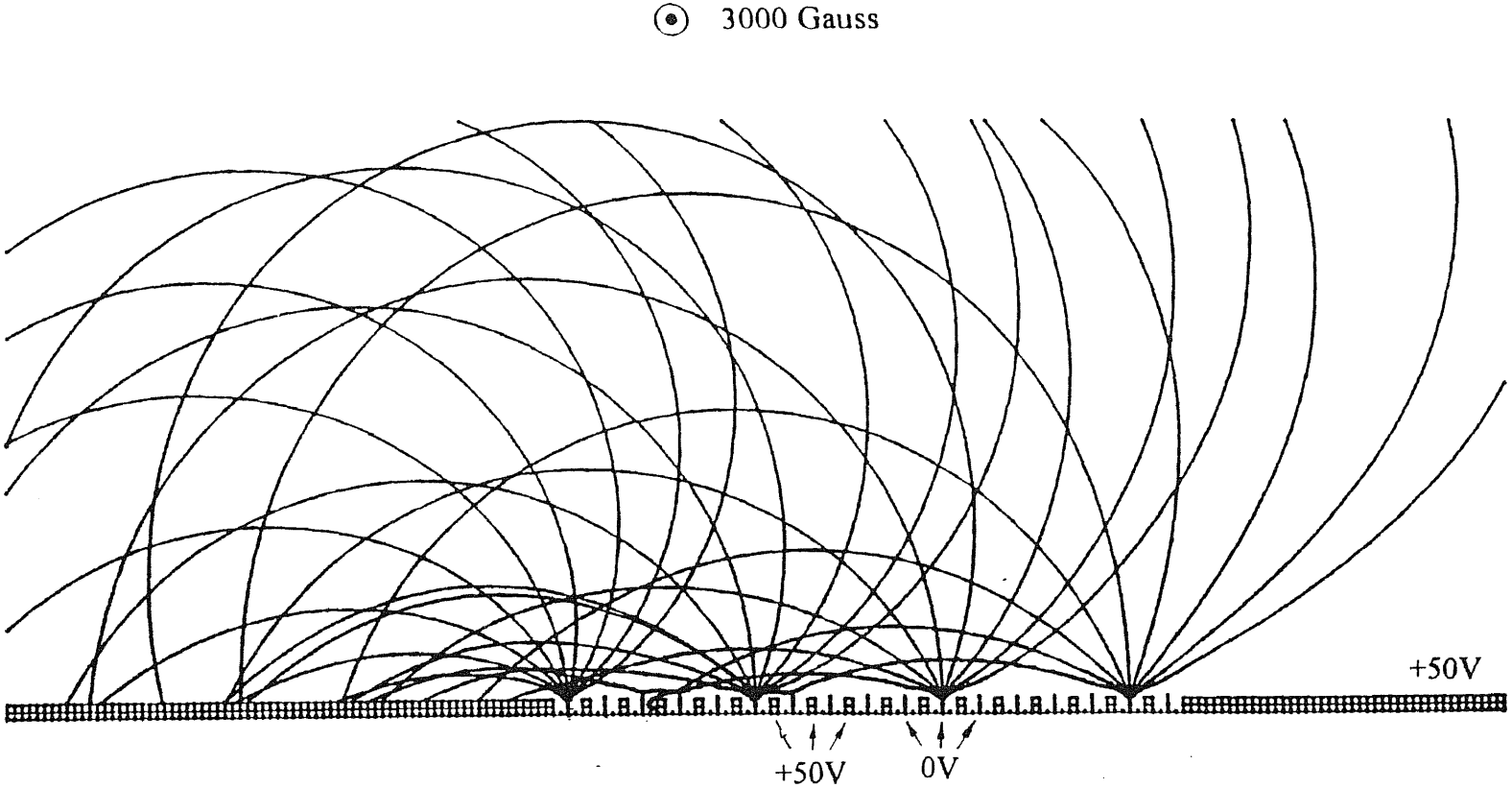

Figure 4.14 (a) Trajectories of field emitted electrons. The scale unit is 5μm per square.

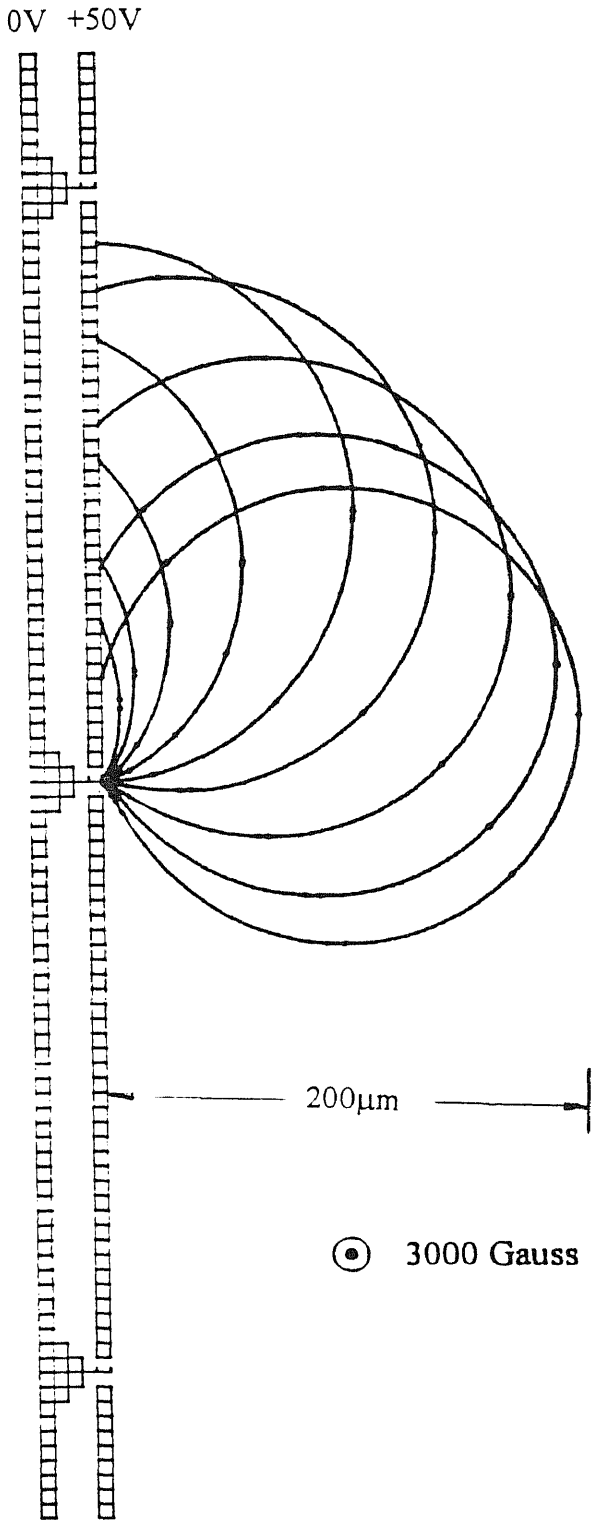

Figure 4.14 (b) Electrons emitted from one of the tips. The scale unit is 5μm per square.

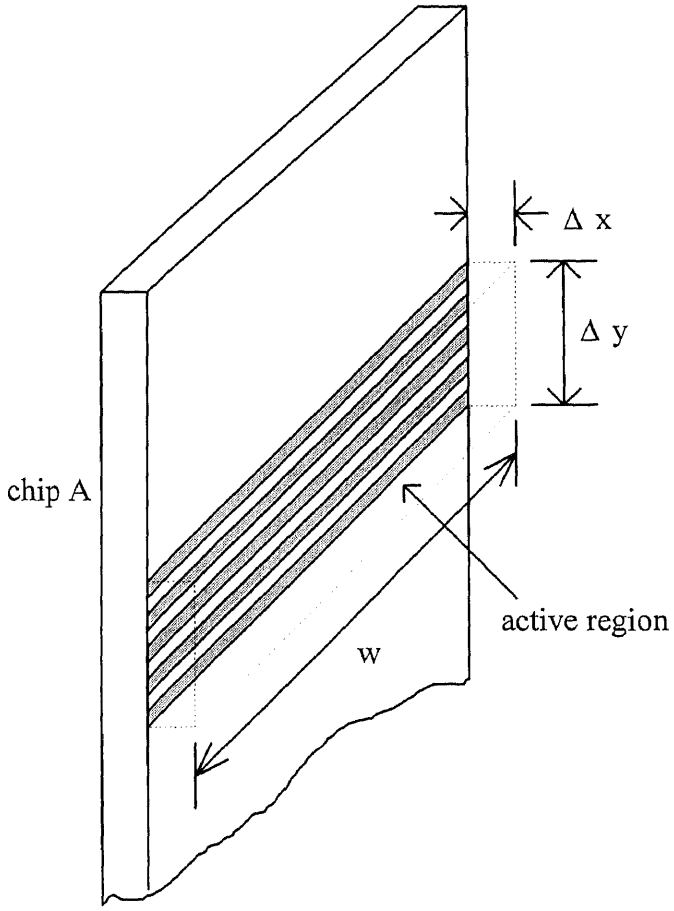

Figure 4.15 A portion of chip A showing the active region (enclosed by dotted lines).

Due to the very small size of the active region compared to the overall device dimensions, it is impossible to observe electron paths at the cathode tips when simulating ion trajectories. The limited resolution for the SIMION simulation does not permit simultaneous plots of electron and ion trajectories within the same field. Zooming techniques are available but are not used in this design. The maximum matrix size for

SIMION version 4.0 is 16,000 array points. In the ion trajectory simulation the tips array was simply treated as a conducting plane of 50V potential (refer to Figure 4.13, electrode A). In the real device, the tip inside the small gate opening is grounded and will modify the electrostatic field and hence the ion trajectory slightly. The contour of the electrostatic field near a gate opening is shown in Figure 4.16. Ions created near the gate opening might be dispersed, caused by the curvature of electric contours (Figure 4.16(a)). To reduce ion dispersion, the cathode tip arrays were divided into ten smaller arrays. Each smaller array contained three lines of tips. The distance between adjacent smaller arrays is about 200μ. This is larger than the diameter of the trajectory of most electrons. Because there are no gate openings within the 200μ-region where ions are created, the electric field is uniform and overall ion dispersion is reduced (Figure (4.16(b)). In the region very near the tip, electrons do not yet have enough kinetic energy to strip off an electron from a molecule (ionize) upon impact. This cathode design reduces the dispersion of ions at the ion collector.

The cathode used in the device III is a lateral geometry. It has a simple structure compared to the vertical geometry. But the current density of the lateral geometry is lower than that of the vertical geometry. Since there is a large number of tips on the cathode of device III (total number of tips is 37.5k). This provides enough electron cathode current for ionization.

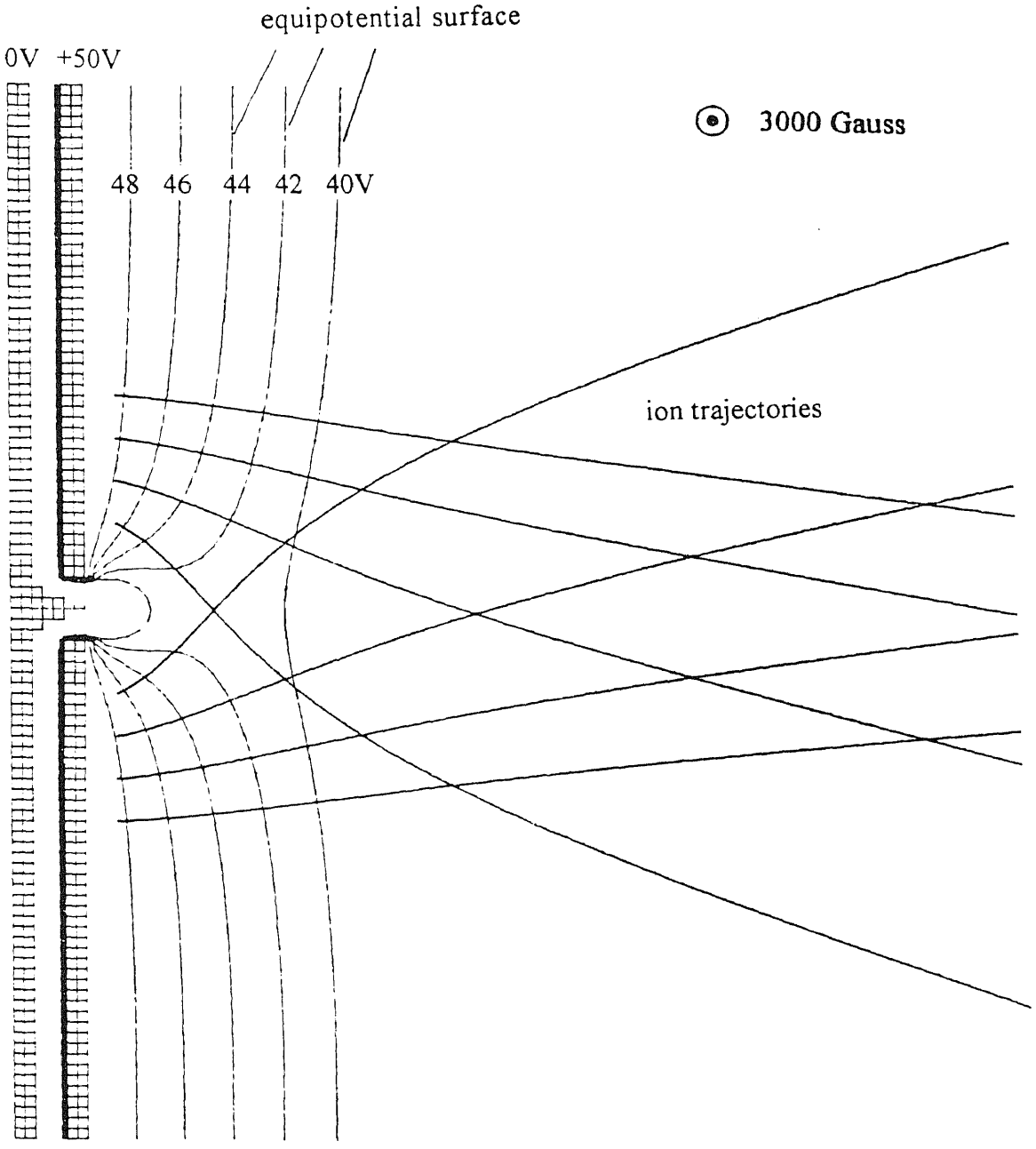

Figure 4.16 (a) Illustration of dispersed ions trajectories. Ions originating near the cathode have higher dispersion. The scale unit is 1μm per square.

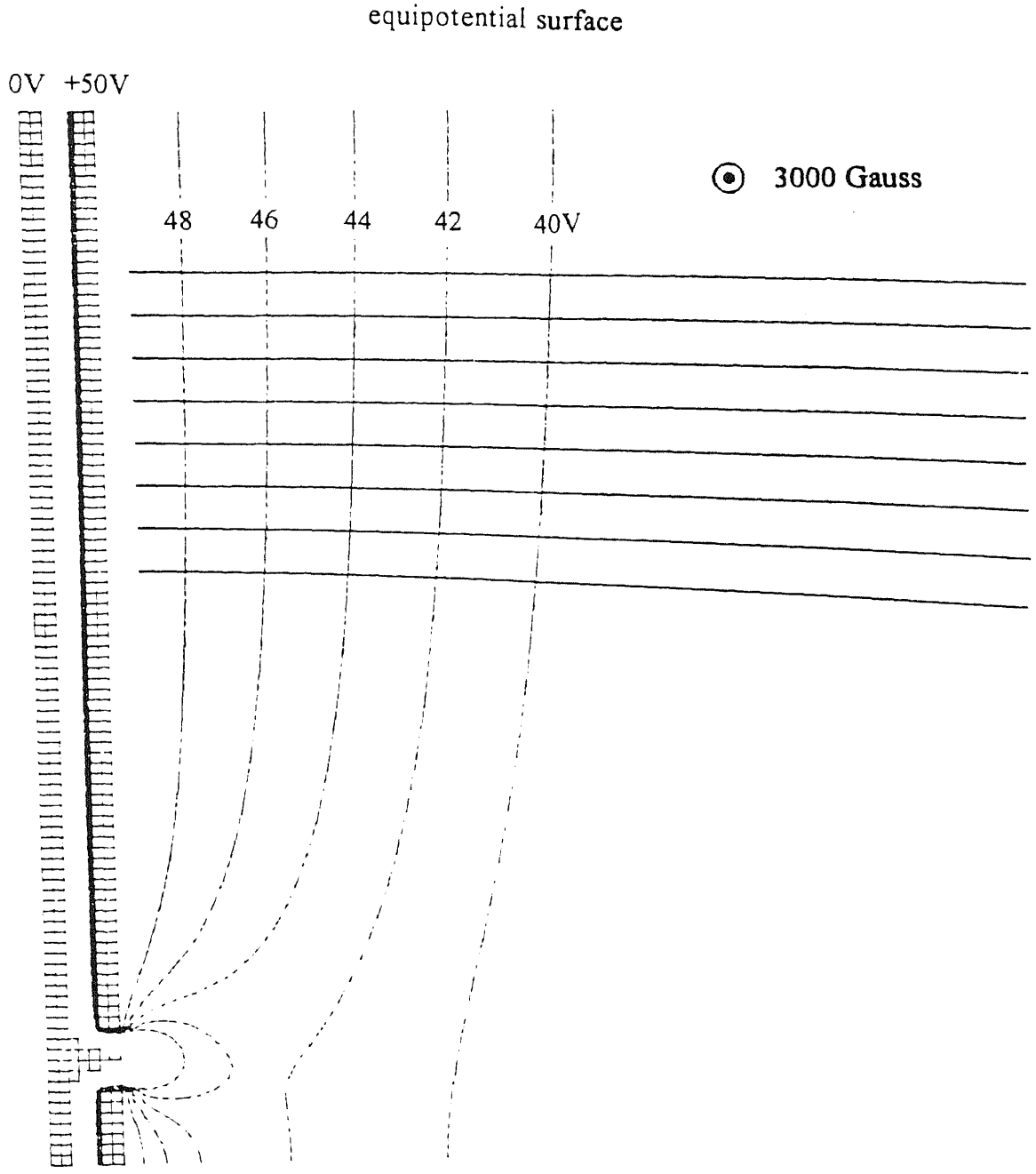

Figure 4.16 (b) Selected ion trajectories (m=222 amu) illustrating minimal local dispersion effect due to proximity to high E-field. Ions originating far from the cathode tip have no dispersion. The scale unit is 1μm per square.

CHAPTER 5

DEVICE PROCESSING AND INTEGRATION

In this chapter the fabrication processing of the microengineered mass spectrometer and vacuum sensor devices is detailed. The fabrication processing steps of these two devices are compatible.

5.1 Fabrication of the Microengineered Mass Spectrometer Device

This device consists of two chips. Chip A contains the electron cathode tip array and the electron collector electrodes. Chip B contains the coplanar ion collectors (see Figure 4.7).

5.1.1 Fabrication of Chip A with Cathode Tip Array

A critical component of the microengineered mass spectrometer device is the cathode tip array. The high ion-yield requires as high an electron current from the cathode as possible. It has been reported that the electron emission efficiency of an array of cone-shaped tips array is higher than that of wedge-shaped tips of the same total area [29-32]. In this microengineered mass spectrometer device, several arrays of a large number of tips are chosen as the cathodes. It is important that field emitters be very sharp since the electric field scales with sharpness and electron emission is strongly dependent on the electric field. Sharp emitters also make it possible for the device to operate at low voltage. The emitter damage by ion bombardment can be reduced at low operating voltage due to kinetic energy reduction, and therefore the emitter lifetime can be extended. In addition to a sharp emitter, an optimum field emission device requires many

other features such as a low work function emitter which helps to enhance electron emission [8], a high melting point emitter which helps to withstand high temperatures caused by resistive heating [9], and a small gate opening for a gated emitter structure which helps to increase the electric field [33]. Also, the dielectric film between electrodes should have high dielectric strength and the film should be thick enough in order to maintain the necessary operating voltage without breakdown or significant leakage. Finally, a tall emitter helps to enhance electron emission [34].

Sharp field emitters can be produced in many ways [35-36]. The emitters in this device are fabricated by using an oxidation method for sharpening [37-40]. During oxidation, the preliminary structure is sharpened due to the slower rate of surface reaction at the tip than at the sidewall. The faster surface reaction rate at the sidewall results in more silicon being consumed than at the tip and consequently the emitter is sharpened [41].

There are three mask levels needed for processing chip A. Figure 5.1 shows the layout of the three mask levels. The overall processing scheme used in fabricating the tip array is the standard oxidation sharpening method [42]. The starting material is an n-type, (100) silicon wafer. The major fabrication steps are shown in Figure 5.2 and are described as follows:

(a) Oxidize a n-type (100) silicon wafer at 1050°C for 1 hour in oxygen to grow a 2000Å~3000Å thermal oxide layer followed by spinning photoresist on the surface.

(b) Define silicon oxide pattern. Use lithography to transfer the pattern of mask 1 onto the resist. The pattern consists of 2 μm and 4μm diameter discs. Transfer photoresist pattern to the silicon oxide by wet etching.

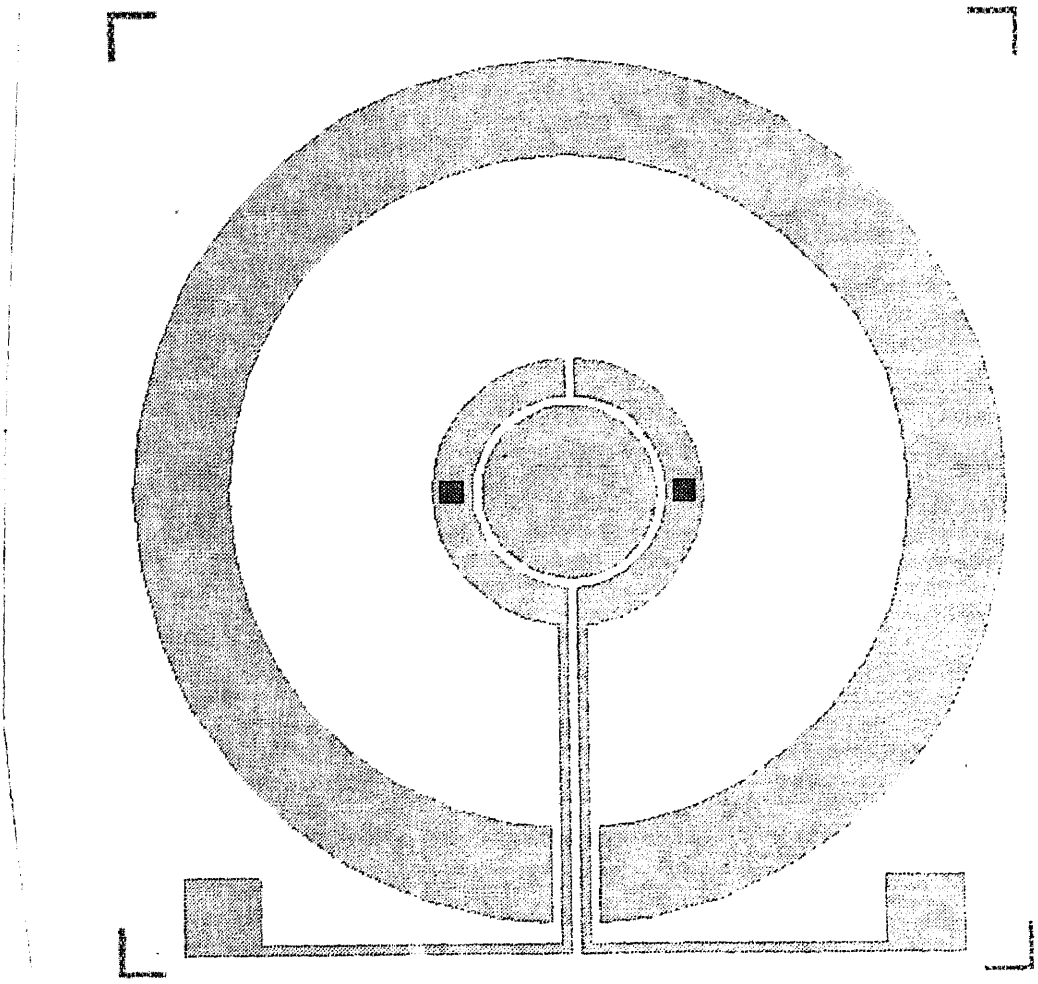

Figure 5.1 Mask layout for microengineered pressure sensor device

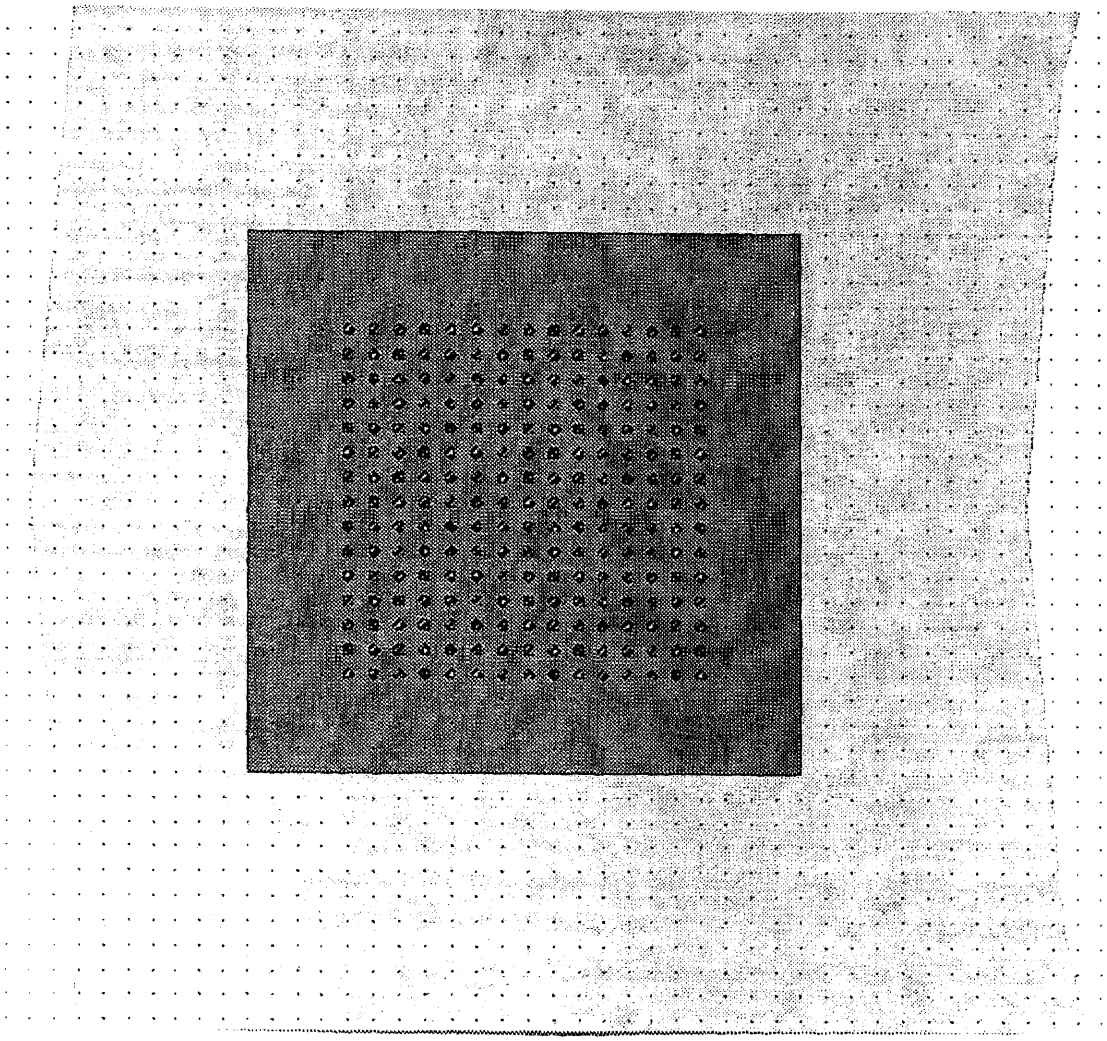

Figure 5.1 (Continued) Expanded view of cathode area.

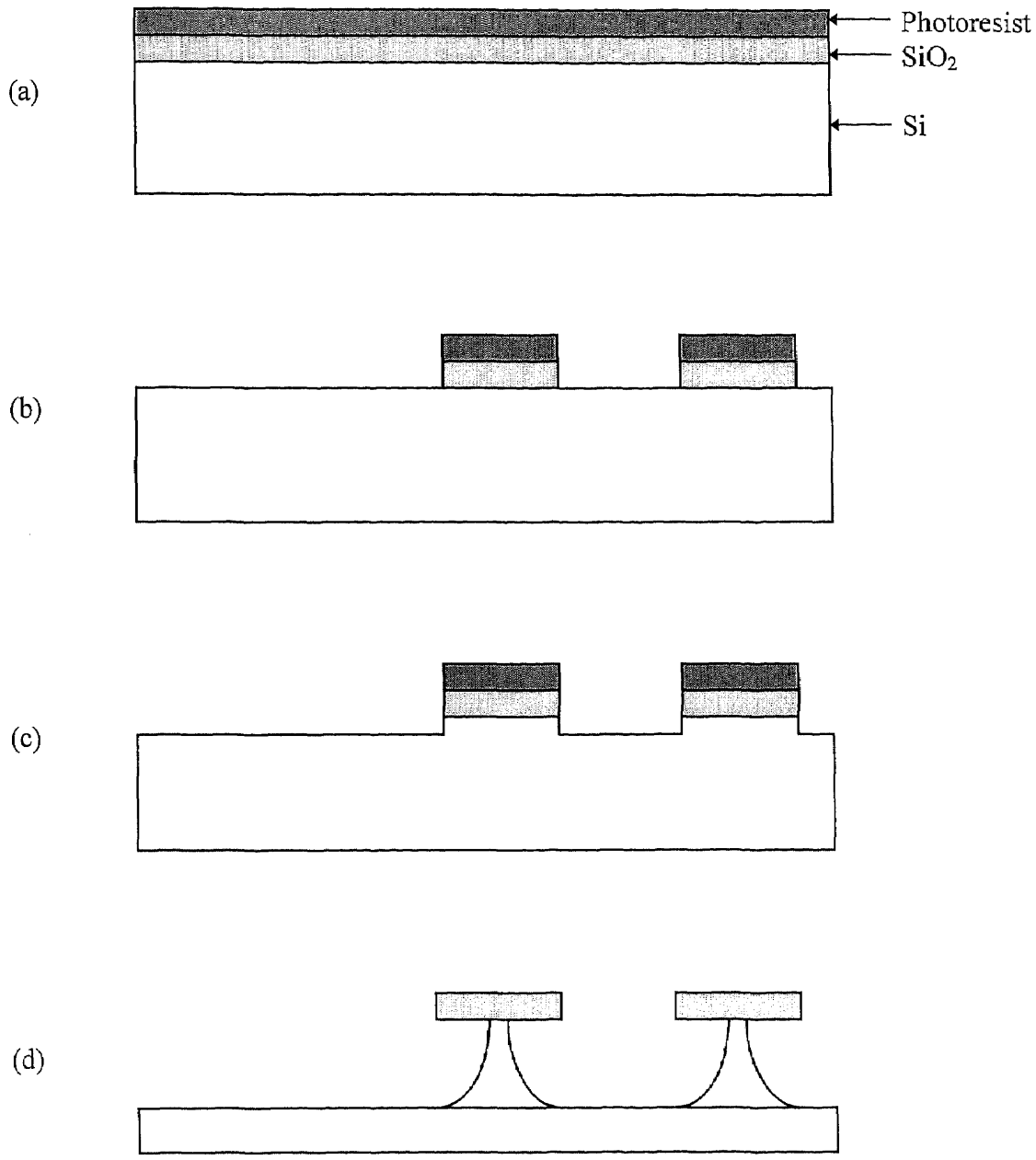

Figure 5.2 Fabrication steps of the gated silicon tip array.

(e)

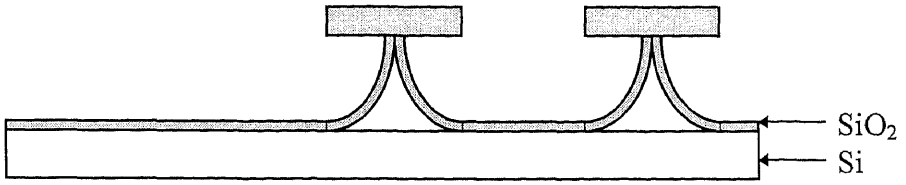

(f)

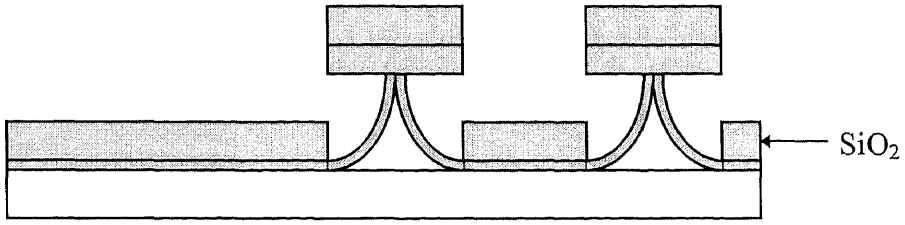

(g)

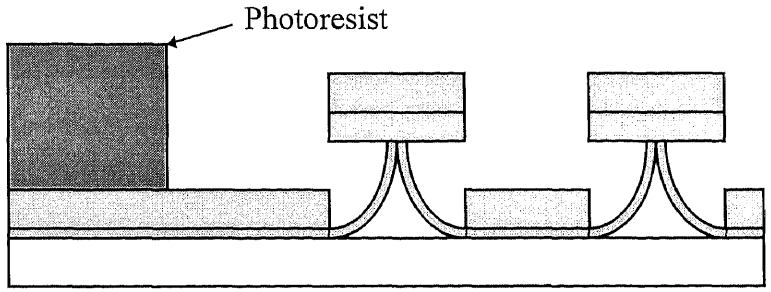

(h)

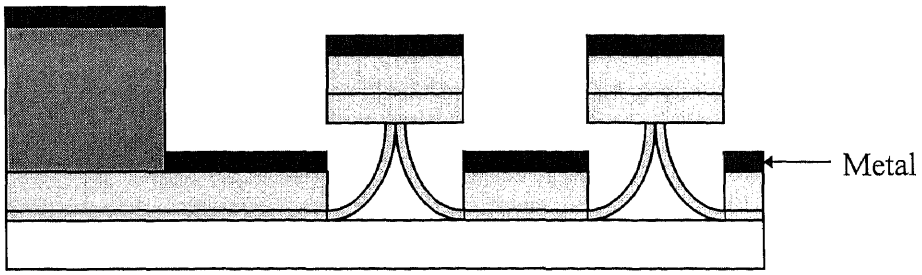

Figure 5.2 (Continued)

(i)

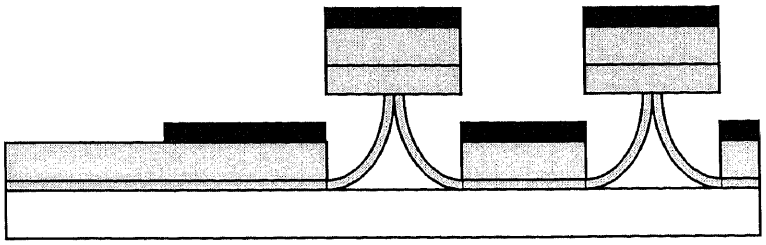

(j)

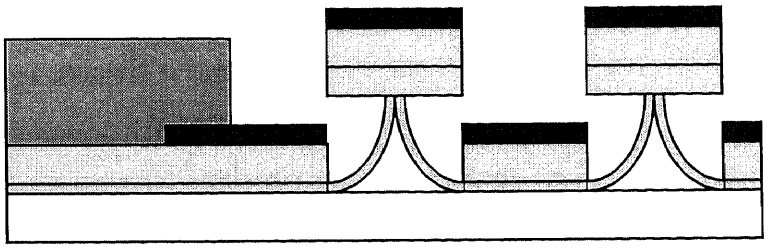

(k)

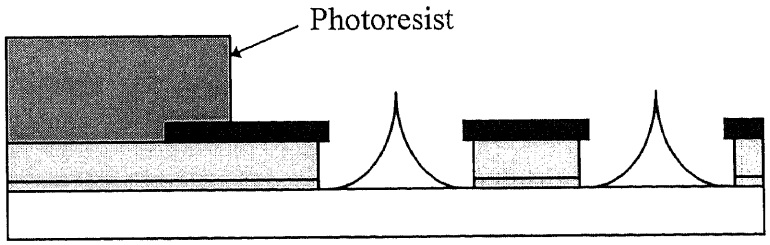

(l)

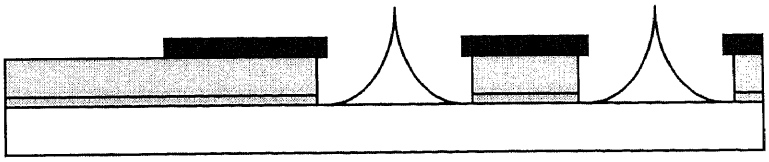

Figure 5.2 (Continued)

(c) Use the patterned silicon oxide as a mask to etch down the silicon by anisotropic RIE. The RIE is performed by SF_6 and Freon 115 gases using a 50 sccm (standard cm^3/min.) flow rate, 150 mTorr gas pressure, and a 400 W of RF power. 5000Å of silicon is etched to form a straight wall structure. This etched silicon wall is used to obtain needlike tips during a later oxidation srep.

(d) Remove the photoresist and wet etch the silicon under the silicon mask. The solution consists of 2% HF, 8% CH_3COOH, and 90% HNO_3 (vol%). It is an isotropic silicon etchant with the oxide etch rate only 0.01 times the silicon etch rate. The etching process is stopped when the diameter of the silicon disc which supports the silicon oxide mask is decreased to around 1000-2000 Å. This is done by controlling the etch time. The typical etching time is 3~5 minutes.

(e) Dry oxidize the wafer at 950°C for 14 hours. This step may be repeated a few times to obtain very sharp tips.

(f) Deposit 8000Å of oxide by LPCVD. This oxide layer serves as the dielectric layer between the gate and the silicon tips.

(g) Spin a thick photoresist layer (6~8μm) and apply mask 2 to define the metal gate pattern. This thick photoresist layer will be used for metal lift-off in the following steps.

(h) Deposit gate metals by using electron beam deposition. The gate metals are self-aligned to the silicon mask during the deposition. The gate metals are 500Å titanium and 2000Å palladium. The titanium layer between the oxide and the palladium is for increasing adhesion between the oxide and the metal.

(i) Lift-off gate metals by removing the thick photoresist underneath the metal layers.

(j) Spin photoresist and expose through mask 3 to define windows which are opened in order to remove the silicon oxide mask on top of the tips. This step is necessary for preventing lateral etch of the dielectric layer underneath the metal, that could cause an electrical short between the tips and the gate.

(k) Remove silicon oxide mask by wet etching. The solution is 7:1 buffered HF. The etching time should be less than 2 minutes. Ultrasonic agitation may be employed to reduced the etch time. This final oxide stripping in buffered HF is used not only to remove the oxide, but to passivate the silicon tips against further oxidation [43].

(l) Remove the photoresist. The gated tip array is formed.

The SEM micrographs in Figure 5.3 shows the tip formation progress after certain process steps. In this process, the shape of emitter tips can be controlled by anisotropic RIE conditions. Figure 5.3(a) shows the SEM micrograph after RIE (step c). Since the RIE is not a perfect anisotropic etch process, there is some lateral etch under the silicon oxide masks. This will reduce the aspect ratio of the tips. This RIE step is necessary for obtaining more needlike tips during a later oxidation step. Figure 5.3(b) shows the SEM micrograph after isotropic wet etch (step d). We can see the diameter of silicon pillar which supports the silicon oxide mask is about 2000 Å. Figure 5.3(c) is a SEM micrograph taken after 14 hours dry oxidation at 950°C (step e). The bright region in the center of the micrograph indicates that the silicon tip is covered by oxide. The diameter of the pillar doubles due to oxidation. The emitter height can be controlled by anisotropic RIE time. The completed emitter tip array is shown in Figure 5.3(d). The complete picture of Chip A is shown in Figure 5.4. The rectangular area on the chip is the field

emission tip array. An ion focal electrode surrounds the tip array. Below the focal electrode there are some field emission test cells.

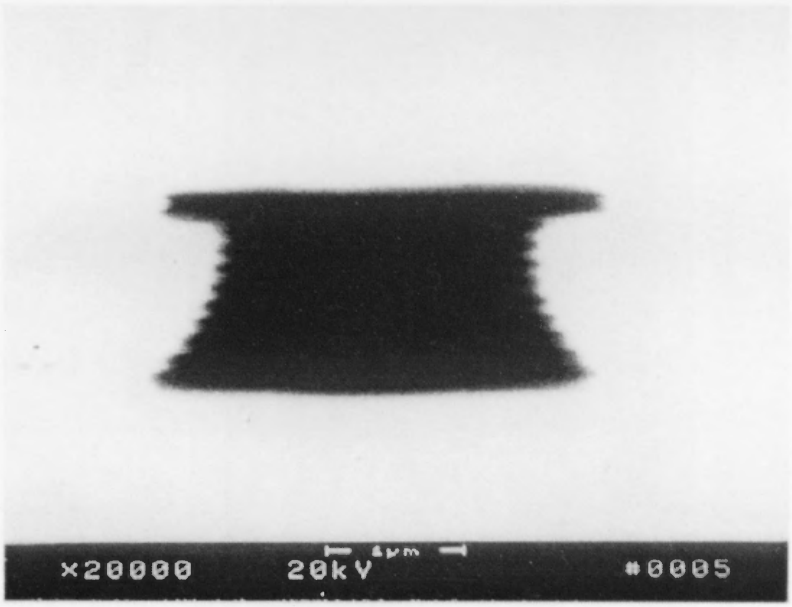

(a) After RIE (step c)

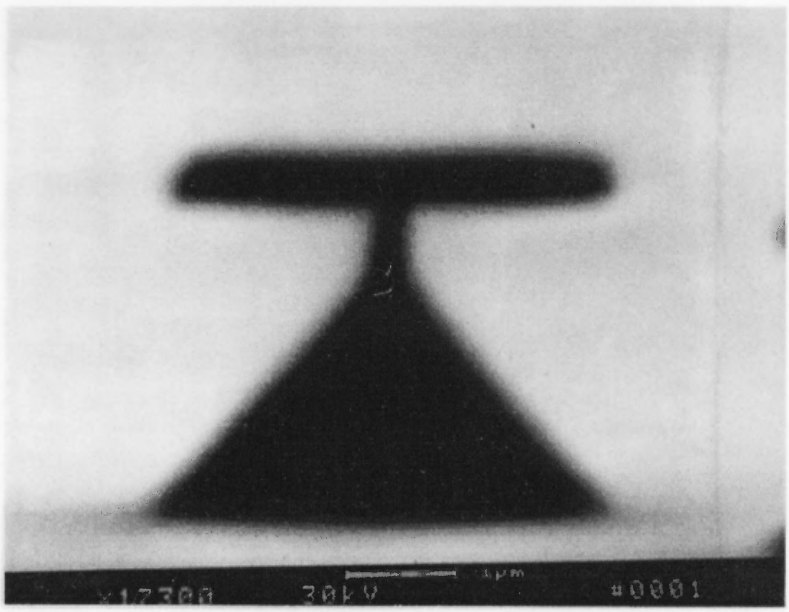

(b) After isotropic wet etch (step d)

Figure 5.3 SEM photographs show tip array formation progress.

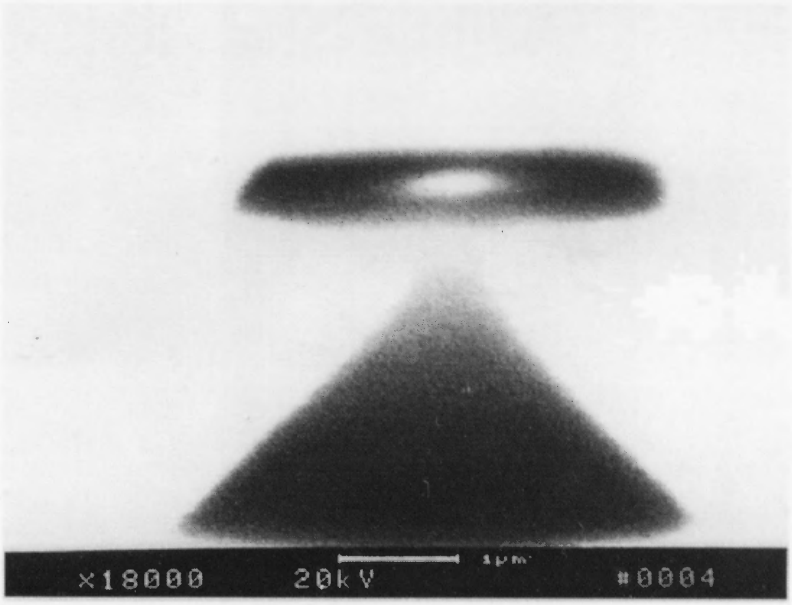

(c) After oxidation sharpening (step e)

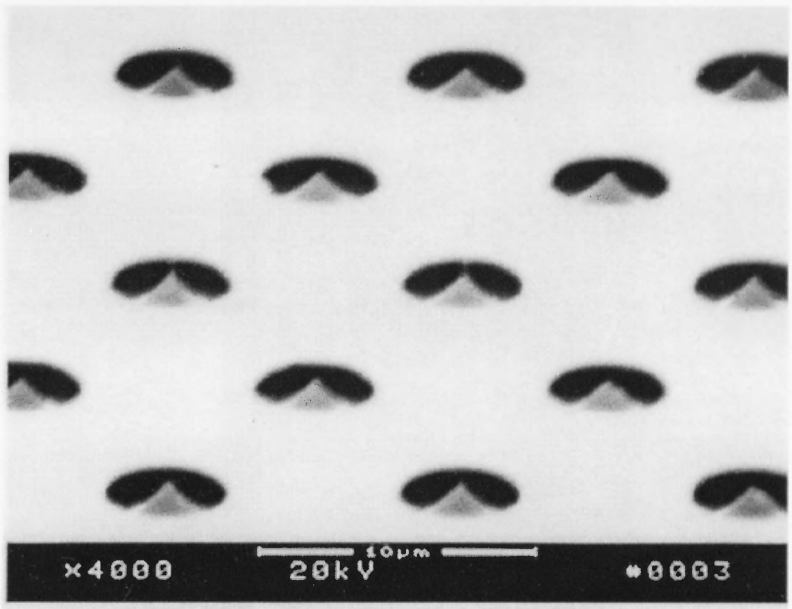

(d) Completed tip array

Figure 5.3 (Continued)

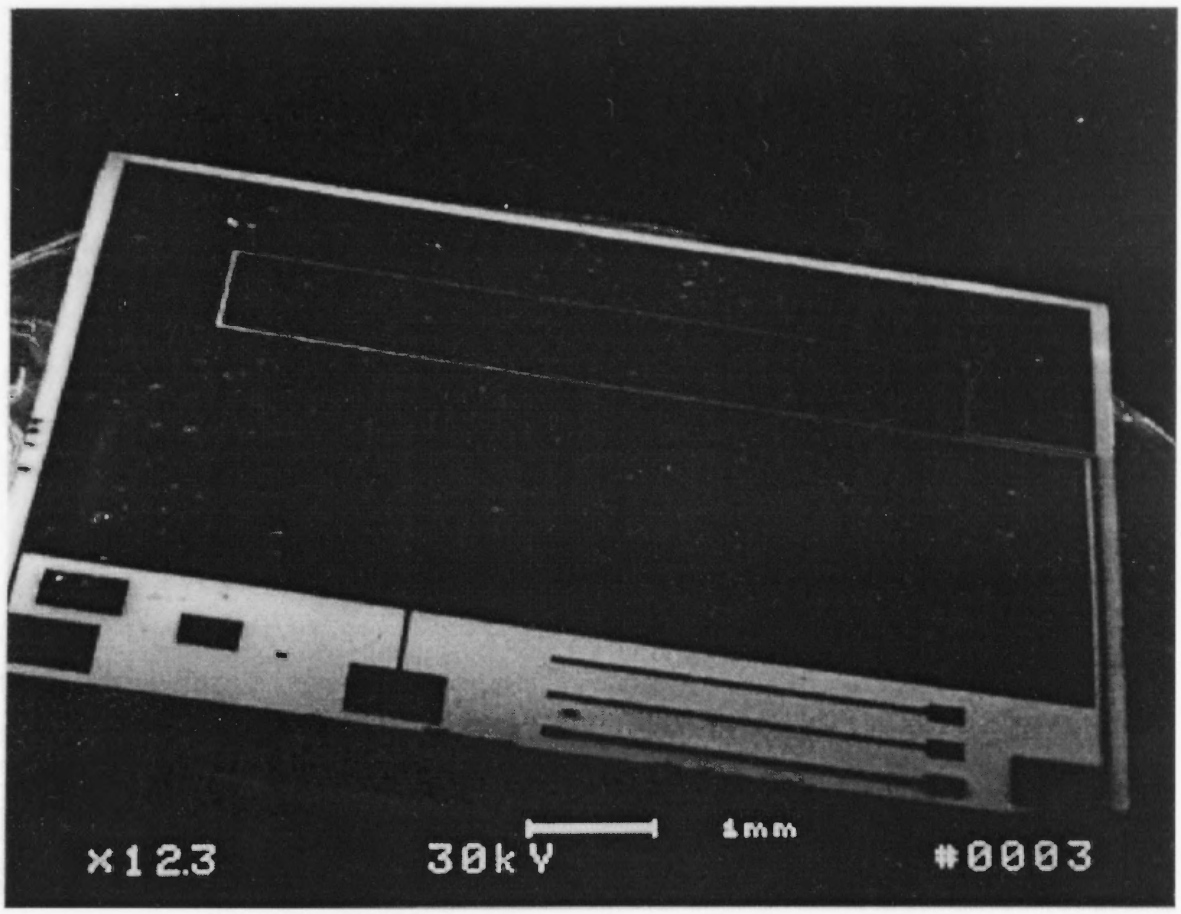

Figure 5.4 A complete picture of Chip A.

5.1.2 Fabrication of Ion Collector

Chip B contains ion collectors. Fabrication of chip B needs one mask level. The major fabrication steps are shown in Figure 5.5 and are described as follows:

(a) Oxidize a silicon wafer to grow an oxide layer (4000Å). This layer is used as an insulating layer between the substrate and the ion collectors.

(b) Deposit (sputter) an aluminum layer (5000Å).

(c) Spin photoresist on the aluminum surface and use lithography to transfer the electrode pattern into photoresist.

(d) Etch aluminum to form the electrode and remove photoresist. The solution is a standard aluminum etchant. The temperature is 40°C.

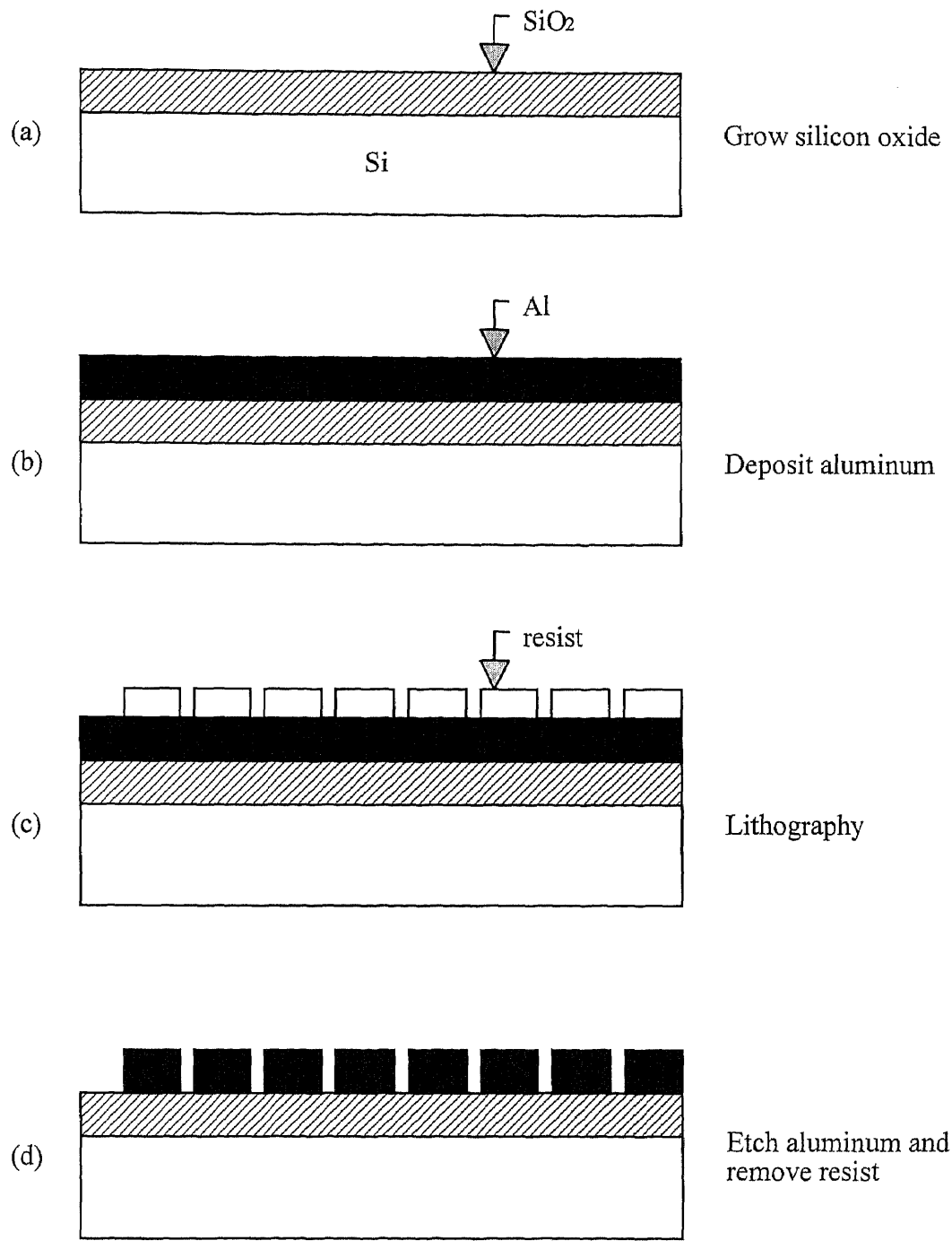

Figure 5.5 The major fabrication steps of coplanar ion collector

5.1.3 Package Assembly

Chip A (contains the arrays of cathode tips) and chip B (ion collectors) are connected at a 90° angle as shown in Figure 5.6. An L-shaped metal preform (aluminum, copper, etc.) can be used as the base for the two chips. The chip A and B are bonded to the surface of the bent metal. Then the assembly is mounted into a dual in-line DIP package with an internal ground plane.

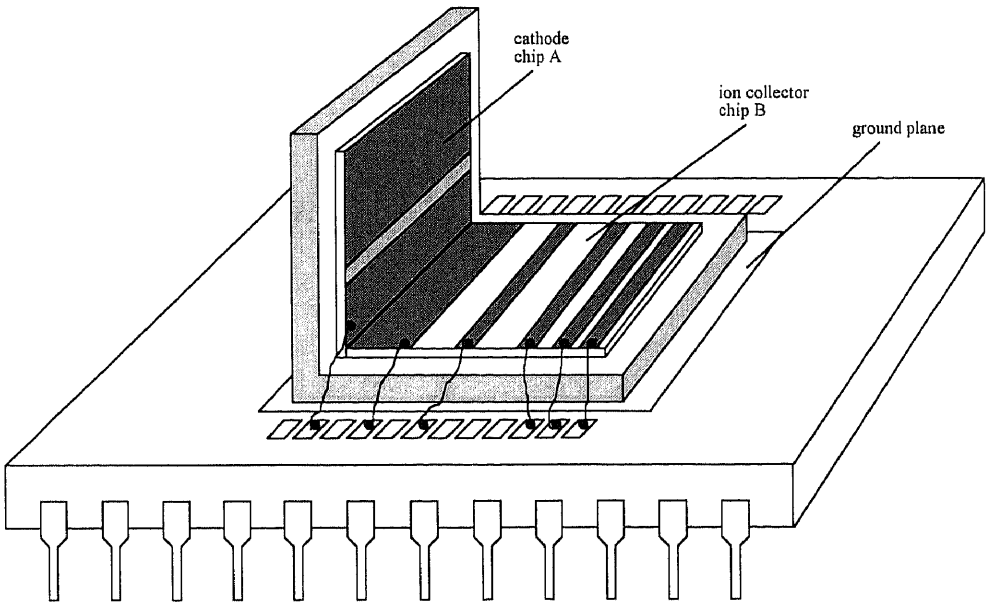

Figure 5.6 Assembled device in a 24-pin DIP package with ground plane

5.2 Fabrication of Microengineered Pressure Sensor

The processing steps for fabricating the microengineered pressure sensor are similar to thoes of the microengineered mass spectrometer described in the previous section. This sensor is a monolithic device. There are three mask levels needed for processing. Figure 5.7 shows the layout of the three mask levels.

The chip is mounted into a dual in-line DIP package with an internal ground plane (Figure 5.8). The ion collector on the center area of the chip is connected to the package via a stiff wire that is bent above the chip. Figure 5.9 shows an SEM micrograph of the completed chip.

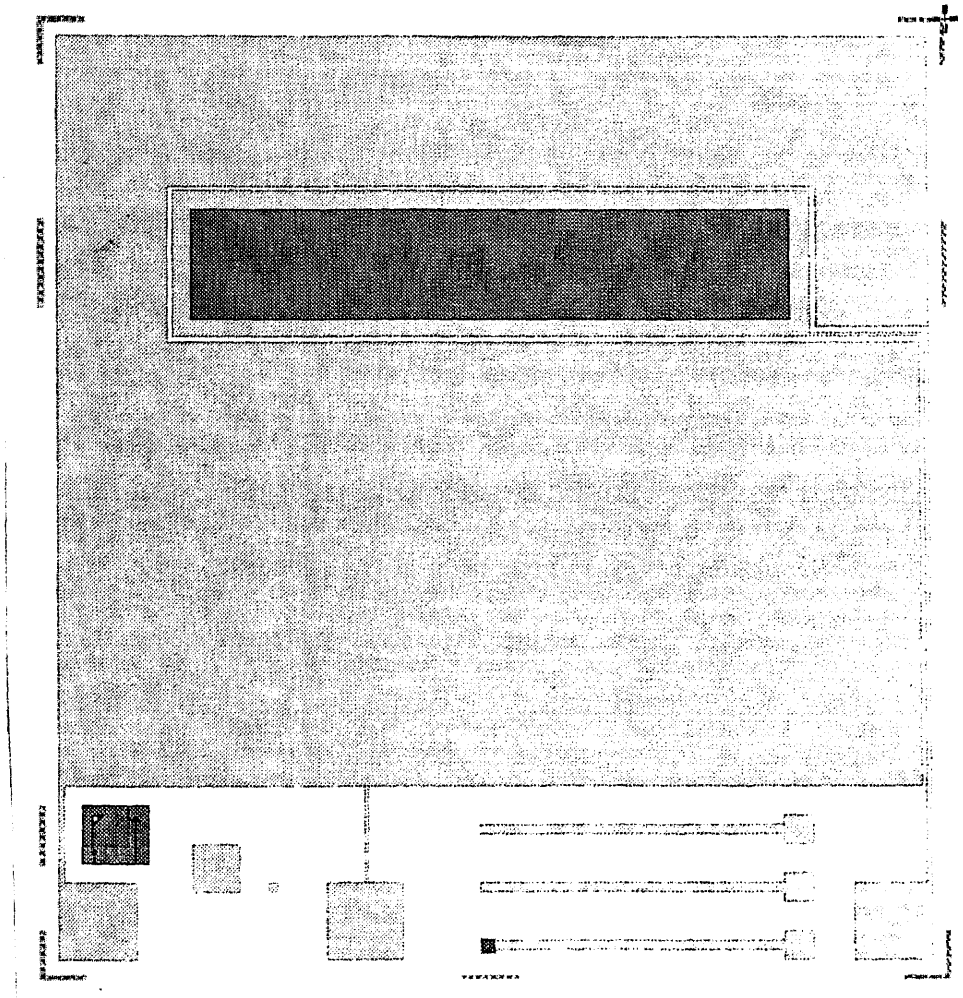

Figure 5.7 Mask layout for microengineered mass spectrometer

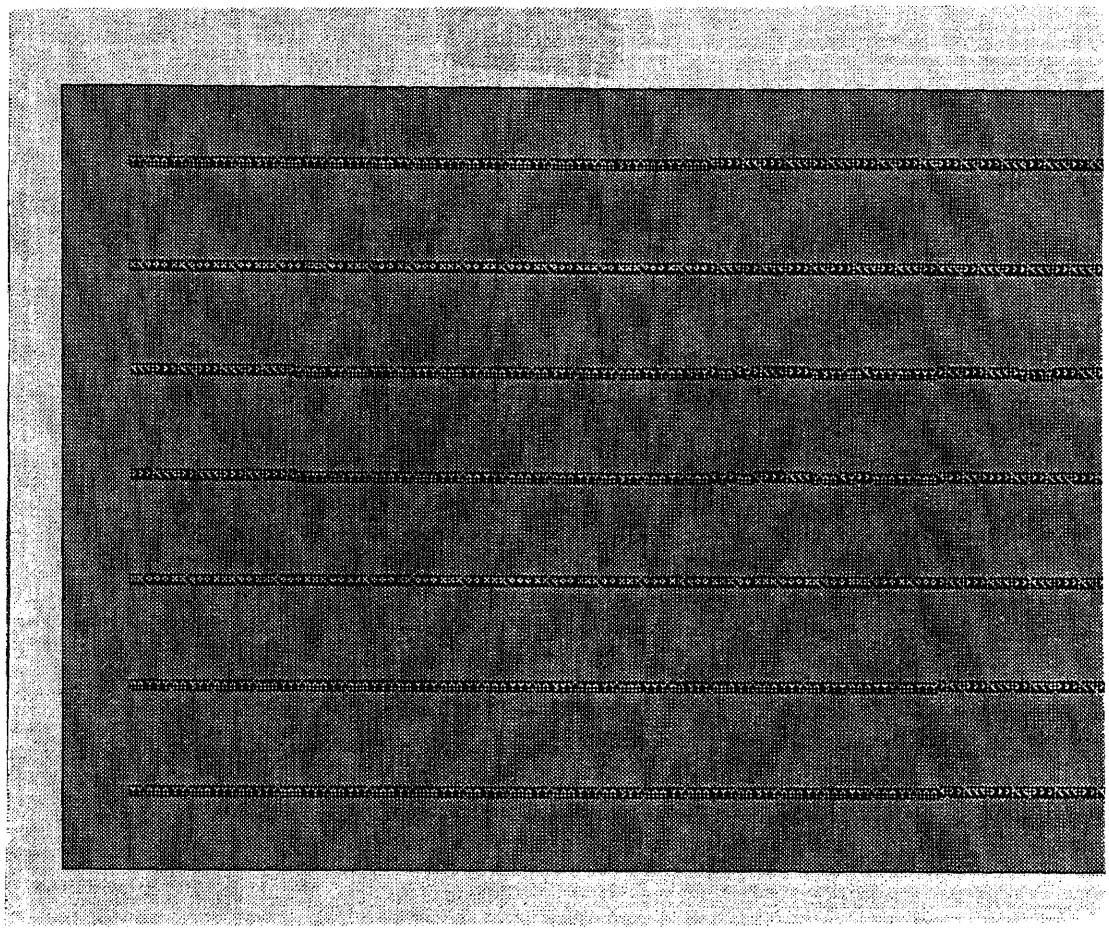

Figure 5.7 (Continued) Expanded view of cathode area.

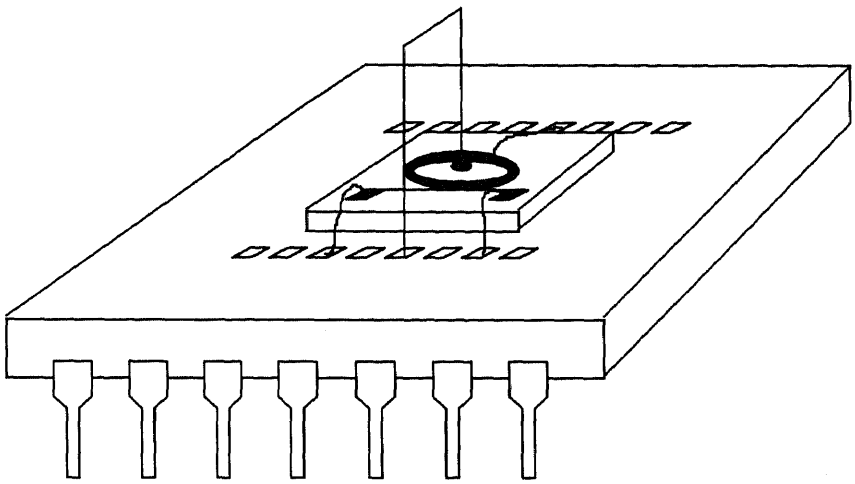

Figure 5.8 Assembled device in a DIP package with ground plane

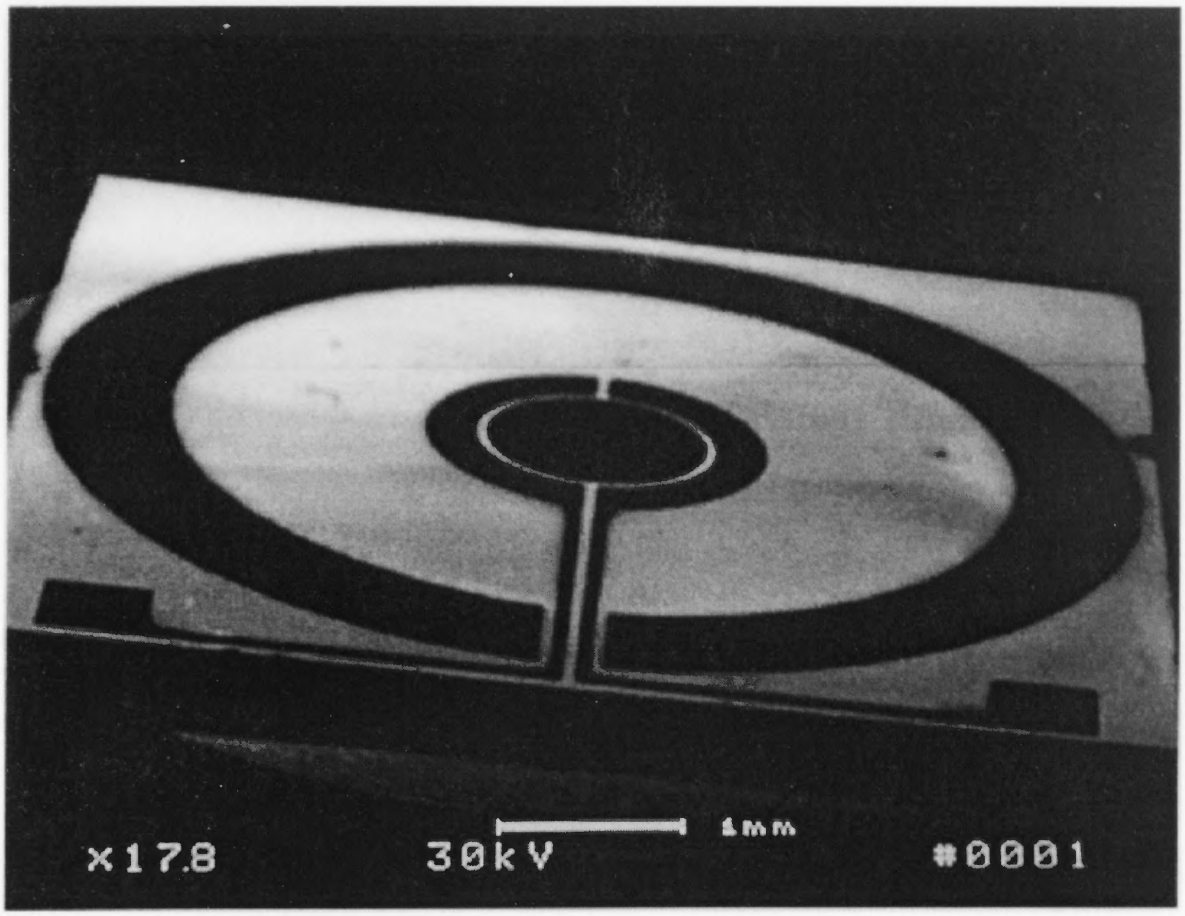

Figure 5.9 SEM photograph of microengineered pressure sensor chip.

CHAPTER 6

ENGINEERING TEST AND CHARACTERIZATION

The engineering test and characterization consist of three parts: field emission current measurement, ion current measurement, and ion current separation analysis. This chapter describes the test environment, test structure, and test circuits for characterization of the microengineered pressure sensor and mass spectrometer. Also the test results are presented and discussed.

6.1 Test Environment

The field emission device must work in a high vacuum environment ($P<10^{-5}$ Torr). A high vacuum system with electrical feedthroughs is needed for characterization of the devices. Figure 6.1 illustrates the high vacuum system used for testing. A mechanical (roughing) pump is first used to evacuate the chamber to a medium vacuum range ($P<10^{-2}$ Torr), then a turbo molecular vacuum pump takes over and continues to evacuate the chamber to a higher vacuum range ($P<10^{-5}$ Torr). Finally, an ion pump is used to lower the pressure below 10^{-8} Torr. The test devices are heated for outgasing. After the system pumps down to the desired vacuum level, the sample gas inlet valve is opened and the sample gas enters the vacuum chamber through a small orifice.

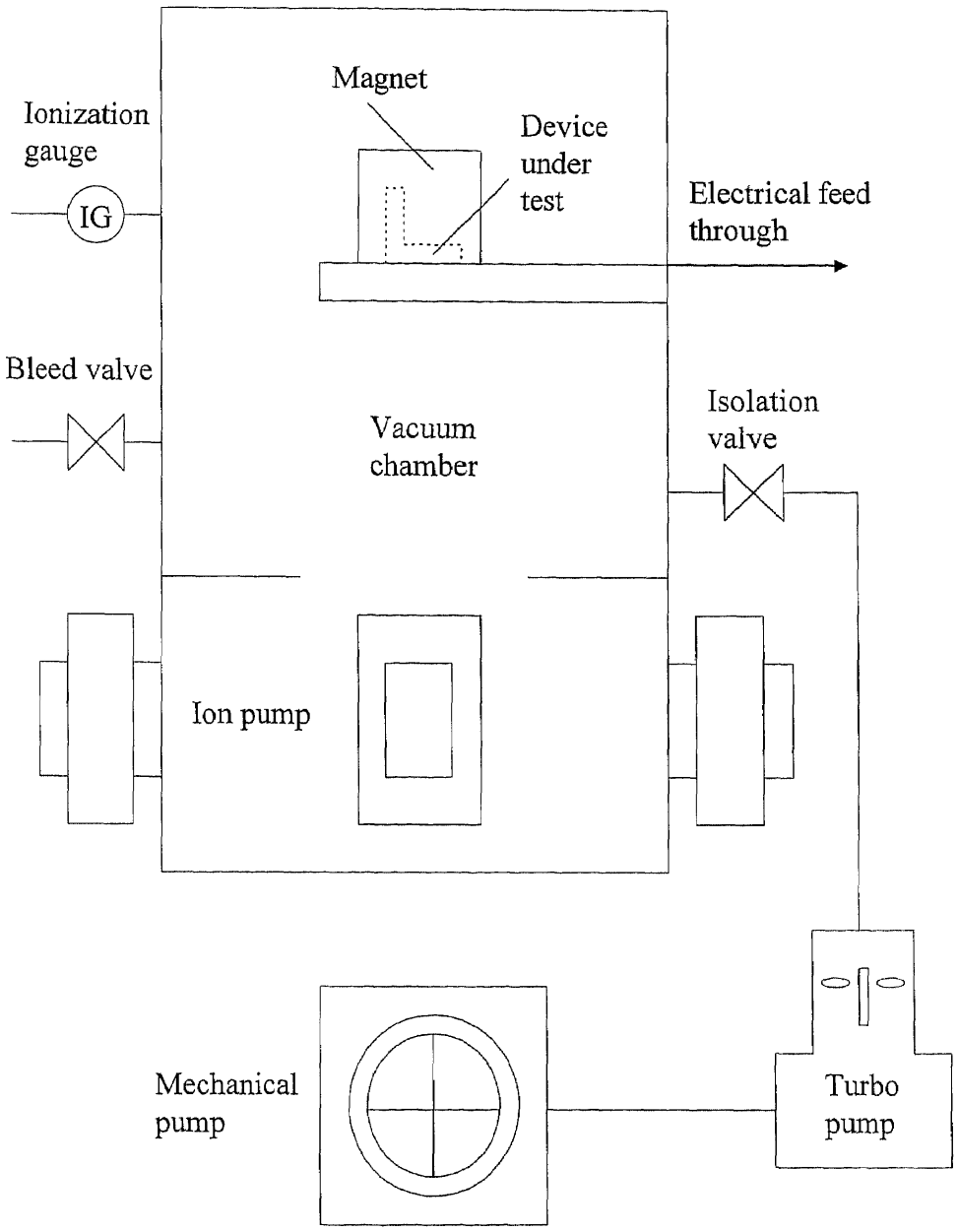

Figure 6.1 Schematic diagram of the high vacuum system used for testing the microengineered mass spectrometer and pressure sensor devices.

6.2 Field Emission Current Measurement

6.2.1 Test Circuits Set-up

Due to the short lifetime of the field emission devices, the field emission current and ion current characterizations are performed on different devices. Figure 6.2 shows the test set-up used for field emission current and leakage current measurements. The electron emitter chip (contains ~7000 microtips) and electron collection chip (a metal layer covering the whole surface) are mounted parallel, i.e., face to face, and separated by approximately 100μm distance. Two power supplies are used to supply stable voltages to the emitter and the collector electrodes. The collector current I_a and the gate current I_g are measured using two Keithley 617 electrometers. The resistor R is used as a current limiter for the gate path to protect the emitter tips from current bursts. The measurement is done under vacuum 10^{-7} Torr at room temperature.

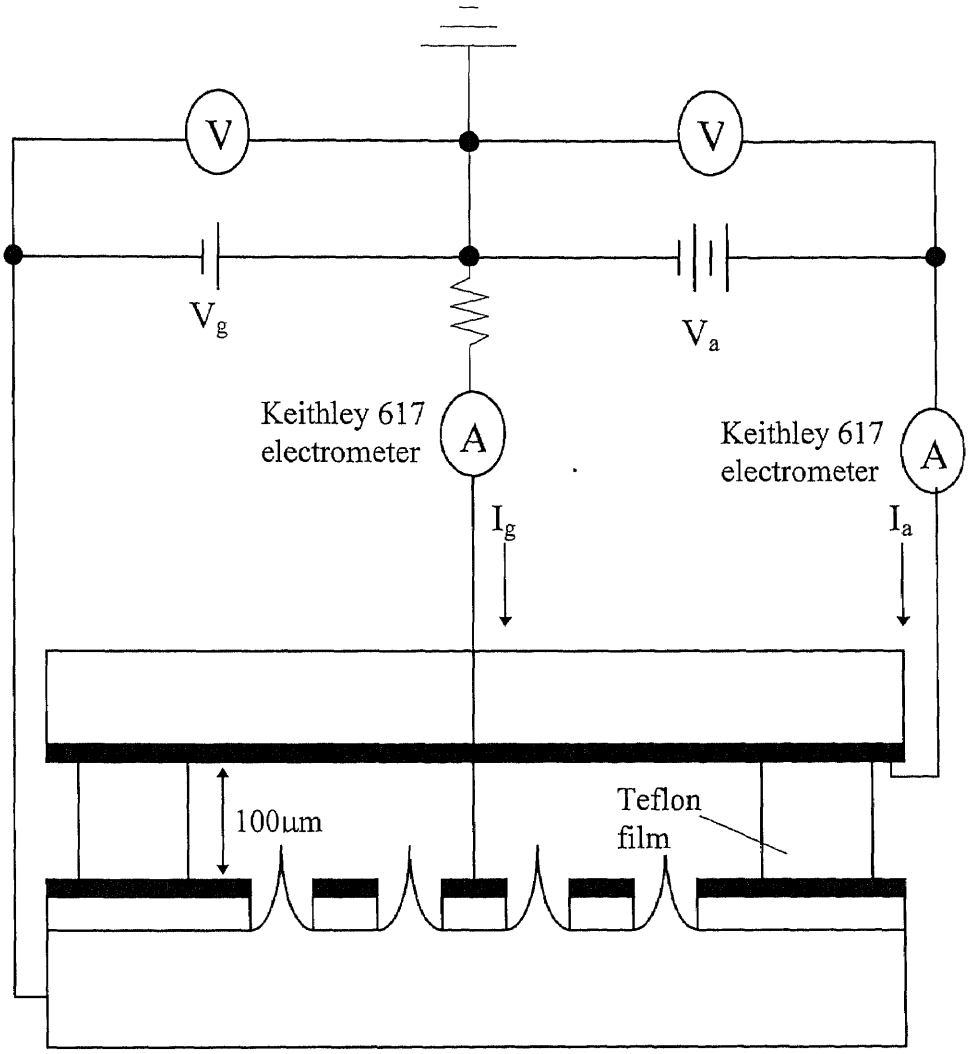

Figure 6.2 Test circuit set-up for field emission current measurement

6.2.2 Test Results and Discussion

As mentioned in chapter 5, the gated microtip array was fabricated by using the self-aligned method, therefore it has relatively high leakage current between the gate and tips than those fabricated by other methods. The leakage test is necessary to presort the field emission chips. This test is done at atmosphere. The maximum voltage applied to the devices should be lower than 5V to prevent devices from oxidizing during this test step. An HP 4140B V-Source/pAmmeter programmed by a PC is used to measure the I-V relations. A typical I-V curve is shown in Figure 6.3. The data of the error bars are based on 90% of the total devices tested. By performing this leakage test, those devices with low leakage current are picked out for field emission tests. The reverse biased leakage current at 150V is lower than 100nA in vacuum of 8×10^{-7} Torr.

The field emission characterization tests are performed on cathodes of both pressure sensor device and mass spectrometer device, which contain 100 and 7000 tips, respectively. A number of chips have been tested and measured for field emission. When field emission started, the initial current is unstable. Figure 6.4 shows a typical emission current as a function of time (device 39-28 with 100 tips). The gate and anode potentials are maintained constant. The current initially increased for a few minutes. This is caused by degasing from the surface of the emitters [42]. After reaching a maximum, the current abruptly drops. This drop in current could indicate burn-out of some of the emitting tips [44]. Figure 6.5 is a SEM photograph which shows the damaged tip array area . It was taken right after a two hour field emission test. The current became relatively stable after a few tens of minutes.

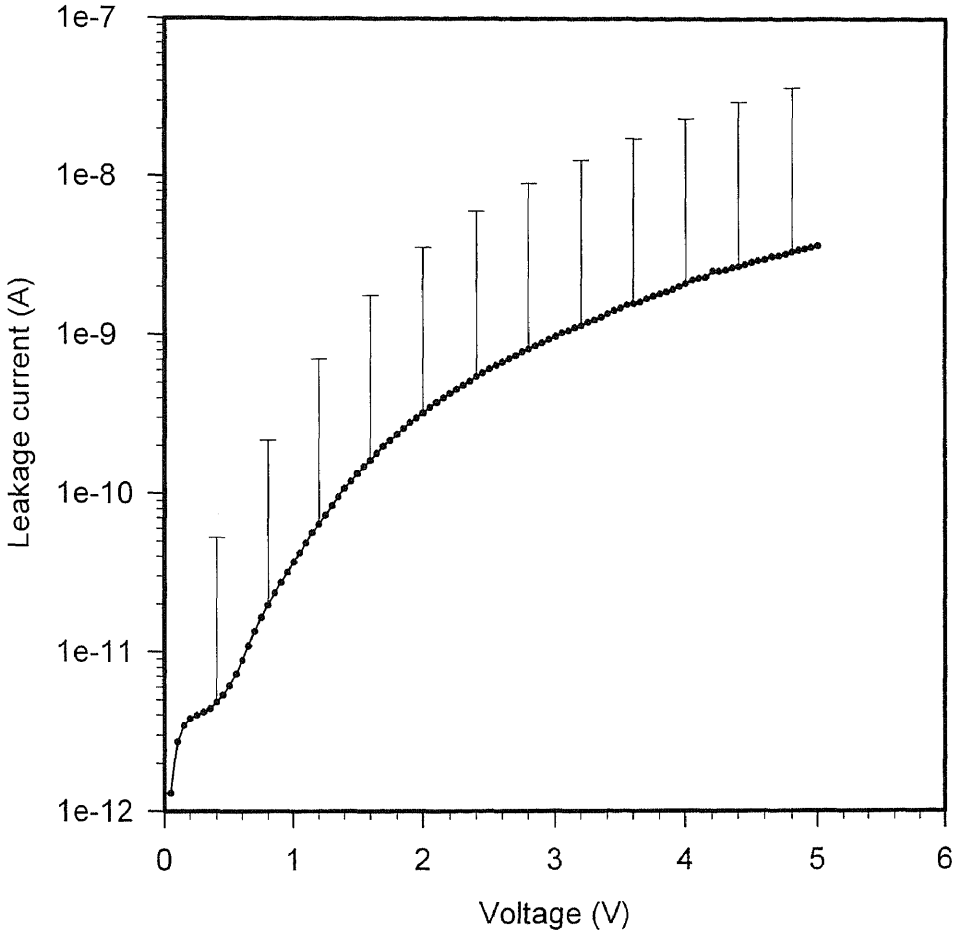

Figure 6.3 Leakage current as a function of applied gate voltage.

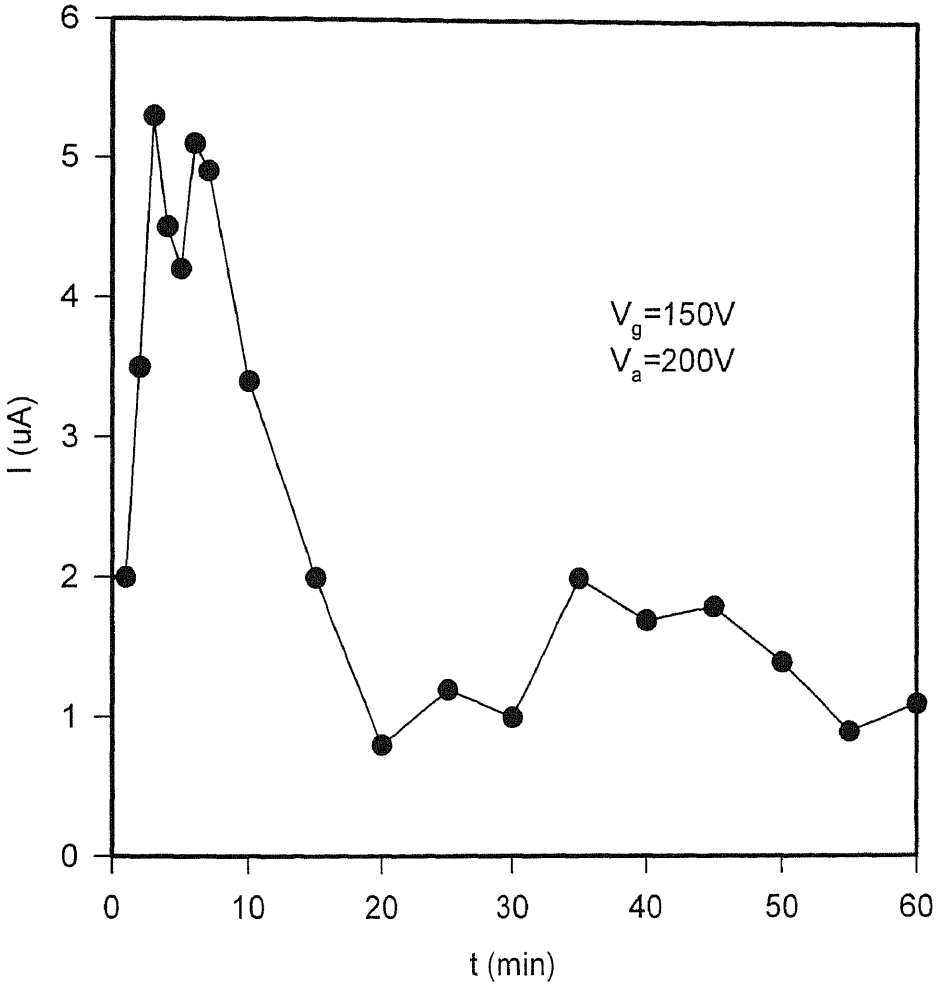

Figure 6.4 Field emission as a function of time for 100 tip array. Pressure is 8×10^{-7} Torr.

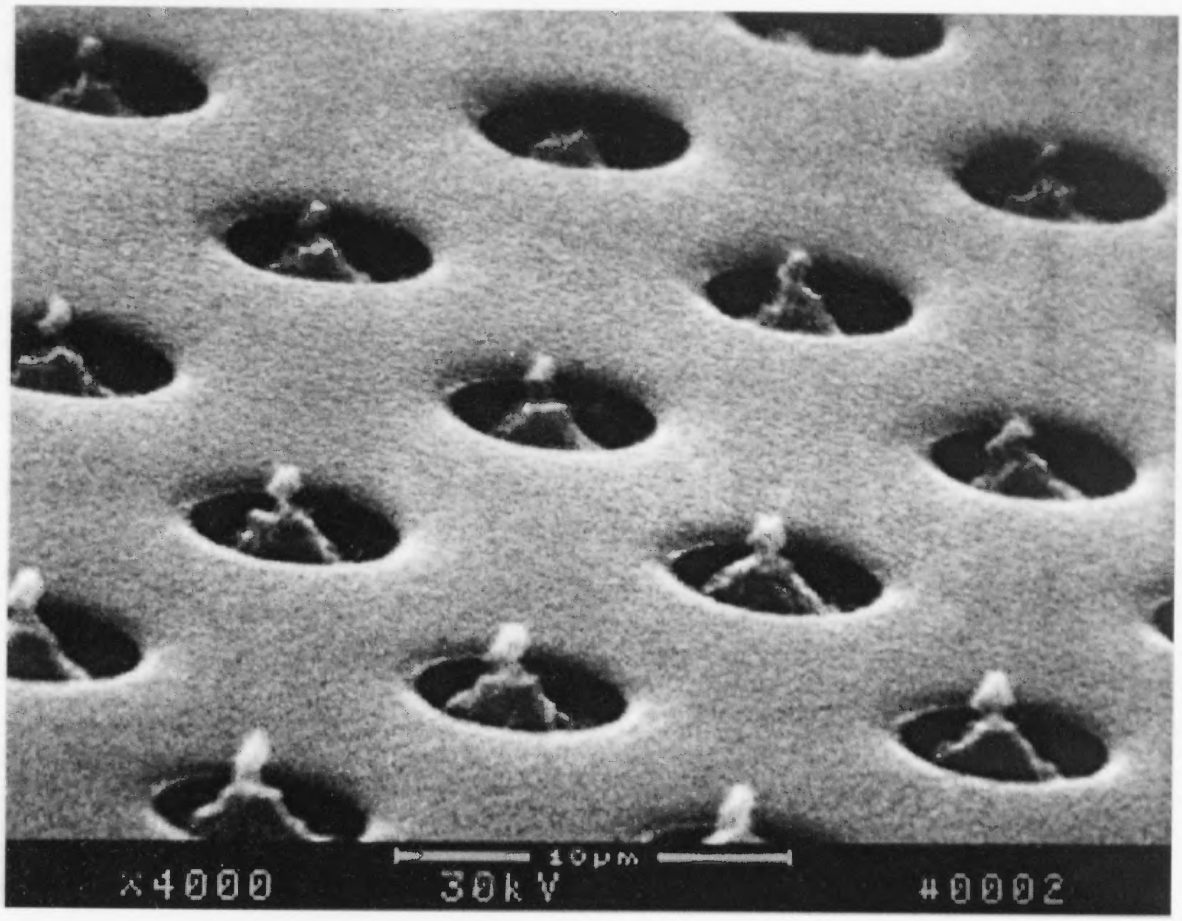

Figure 6.5 SEM micrograph shows the damaged tips after a two hour field emission test.

The data of field emission current I_a vs. gate voltage V_g were taken one hour after emission began. The Fowler-Nordheim plots of the pressure sensor cathode (device 35-32 with 100 tips) and the mass spectrometer cathode (device 38-11 with 7000 tips) are shown in Figures 6.6 and 6.7 respectively.

From the slopes of these two F-N plots, we calculate the field conversion factor α/r and emitting area βr^2 by using Equations (3.11) and (3.8). The results are shown in Table 6.1.

Table 6.1 Values of field conversion factor and emitting area for different cathode.

Device number	Field conversion factor α/r (cm^{-1})	Emitting area βr^2 (cm^2)	Average emitting area per tip (cm^2/tip)
35-32 (100 tips)	3.29×10^{5}	4.99×10^{-11}	4.99×10^{-13}
38-11 (7000 tips)	3.14×10^{5}	2.11×10^{-9}	3.01×10^{-13}

These values are close to those from other silicon tip field emission studies [13] [37] [45-46]. From the table we find that the average emitting area per tip is very small. It indicates that the tip radius could be in the nanometer range. Figures 6.8 and 6.9 show a comparison of field emission characteristics of the 100 tip cathode and the 7000 tip cathode.

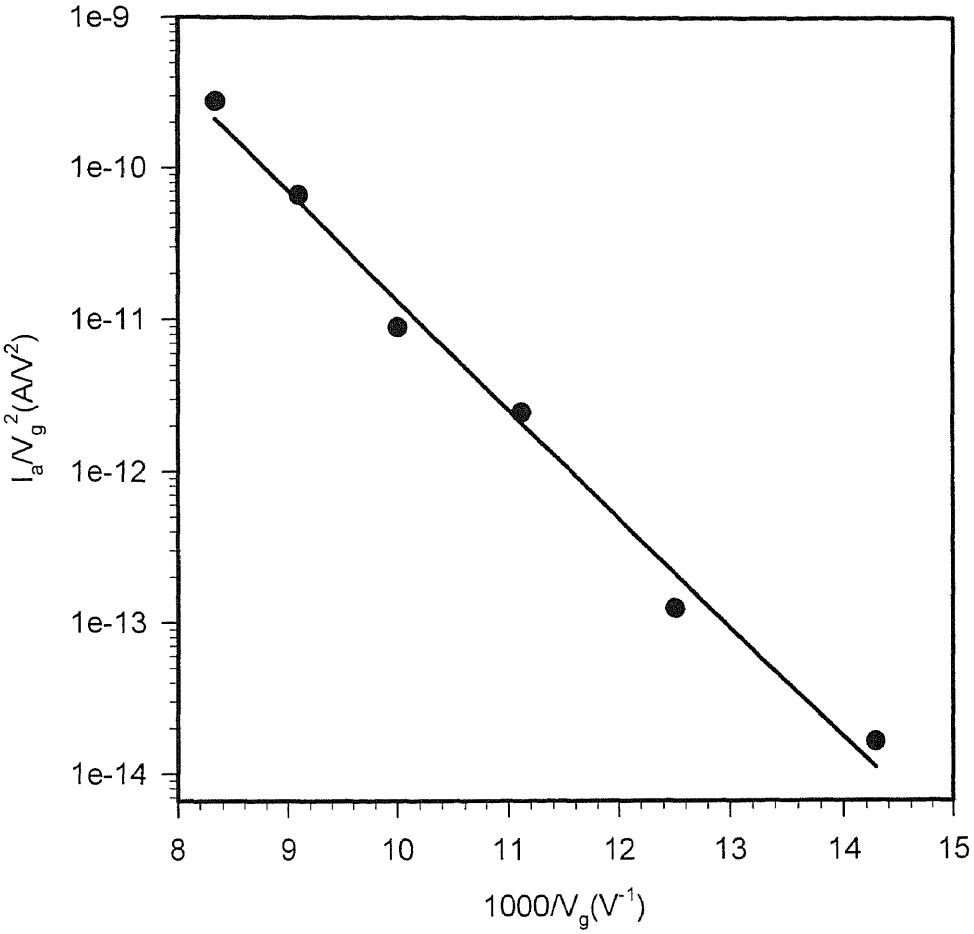

Figure 6.6 Fowler-Nordheim plots of emission from a 100 tip array (cathode of pressure sensor).

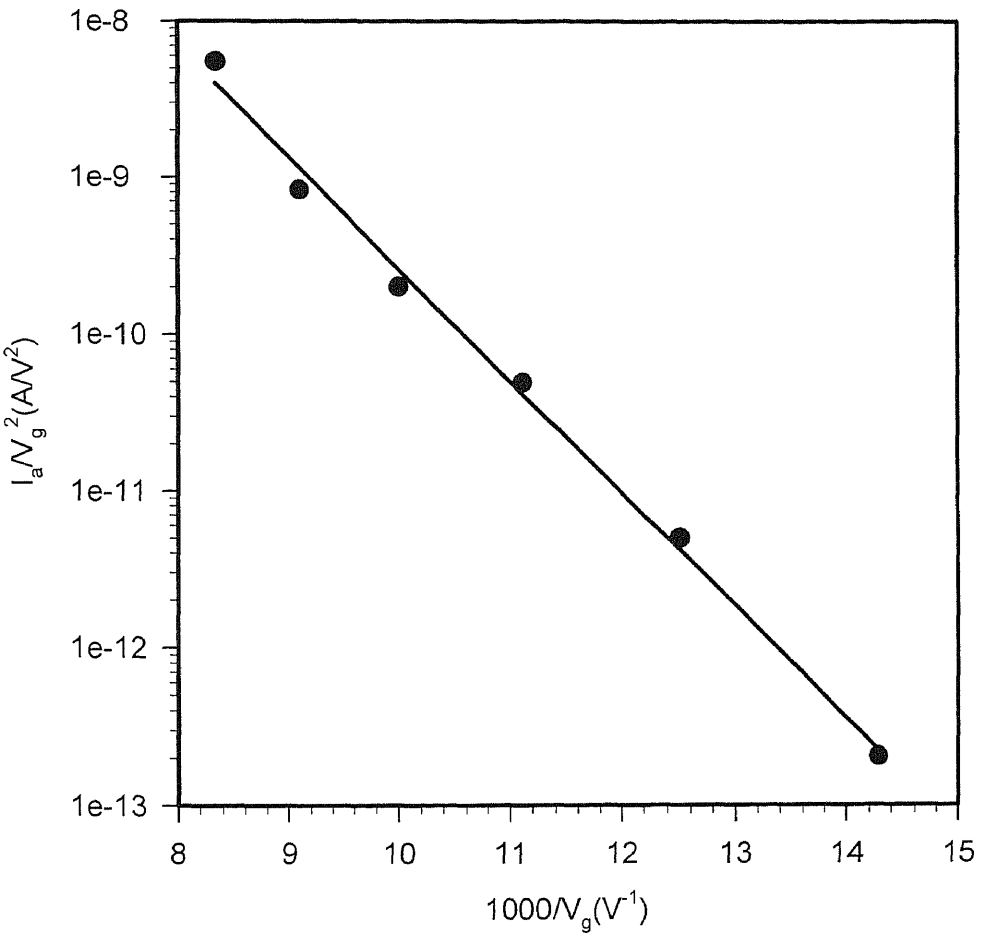

Figure 6.7 Fowler-Nordheim plots of emission from a 7000 tip array (cathode of mass spectrometer).

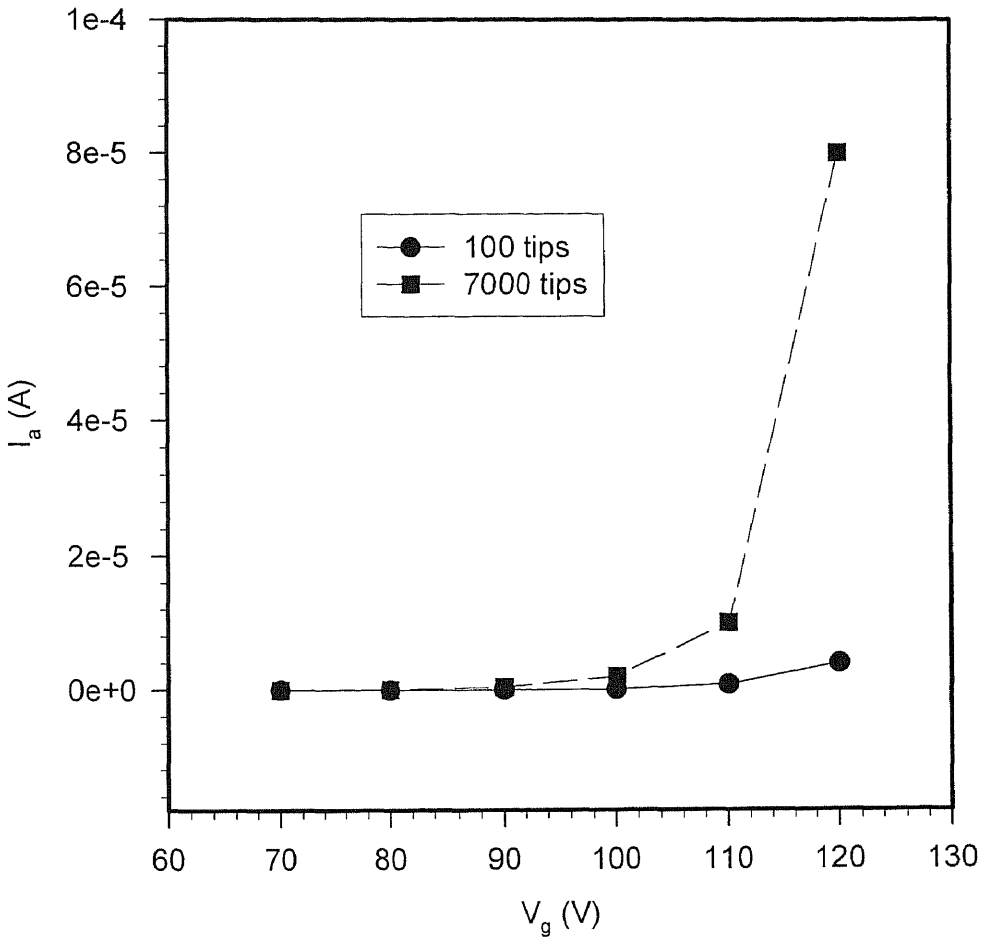

Figure 6.8 Comparison of emission current of a 100 tip cathode with a 7000 tip cathode.

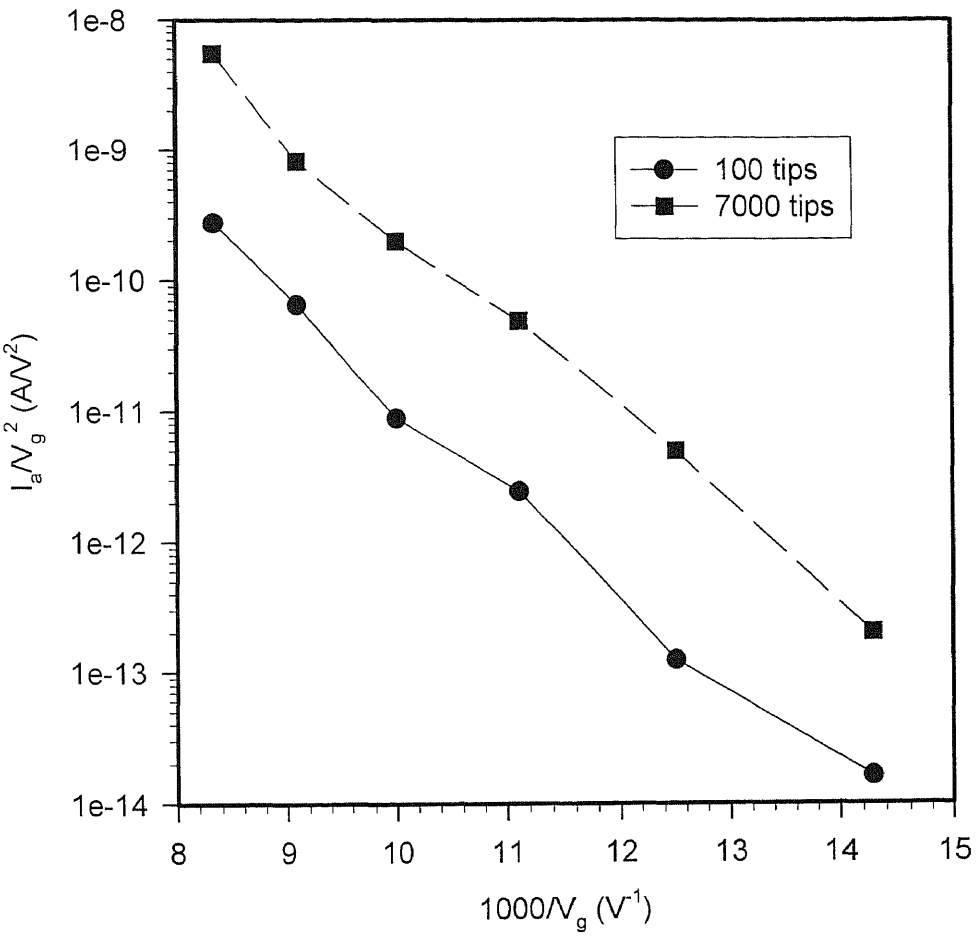

Figure 6.9 Comparison of F-N behavior of a 100 tip cathode with a 7000 tip cathode.

6.3 Characterization of Microengineered Pressure Sensor Device

6.3.1 Test Circuits Set-up

The test set-up used for characterizing the microengineered pressure device is shown in Figure 6.10 The testing chip is mounted on a IC package. A permanent magnet is placed underneath the package to create a 500 Gauss magnetic field that is perpendicular to the chip surface. Two power supplies are used. One is for gate voltage supply and the other is for the electron anode annular ring voltage supply. The ion current is detected by a Keithley 617 electrometer. The pressure in the vacuum chamber can be changed by operating the bleed valve connected to vacuum chamber. It should be noted that the pressure must be lower than 10^{-5} Torr during the measurement to reduce tip contamination, possible oxidation and ion bombardment damage.

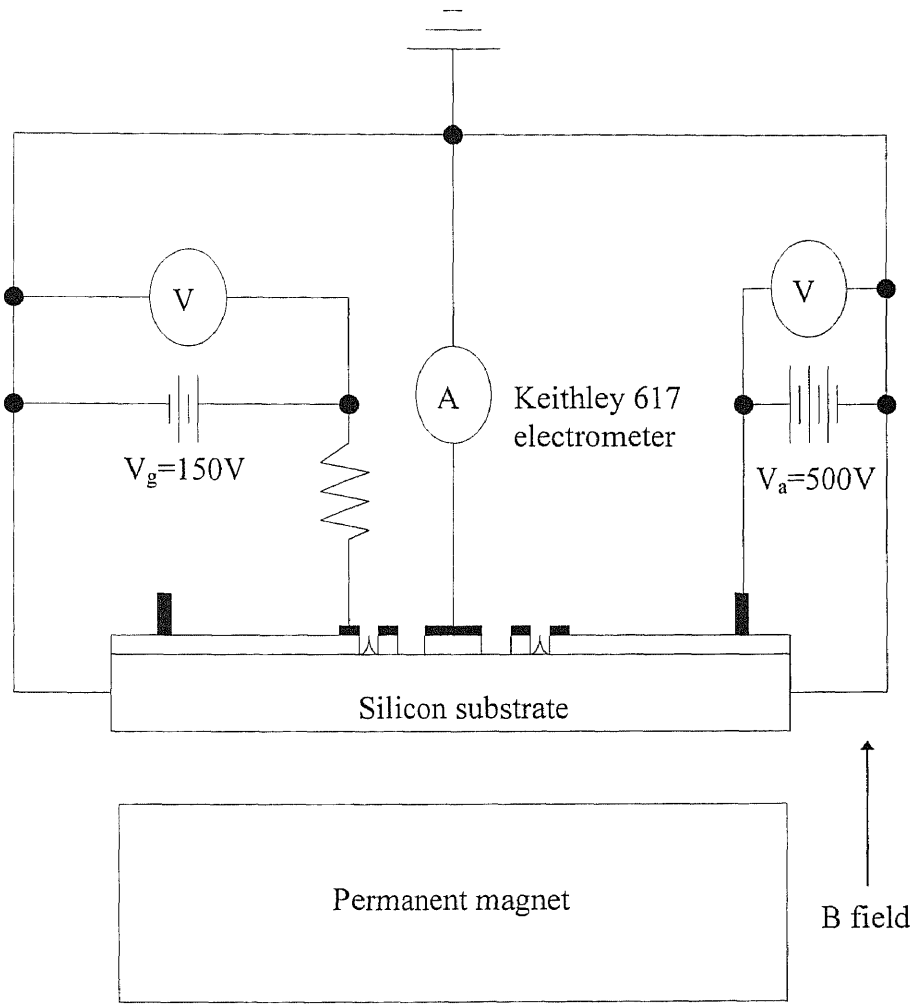

Figure 6.10 Test circuit set-up for microengineered pressure sensor device characterization

6.3.2 Teat Results and Discussion

One of the most important characteristics of the pressure sensor device is the ion current as a function of pressure. Figure 6.11 shows the data measured from device sample 35-28. As the pressure between 1×10^{-6} and 2×10^{-5} Torr, the I-P curve is closed to a straight line. It is consistent with the theoretical analysis. At lower pressure region ($P<1\times10^{-6}$ Torr), the data deviate from straight line. This is caused by noise, capacitance of the feed through and minimum detection limitation of the electrometer. If noise prevention feed through and fA meter are used, the minimum detection pressure can be extended by four orders. After pressure increased to 2×10^{-5} Torr, the oxidation of the silicon cause degradation of the silicon tips. Therefore, the field emission current start to decrease significantly, and the ion current cease to increase with the pressure. Finally, the field emitters are destroyed and the ion current drops to zero. For comparison of ionization efficiency with the other device structure, we define an efficiency related parameter,

$$\kappa = \frac{I_{ion}}{P \cdot I_e} \tag{6.1}$$

where I_{ion} is ion current, P is pressure, and I_e is the field emission electron current. From the data show in Figure 6.11, we have

$\kappa=1500$ Torr^{-1}

It should be noted that the electron emission current data were not taken simultaneously with the ion current measurements. The electron current may vary significantly with the time.

The ratio of ion current to electron current indicates the device ionization efficiency,

$$A = \frac{I_{ion}}{I_e} = \kappa P . \tag{6.2}$$

At certain pressure, e.g. $P=10^{-7}$ Torr, we have $A=1500\times10^{-7}=1.5\times10^{-4}$.

In Chapter 4, we know the electron ionization mean free path

$$\lambda = \frac{1}{n\sigma_{ion}} \tag{4.3}$$

where n is the number of particles per unit volume of gas, and σ_{ion} is the ionization cross section of the collision. For oxygen at 150 eV and 10^{-7} Torr, $\sigma_{ion}\approx4\times8.82\times10^{-17}cm^2$ (Figure 4.7), and $n\approx3.25\times10^{9}$ cm^{-3}. Then $\lambda\approx8.72\times10^{5}cm$. The calculated values of ionization mean free path for oxygen at different pressure are shown in Table 6.2.

Table 6.2 Values of electron ionization mean free path for oxygen at different pressure.

Pressure P (Torr)	Molecular density n (cm^{-3})	Ionization mean free path λ (cm)
760	2.46×10^{19}	1.15×10^{-4}
1	3.25×10^{16}	8.72×10^{-2}
10^{-3}	3.25×10^{13}	8.72×10^{1}
10^{-6}	3.25×10^{10}	8.72×10^{4}
10^{-9}	3.25×10^{7}	8.72×10^{7}
10^{-12}	3.25×10^{4}	8.72×10^{10}
10^{-15}	3.25×10^{1}	8.72×10^{13}

On the other hand,

$$A = \frac{l}{\lambda} = n\sigma_{ion} l \tag{6.3}$$

where l is the average path that each electron travels (one circle). From Figure 4.4, we can estimate $l \approx 3.14$cm. Therefore, we have $A \approx 3.6 \times 10^{-6}$.

Substituting equation (2.14) into (6.3), we get

$$A = \frac{l}{\lambda} = n\sigma_{ion} l = 9.656 \times 10^{18} \times \frac{P}{T} \sigma_{ion} l \tag{6.4}$$

Figure 6.12 shows a comparison of experimental and theoretical curves of A vs. P. The theoretical curve are based on equation (6.4). From the curves, we find that the experimental value of A is 40 times higher than that of the theoretical value at the same pressure. The possible reasons that cause the high ionization efficiency are:

(1) The electron current was measured at a different time compared to the ion current. This accounts for an error in I_{ion}/I_e.

(2) The theoretical calculated A is based on a single 360° orbit for the electron. In actual fact, the electrons may be traversing the ionizing volume many times, in which the theoretical value of I_{ion}/I_e could increase in proportion to the total electron path.

(3) Localized degasing may cause an increased gas pressure near the tip array, making the measured vacuum pressure inaccurately low. In this case, the experimental data would refer to pressures lower than actual.

(4) An ionizing event may be accompanied by the secondary emission of one or more additional electrons. This phenomenon when included into a more precise calculation would increase the theoretical value of I_{ion}/I_e.

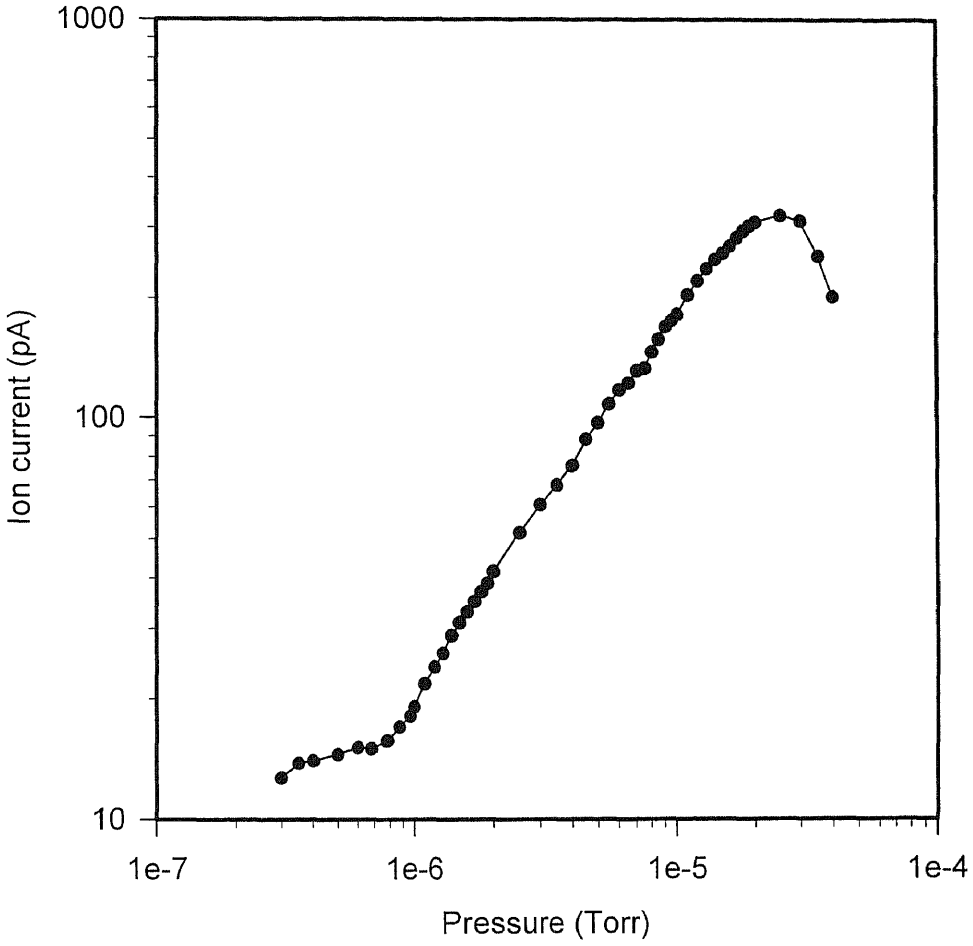

Figure 6.11 Ion current as a function of pressure (pressure sensor). V_g=150V. V_a=500V.

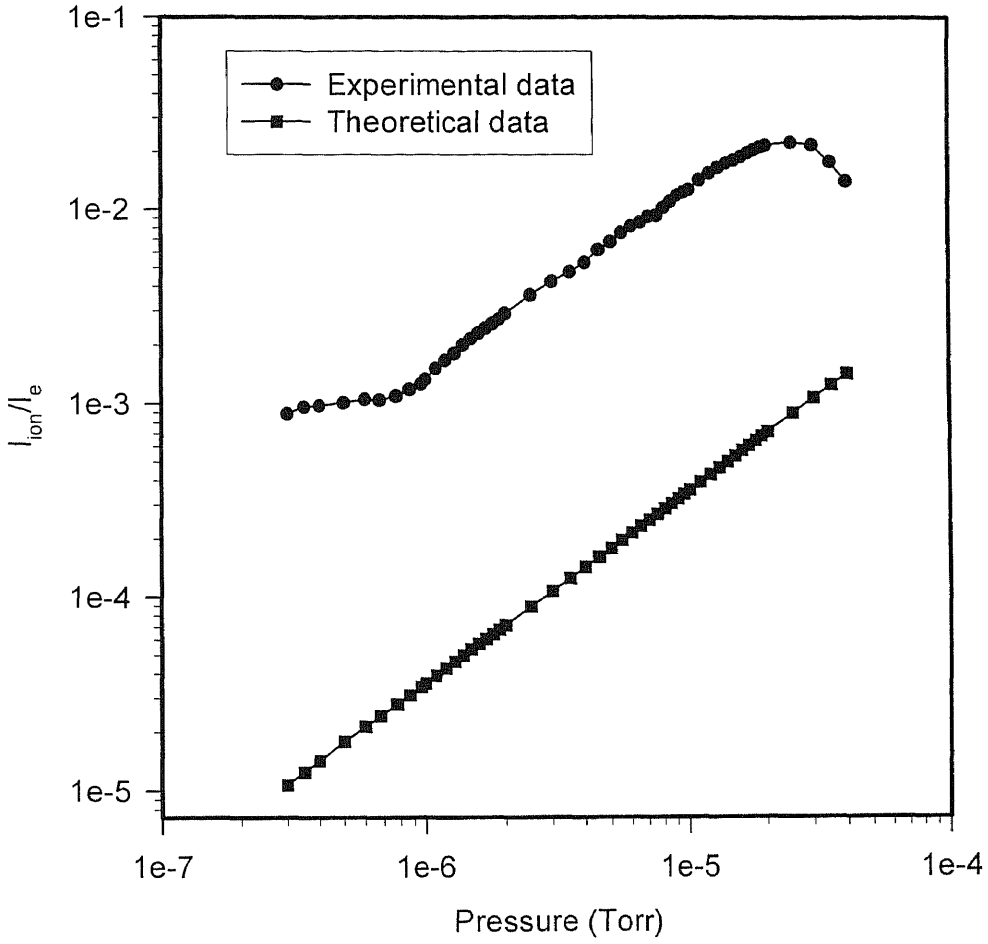

Figure 6.12 Comparison of experimental and theoretical A vs. P curves for pressure sensor device.

6.4 Characterization of Microengineered Mass Spectrometer Device

6.4.1 Test Circuit Set-up

The test set-up used for microengineered mass spectrometer characterization is shown in Figure 6.13. Two chips (field emission tip array and ion collector) are parallel mounted, face to face and separated by a 1mm distance. Each of the ion collector stripes can be switched to connected in series with a Keithley 617 electrometer. Different kinds of sample gases are fed through the bleed valve. These two chips are put in a gap between two parallel permanent magnets. A fairly uniformed 3000 Gauss magnetic field is built for ion separation test. Two measurements are performed for characterizing this mass spectrometer device: ion current vs. pressure characteristic and ion separation.

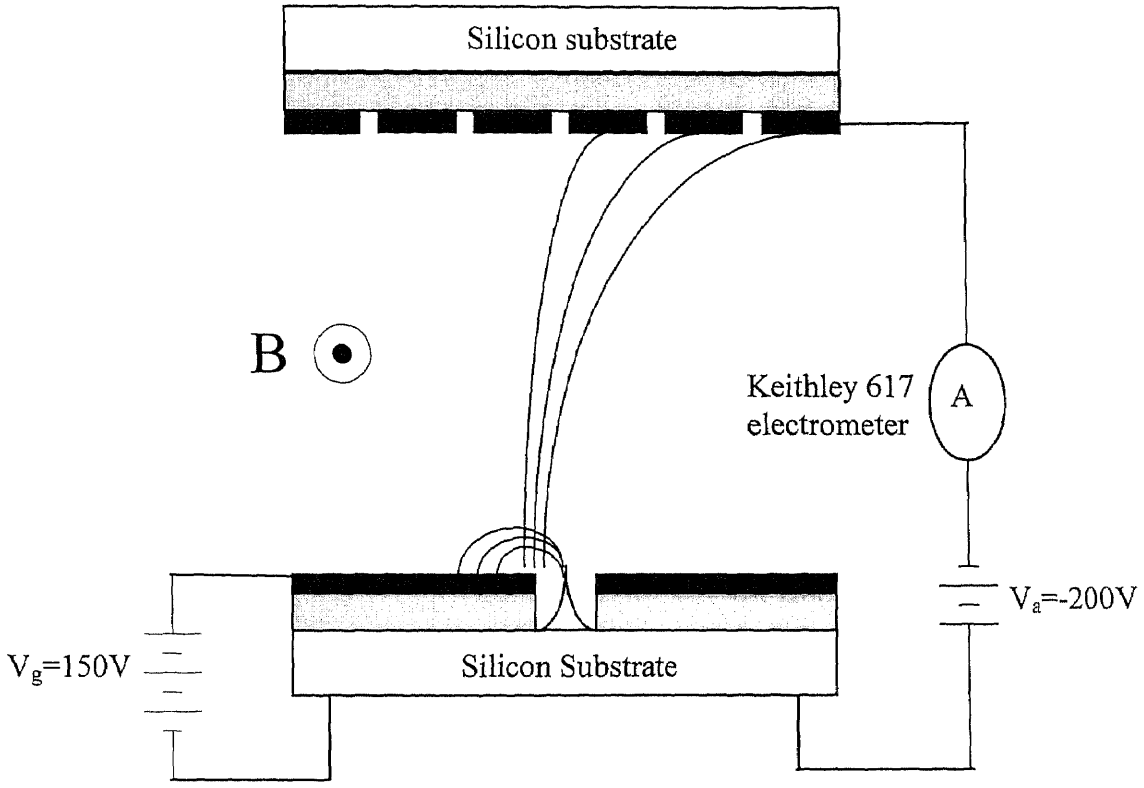

Figure 6.13 Test set-up for microengineered mass spectrometer characterization

6.4.2 Test Results and Discussion

The first test is to measure the ion current vs. pressure characteristic, which is similar to the procedure described in section 6.3. During this measurement, all ion collection stripes are electrically connected together. The ions of all kinds of gases are totally collected, and no gas discrimination occurred at this point. The ion current vs. pressure measurement is performed on three different field emission chips, which labeled 38-15, 38-32 and 38-58, respectively. The average ion current vs. pressure behavior is shown in Figure 6.14. The analysis of this curve is similar to Figure 6.11. The I-P curve is a straight line for the pressure below 2×10^{-5} Torr,. The device failure happened when pressure exceeded 2×10^{-5} Torr, because of the tip degradation. From the data show in Figure 6.14, we have

$$\kappa=170\ \text{Torr}^{-1}$$

The average electron current $I_e=40\mu A$ is used for calculation. To increase the ion current, the mass spectrometer is designed with great number of field emission tips.

Using Equation 6.2, the experimental value of A at 10^{-7} Torr is obtained, $A=\kappa P=170\times10^{-7}=1.7\times10^{-5}$.

Similar to the analysis for pressure sensor device, we calculate the ratio of ion current to electron current using Equation (6.3). The average electron path l for mass spectrometer device can be estimated $l\approx500\mu m$ (Figure 4.14(b)). The other parameters remain the same as of pressure sensor. We have $A\approx5.7\times10^{-8}$.

Figure 6.15 shows a comparison of experimental and theoretical curves of A vs. P. The theoretical curve are based on equation (6.4). From the curves, we find that the experimental value of A is 300 times higher than that of the theoretical value at the same pressure. The same discussion given to explain the discrepancy for I_{ion}/I_e for the case of

the pressure sensor device also applies to the present mass spectrometer device discussion. In addition, the ratio of the experimental to theoretical ionizing efficiency is higher for the mass spectrometer compared to case of the pressure sensor. This difference may be related to the following factors:

(1) The ion collector covers the whole electron emitting area of the mass spectrometer device, almost 100% of the ions are collected. But for pressure sensor device, only a small portion of the ions are collected.

(2) The high electric field between the gate and ion collector for the mass spectrometer device may induce a plasma arc discharge, which could create a large ion current.

(3) A non-uniform magnetic field may cause deviation of electron trajectories from the simulation. As a result, the electron paths might increase. This factor is however considered unlikely.

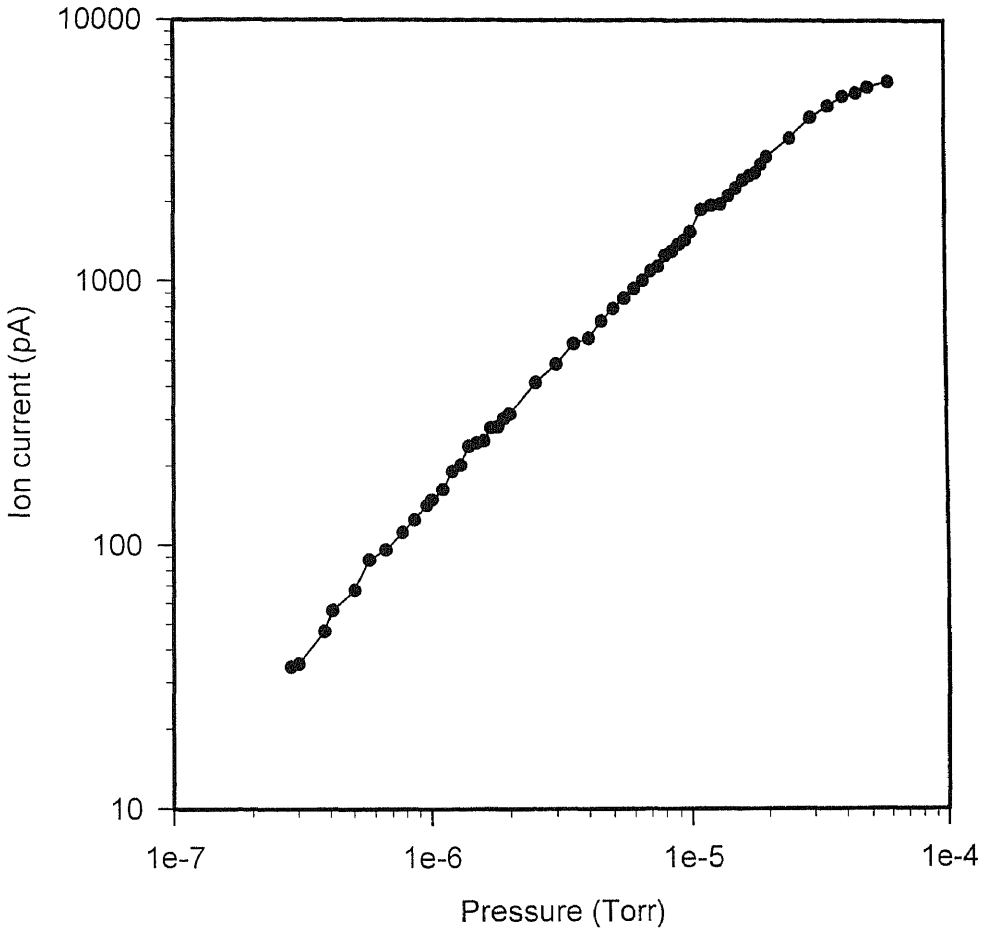

Figure 6.14 Ion current as a function of pressure (spectrometer). V_g=150V. V_a=-200V.

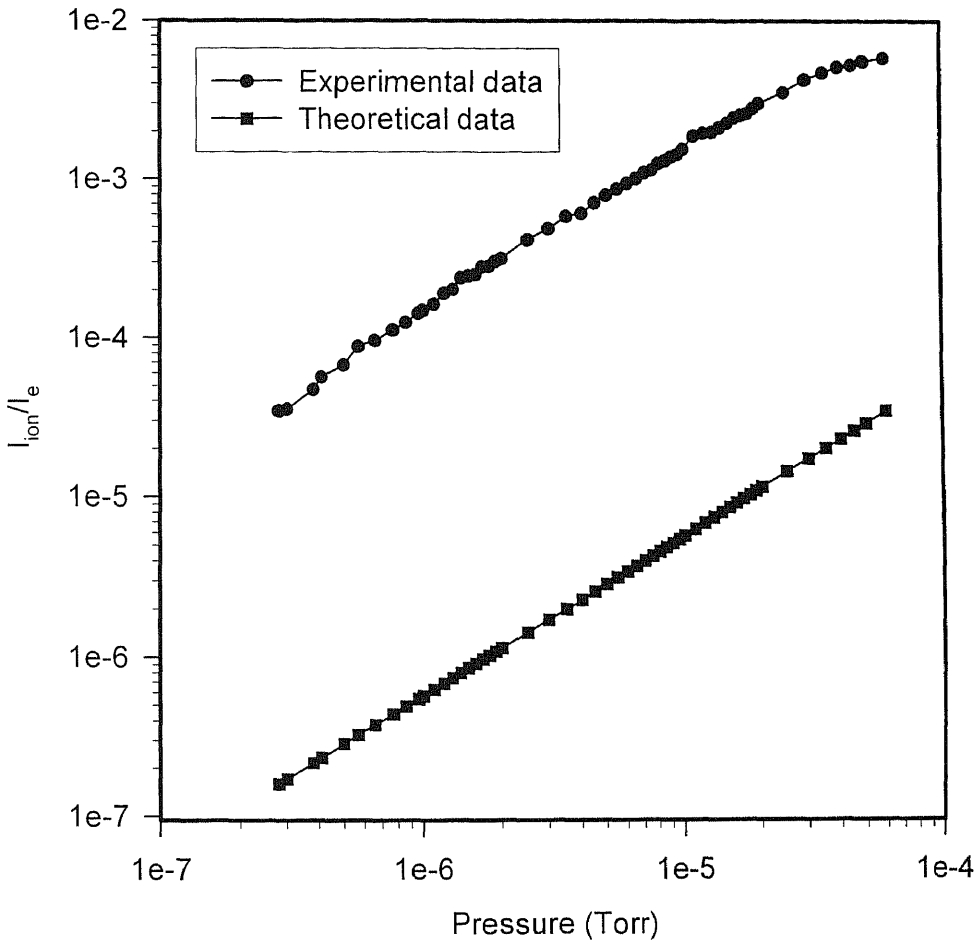

Figure 6.15 Comparison of experimental and theoretical A vs. P curves for mass spectrometer device.

The second test is to evaluate the ion separation ability of the mass spectrometer device. The resolution of this device is limited by its tiny and simple structure. The lifetime of the devices is also very short. Therefore, the test of gas analysis capability of the mass spectrometer is beyond the scope of this dissertation and cannot be completed at current stage. The goal of this test is to prove the ideas that the spectrometer can be scaled down to IC chip size, and the ion trajectories can be controlled by magnetic field. During that measurement, the ion collector is divided into two regions, left and right. All ions should go to rightside collector when magnetic field is applied. But the ions will go evenly to both leftside and rightside collectors if magnetic field is withdrawn. Figure 6.16 shows the ion current collected at different ion collector with and without magnetic field. The testing pressure was 2×10^{-6} Torr. When 3000 Gauss magnetic field was applied, the ion trajectories was bent to upright side and a maximum current of 82pA was measured at rightside collector. Then the magnetic field was withdrawn, the ions went upward and a equal amount current of 58pA was measured at each of the left and right side collectors respectively.

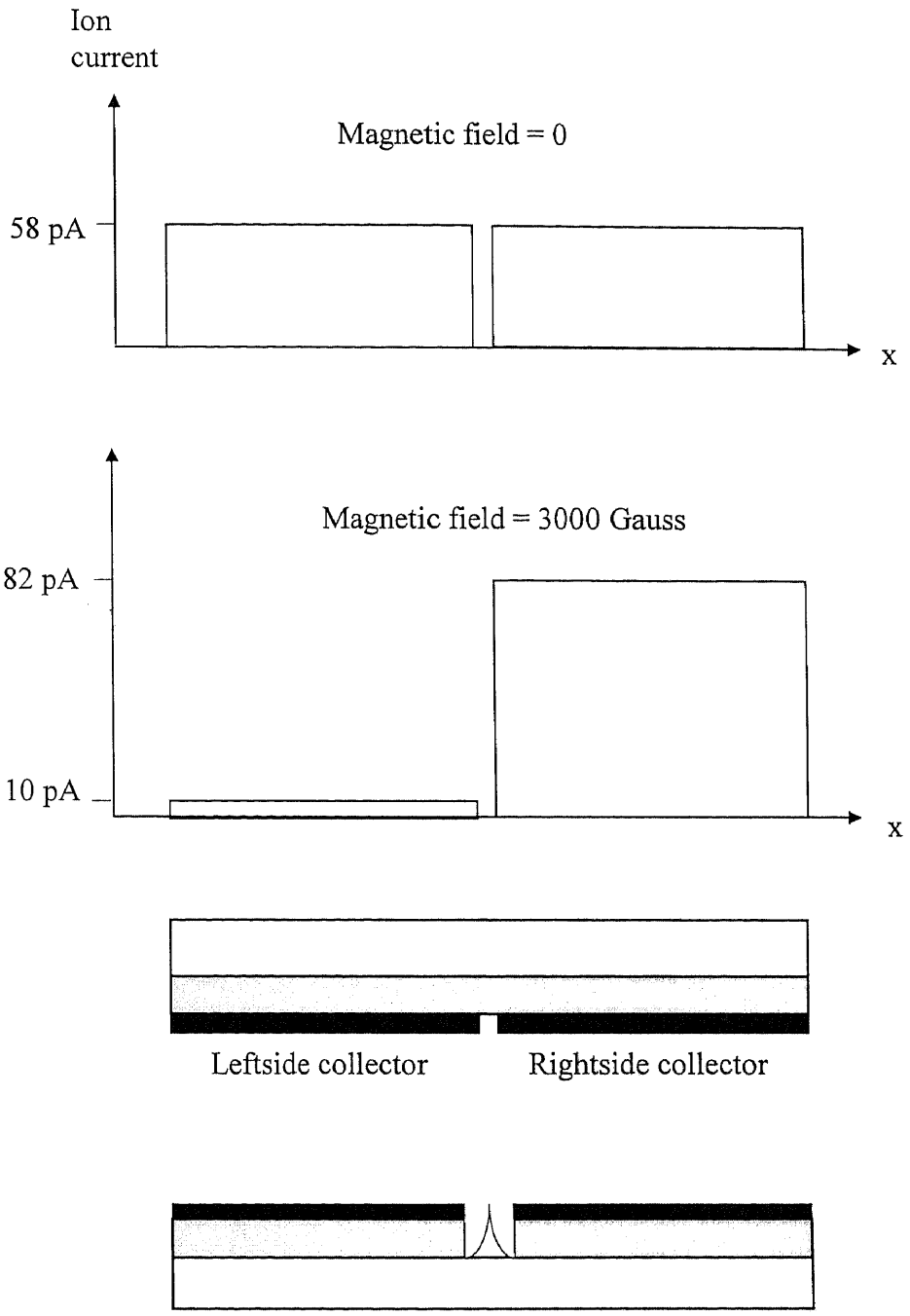

Figure 6.16 Comparison of ion current collected at different electrodes with and without magnetic field

6.5 Device Failure and Lifetime

The vacuum arc phenomenon may completely destroy the field emitters during measurement. It is initiated by the high emission current density, and is easily happened during device characterization [13][47-51]. The device failure problem is mainly caused by this vacuum arc phenomenon, and has been observed in testing the microengineered pressure sensor and mass spectrometer devices. Low vacuum degree in some local region of vacuum chamber and material outgasing are possible causes of the vacuum arc. Before measurements, each device was pre baked for 5 minutes at atmosphere, then put into vacuum chamber to pump down for couple of days. It could help to reduce the material outgasing.

The lifetime of the device is limited not only by vacuum arc phenomenon, but also by the high leakage current density between some tips and gate electrode. Since the metal deposition is not perfectly directional, some individual tips might be smeared with metal and the electrical shortage channels formed. This shortage current could cease field emission and damage the tips. It could also heat some local emission surface area and cause outgasing. Therefore the vacuum arc could easily happen. To reduce to shortage current, e-beam directional deposition is used in fabrication the gated electrode. The thickness of the metal layer is less than 2000 Å. The possibility of electrical shortage is significantly reduced by these fabrication approaches.

CHAPTER 7

SUMMARY

This research work has concentrated on the design, fabrication, and characterization of a microengineered pressure sensor device and a mass spectrometer device. The main results of this work are as follows:

(1) A microengineered pressure sensor device has been designed, fabricated, and tested. The dimension has been scaled down to 1cm by 1cm. It is the first report of a magnetic ionizing type pressure (vacuum) sensor with a field emission electron source on a chip. To date, no such device has appeared in the literature.

(2) Simulation results for the microengineered pressure sensor device show that the paths of electrons emitted from the cathode tip array are greatly lengthened using our specially designed structure and carefully chosen combination of electric and magnetic fields. This makes it possible to scale down the device dimension without reducing its sensitivity.

(3) The microengineered pressure sensor is a monolithic and planar device, with all essential features fabricated on a single silicon chip.

(4) The test results for the microengineered pressure sensor device show that the ion current is a linear function of pressure. This is consistent with the theoretical modeling and simulation.

(5) A microengineered mass spectrometer device has been designed, fabricated, and tested. The dimensions have been scaled down to 1cm by 1cm. A number of different

structures were simulated and the optimized geometry of this device was selected. It is the first miniature mass spectrometer using a field emission electron source.

(6) Fowler-Nordheim field emission behaviors was investigated. Our results are closed to those of other silicon tip field emission studies found in literature.

(7) Due to its simple and tiny structure, the resolution of this microengineered mass spectrometer is lower than conventional mass spectrometer. The non-uniform magnetic field also limits the resolution.

(8) The test results show that ion trajectories can be controlled by the crossed combination of electric and magnetic fields. By changing the applied electric and magnetic fields, ions of different mass can be directed to different collector.

(9) The test results show that this microengineered mass spectrometer can also be used as pressure sensor. The ion current is a linear function of pressure.

(10) The device failure of the cathode has been observed. Cathode oxidation and outgassing are likely responsible for this failure. Because the cathodes of both microengineered devices are field emission arrays, their lifetime is limited by oxidation or degradation of the silicon tips. These problems may be improved by using metal coated field emission tips.

REFERENCES

[1] A. Berman, *Total Pressure Measurements in Vacuum Technology,* chap.4, Academic Press Inc., New York, 1985.

[2] J. F. O'Hanlon, *A User's Guide to Vacuum Technology,* chap.5, John Wiley & Sons, Inc., New York, 1989.

[3] F. A. White, *Mass Spectrometry in Science and Technology*, chap.2, John Wiley & Sons Inc., New York, 1968.

[4] A. Roth, *Vacuum Technology,* chap.2, North-Holland Publishing Company, Amsterdam, 1982.

[5] R. Gomer, "Theory of Field Emission," *Field Emission and Field Ionization,* Harvard University Press, Cambridge, 1961.

[6] W. P. Dyke, and W. W. Dolan, "Field Emission," *Advances in Electronics and Electron Physics,* vol.8, edited by L. Marton, p.89, Academic Press Inc., New York, 1956.

[7] R. W. Wood, "A New Form of Cathode Discharge and the Production of x-rays, Together with Some Notes on Diffraction," *Phys. Rev.,* vol.5, No. 1, p.1, 1897.

[8] R. H. Fowler, and L. Hordheim, "Electron Emission in Intense Electric Fields," *Proc. R. Soc. of London,* A119, p.173, 1928.

[9] W. W. Dolan, W. P. Dyke, and J. K. Trolan, "The Field Emission Initiated Vacuum Arc II. The Resistively Heated Emitter," *Phys. Rev.,* vol.91, No.5, p.1054, 1953.

[10] W. P. Dyke, J. K. Trolan, E. E. Martin, and J. P. Barbour, "The Field Emission Initiated Vacuum Arc I. Experiments on Arc Initiation," *Phys. Rev.,* vol.91, No.5, p.1043, 1953.

[11] K. R. Shoulders, "Microelectronics Using Electron-Beam-Activated Machining Technologies," *Advances in Computers,* Edited by F. L. Alt, vol.2, p.135, Academic Press, New York, 1961.

[12] A. Modinos, "Electron Emission from Free-Electron Metals," *Field, Thermionic, and Secondary Electron Emission Spectroscope,* Plenum, New York, 1984.

[13] C. A. Spindt, I. Brodie, L. Humphey, and E. R. Westerberg, "Physical Properties of Thin-Film Field Emission Cathodes with Molybdenum Cones," *J. Appl. Phys.*, vol.47(12), p.5248, 1976.

[14] R. H. Good, Jr., and E. W. Muller, "Field Emission," *Handbook Der Physik, vol.XXI, Electron-Emission Gas Discharge I,* p. 176, Springer-Verlag, Berlin, 1956.

[15] R. E. Burgess, and H. Kroemer, "Corrected Values of Fowler-Nordheim Field Emission Functions v(y) and s(y)," *Phys. Rev.*, vol.90, No.4, p.515, 1953.

[16] H. C. Lee, and R. S. Huang, "Simulation and Design of Field Emitter Array," *IEEE Electron Devices Lett.*, vol.11, No.12, p.579, 1990.

[17] E. L. Murphy, and R. H. Good, Jr., "Thermionic Emission, Field Emission, and the Transition Region," *Phys. Rev.*, vol.102, No.6, p.1464, 1956.

[18] K. L. Jensen, "Improved Fowler-Nordheim Equation for Field Emission from Semiconductors," *J. Vac. Sci. Technol.*, vol.B13(2), p.516, 1995.

[19] I. Brodie, "Physical Consideration in Vacuum Microelectronics Devices," *IEEE Trans. Electron Devices,* vol.36(11), p.11, 1990.

[20] S. C. Brown, *Basic Data of Plasma Physics,* chap.5, John Wiley & Sons, Inc., New York, 1959.

[21] T. Utsumi, "Vacuum Microelectronics: What's New and Exciting," *IEEE Trans. Electron Devices,* vol.38(10), p.2276, 1991.

[22] S. M. Sze, Semiconductor Sensors, chap.1, John Wiley & Sons, Inc., New York, 1994.

[23] D. A. Dahl, and J. E. Delmore, *The SIMION User's Manual,* EG & G Idaho Inc., 1988.

[24] S. Wolf, and R. N. Tauber, *Silicon Procassing for the VLSI Era,* Lattice Press, Sunset Beach, CA, 1986.

[25] Essam Nasser, *Fundamentals of Gaseous Ionization and Plasma Electronics,* Wiley-Interscience, New York, 1971.

[26] J. R. Tesmer, and M. Nastasi, *Handbook of Modern Ion Beam Materials Analysis,* Materials Research Society, Pittsburgh, PA, 1995.

[27] C. Sun, "Microengineered Mass Spectrometer with Field Emission Electron Ionization Source," Master thesis, Dept. of E. E., NJIT, 1993.

[28] L. Marton, *Advances in Electronics and Electron Physics,* vol.8, Academic Press Inc., New York, 1956.

[29] W. N. Carr and A. Gui, "Comparison of Vertical and Lateral Triode Characteristics Modeled Performance," *Technical Digest of IVMC 90*, p.9. 1990.

[30] W. N. Carr, H. J. Wang, and K. K. Chin, "Vacuum Microtriod Characteristics," *J. Vac. Sci. Technol.,* vol.A8(4), p.3581, 1990.

[31] P. Kopka, and H. Ermert, "Characterization of Field Emitter Structures by Means of Modeling Electron Trajectories in Vacuum," *J. Vac. Sci. Technol.,* vol.B13(2), p.545, 1995.

[32] S. Itoh, T. Watanabe, K. Ohtsu, M. Taniguchi, S. Uzawa, and N. Nishimura, "Experimental Study of Field Emission Properties of the Spindt-type Field Emitter," *J. Vac. Sci. Technol.,* vol.B13(2), p.487, 1995.

[33] C. A. Spindt, C. E. Holland, A. Rosengreen, and I. Brodie, "The Effects of Size and Shape on Field-Emitter Array Performance," *Proc. 4th Intern. Vac. Microelect. Conf.,* p.33, Nagahama, Japan, 1991.

[34] R. B. Marcus, K. Chin, Y. Yuan, H. J. Wang, and W. N. Carr, "Simulation and Design of Field Emitters," *IEEE Trans. Electron Devices,* ED-37, p.1545, 1990.

[35] H. S. Uh, and J. D. Lee, "New Fabrication Method of Silicon Field Emitter Arrays Using Thermal Oxidation," *J. Vac. Sci. Technol.,* vol.B13(2), p.456, 1995.

[36] H. Busta, G. Gammie, S. Skala, M. Fury, M. Stell, and T. Myers, "Fabrication of Volcano Emitters Using Chemical Mechanical Polishing (CMP)," *Proc. 9th Intern. Vac. Microelect. Conf.,* p.388, St. Petersburg, Russia, 1996.

[37] R. B. Marcus, T. S. Ravi, T. Gmitter, J. T. Niccum, K. K. Chin, and D. Liu, "Atomically Sharp Silicon and Metal Field Emitters," *IEEE Trans. Electron Devices,* ED-38, p.2289, 1991.

[38] R. B. Marcus, and T. T. Sheng, "The Oxidation of Shaped Silicon Surface," *J. Electronchem. Soc,* vol. 129, No. 6, p.1287, 1982.

[39] R. B. Marcus, T. S. Ravi, T. Gmitter, K. K. Chin, D. Liu, W. J. Orvis, D. R. Ciarlo, C. E. Hunt, and J. Trujillo, "Formation of Silicon Tips with <1nm Radius," *Appl. Phys. Lett.*, vol.56(3), p.236, 1990.

[40] D. Liu, "Fabrication and Characterization of Gated Silicon Field Emission Micro Triodes," Dissertation, Dept. of E. E., NJIT, 1992.

[41] D. B. Kao, J. P. McVittie, W. D. Nix, and K. C. Saraswat, "Two Dimensional Thermal Oxidation of Silicon-I. Experiments," *IEEE Trans. Electron Devices*, ED-34, p.1008, 1987.

[42] K. Betsui, "Fabrication and Characteristics of Si Field Emitter Arraya," *Proc. 4th Intern. Vac. Microelect. Conf.*, p.26, Nagahama, Japan, 1991.

[43] E. Yablanvitch, D. L. Allara, C. C. Chang, T. Gmitter, and T. B. Bright, "Unusually Low Surface-Recombination Velocity on Silicon and Germanium Surface," *Phys. Rev. Lett.*, p.249, 1986.

[44] D. B. King, and J. G. Fleming, "Testing of Fillet Emitter Structures with Well Defined Emitter-to-Gate Spacings," *Proc. 9th Intern. Vac. Microelect. Conf.*, p.413, St. Petersburg, Russia, 1996.

[45] R. J. Harvey, R. A. Lee, A. J. Miller, and J. K. Wigmore, "Aspects of Field Emission from Silicon Diode Arrays," *IEEE Trans. Electron Devices*, ED-38, p.2323, 1991.

[46] H. H. Busta, B. J. Zimmerman, M. C. Tringgides, and C. A. Spindt, "DC I-V Characteristics of Field Emission Triodes," *IEEE Trans. Electron Devices*, ED-38, p.2558, 1991.

[47] N. E. McGruer, K. Warner, P. Singhal, J. J. Cu, and C. Chan, "Oxidation-Sharpened Gated Field Emitter Array Process," *IEEE Trans. Electron Devices*, ED-38, p.2389, 1991.

[48] I. Brodie, "The Significance of Fluctuation Phenomena in Vacuum Microelectronics," *Proc. IEDM 89*, p.521, 1989.

[49] C. J. Bennette, L. W. Swanson, and F. M. Charbonnier, "Electrical Breakdown between Metal Electrodes in High Vacuum II. Experimental," *J. of Appl. Phys.*, p.634, 1967.

[50] D. Alpert, D. A. Lee, E. M. Lyman, and H. E. Tomaschke, "Initiation of Electrical Breakdown in Ultrahigh Vacuum," *J. Vac. Sci. Tech.* 1, p.35, 1964.

[51] R. Forman, "Evaluation of the Emission Capabilities of Spindt-Type Field Emitting Cathodes," *Applications of Surfaces Sciences 16,* p.277, 1983.